ADVANCED ENERGY MATERIALS
www.advenergymat.de

Toward High-Areal-Capacity Electrodes for Lithium and Sodium Ion Batteries

*Yijun Chen, Bo Zhao, Yuan Yang, and Anyuan Cao**

In recent decades, extensive nanomaterials and related techniques have been proposed to achieve high capacities surpassing conventional battery electrodes. Nevertheless, most of them show low mass loadings and areal capacities, which deteriorates the cell-level energy densities and increases cost after the consideration of inactive components in batteries. Achieving high-areal-capacity is essential for those advanced materials to move out of laboratories and into practical applications, yet remains challenging due to the decreased mechanical properties and sluggish electrochemical kinetics at elevated mass loadings. In this paper, the previously reported strategies for promoting areal lithium storage performance, including material-level designs, electrode-level architecture optimization, and novel manufacturing techniques are reviewed. Sodium-ion battery electrodes are discussed subsequently, emphatically on its difference with those for lithium storage. Pouch-cell-level energy densities based on high-areal-capacity electrodes with different thicknesses are also estimated. For each category of these strategies, working principles, advantages, and possible problems are analyzed, with typical examples presented in detail and a summary table comparing the structures and achieved performance. Finally, the features of the high-areal-capacity electrodes demonstrated in this review are concluded, and overlooked issues and potential research directions in this field are summarized.

1. Introduction

Attributed to the high energy density, environmental benign nature and low self-discharge, lithium-ion batteries (LIBs) have become the most popular and prevailing power sources for consumer electronics and electric vehicles nowadays.[1] As an alternative to LIBs, sodium-ion batteries (SIBs) have also attracted increasing attention in large-scale static energy storage systems, due to the rich abundance of sodium (nearly 1000 times that of lithium) and lower cost (\$0.50 kg^{-1} Na_2CO_3 vs \$6.50 kg^{-1} Li_2CO_3).[2] Traditional battery electrodes like $LiCoO_2$ and graphite in LIBs are based on ion-intercalation mechanism with limited electrode capacities and almost touching the ceilings after the past decades of development. And researchers are exploring electrodes with different ion storage mechanisms for higher theoretical specific capacities, such as metal oxides/sulfides/fluorides with conversion reaction mechanisms, and silicon/tin/phosphorus with alloying mechanisms.[3] However, these materials generally exhibit low intrinsic electron conductivity, insufficient ion diffusion channels, and large volume variation during reaction, leading to deteriorated electrochemical kinetics and cycle stability in practical use.[4] The problems are even more severe for SIBs due to the larger ionic radius and slower transport of Na^+. Reducing the size of active materials to nanometer scale and compositing them with conductive additives is a promising strategy to mitigate these issues and has induced a worldwide research boom in recent years.[5] The innovations have substantially stimulated the energy storage potential of the proposed new materials. Nevertheless, to transfer outstanding lab results to industry applications, achieving high electrode mass loadings (denoted as M_a, which contains both active and inactive materials) is of great significance in practical batteries but have been neglected for long time in previous studies.

The significance of high M_a is mainly featured by two aspects—energy density and cost. Typically, a standard lithium-ion battery (LIB) contains both active and inactive components (**Figure 1**a). The former are electrode coatings involved in electrochemical reactions during charge/discharge and directly determine how much energy can be stored in batteries. The latter generally consist of metal current collectors, separators, electrolyte and outer housings. These components are important for the normal and stable operation of batteries, but come with a cost of additional dead weight (>60% content in some cases,[6] Figure 1b) without direct lithium storage capacity contribution. Taking this into account, the claimed material-level performance enhancement may be heavily discounted when scaled up to a cell level, especially for those obtained at very low mass loadings.[7] Suppose there are two

Y. Chen, B. Zhao, A. Cao
School of Materials Science and Engineering
Peking University
Beijing 100871, China
E-mail: anyuan@pku.edu.cn
Y. Yang
Program of Materials Science and Engineering
Department of Applied Physics and Applied Mathematics
Columbia University
New York, NY 10027, USA

The ORCID identification number(s) for the author(s) of this article can be found under https://doi.org/10.1002/aenm.202201834.

DOI: 10.1002/aenm.202201834

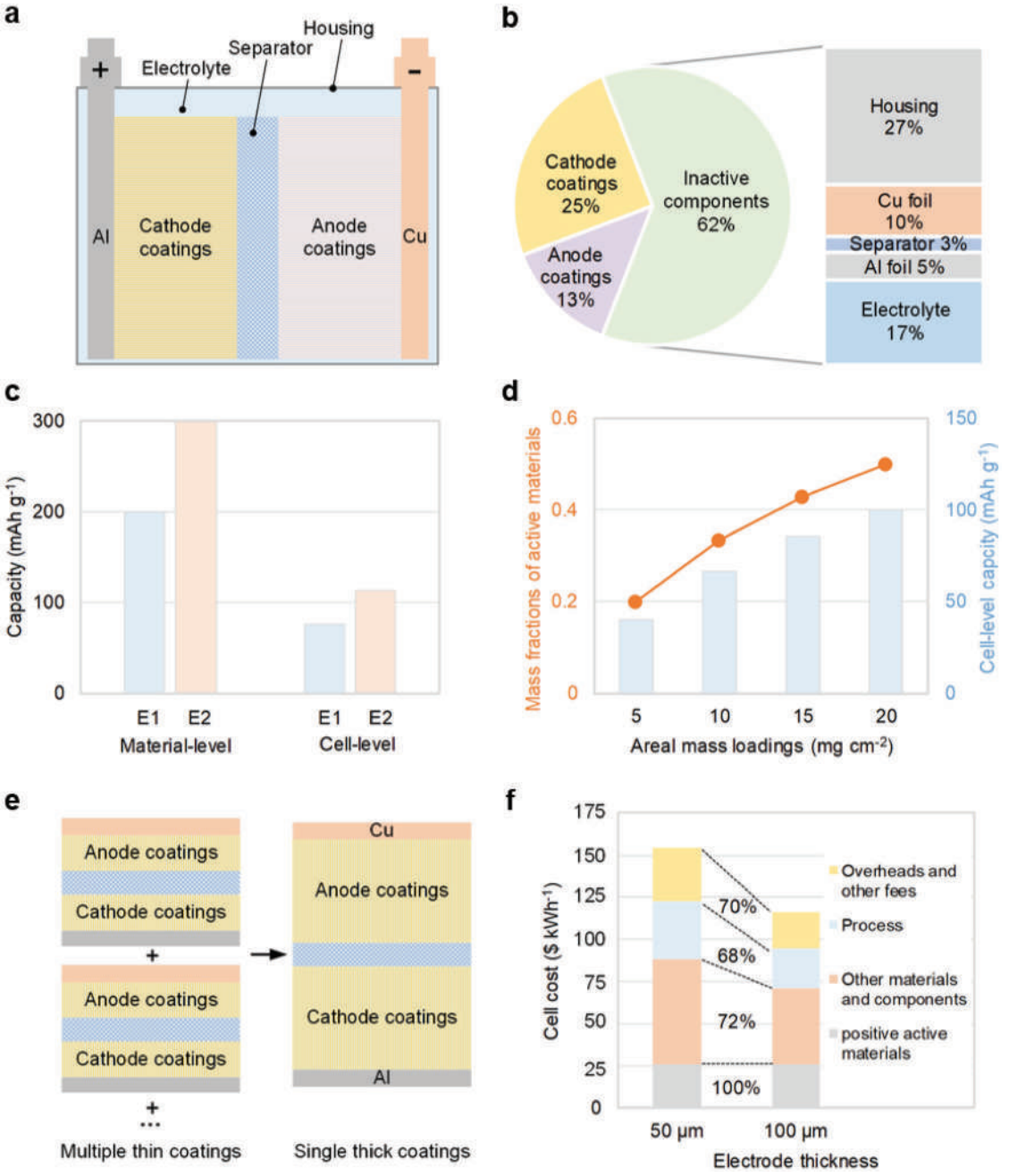

Figure 1. Raising electrode mass loadings for energy density enhancement and cost down. a) Typical configuration of a LIB. b) The mass split of a commercial $LiFePO_4$ cell with the format 18650. Reproduced with permission.[6] Copyright 2014, Royal Society of Chemistry. c) The material- and cell-level capacity of two hypothetical electrode systems. d) The influence of areal mass loadings of active materials on their mass fractions and cell-level capacities in a hypothetical cell, assuming the mass loading of total inactive components is 20 mg cm^{-2} and the active material capacity is 200 mAh g^{-1}. e) Schematic showing using higher mass loading electrodes can reduce the amounts of cells for achieving the same energy. f) Modeled cost breakdown of LIB based on NMC111 cathodes with 50 and 100 μm electrode thicknesses. To prove the view of lowering cell cost by higher electrodes mass loading, assume that the proportion of each component's cost in cell remained unchanged from 2015 to 2022, and we provided the updated cost value around $130 per kWh based on the currently LIB cost in practice. f) Reproduced with permission.[9] Copyright 2015, John Wiley and Sons.

electrode systems of E1 and E2 (Figure 1c). The active materials in E2 exhibit a higher capacity of 300 mAh g^{-1} than that (200 mAh g^{-1}) of E1, suggesting an effective material optimization. After cell assembly based on E1 and E2, inactive components are included. Assuming its mass fraction is 60% (Figure 1b), as a result, the material-level capacity enhancement of 100 mAh g^{-1} fails to hold up and reduces to 40 mAh g^{-1} at the cell level, suggesting that the practical capacity enhancement based on material innovation is restricted by content of active materials in batteries. Using high-M_a electrodes helps diminish

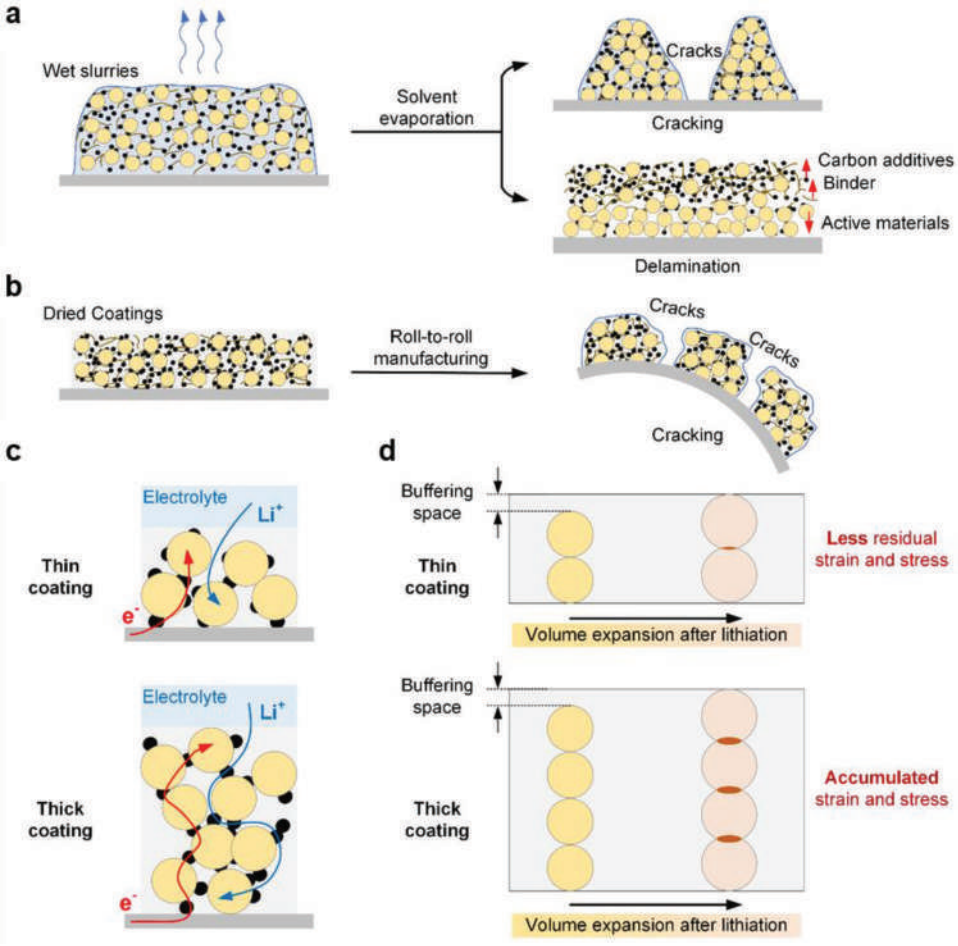

Figure 2. Schematic of the challenges in achieving high-mass-loading electrodes. Cracking and delamination problems during a) the electrodes drying and b) winding processes. More sluggish c) electrochemical kinetics and d) accumulated stress and strain during lithiation/delithiation processes in thick electrodes.

the adverse effects. As the different components in batteries are usually assembled face to face and have roughly the same areas, raising mass loading of active materials can improve their mass fraction in batteries and thus enhance the cell-level capacity. The hypothetical model (Figure 1d) shows that after M_a increases from 5 to 20 mg cm^{-2}, the content of active materials rises from 0.2 to 0.5, and it contributes to a capacity enhancement from 40 to 100 mAh g^{-1}. It confirms that improving M_a can effectively raise the cells' energy densities.

Improving electrodes M_a also helps lower the cost, by decreasing the number of cells to attain the same energy (Figure 1e). The total cell cost can be reduced in three parts: materials cost, process cost, and overheads and other fees. First, fewer cells reduce the consumption of current collectors, separators, and outer packing housings, and thereby lowers the materials cost. Second, increasing M_a reduces the number of steps in cell manufacturing, including casting slurries, calendaring coatings, winding electrodes, filling electrolyte, etc., and thereby decreases the process cost.[8] Last, owing to the less handled materials purchases and process improvement, also the overheads can be reduced.[9] In addition, fewer cells ease the burden of battery management systems with less complex individual cell monitoring and thus reduces the relevant overheads. Patry et al. performed the cost modeling of LIB based on Li($Ni_{0.33}Co_{0.33}Mn_{0.33}$)$O_2$ (NMC111) cathodes with two coating thicknesses (Figure 1f).[9] With the electrode coating thickness increased from 50 to 100 µm, the total cell cost reduces notably from ≈150 to ≈120 $ kWh^{-1}. Except for the same cost of NMC111 cathode materials, the reductions in cost of other material, process, overheads and other fees are all as high as ≈25%, confirming that it is effective to lower cell cost by higher electrodes mass loading.

Despite the above advantages, achieving high mass loadings is not a simple task due to the accompanying challenges in electrode manufacturing and electrochemical reactions. In terms of the electrode manufacturing, the slower slurry drying process for thick electrodes can cause two problems (**Figure 2**a). First, the capillary stress induced by the slow and uneven solvent evaporation leads to more severe electrode cracking.[10] Second, it exacerbates the electrode delamination problems due to the heterogeneous migration of slurries ingredients—Low-density polymer binders and carbon additives float upwards to the electrode surface, while heavier active materials sink to the bottom (Figure 2a). The resultant uneven distribution of

electrode components deteriorates both the mechanical and electrochemical properties of electrodes.[11] Besides, due to the weak adhesion between active materials and metal current collector,[12] the dried thick electrode coatings could fragment and exfoliate from current collectors during winding in high-speed roll-to-roll processes (Figure 2b).

After cell assembly from thick electrodes, problems arise in electrochemical reaction processes during battery operation. First, the electronic and ionic resistance of electrodes would increase due to higher point-point impedance among the active materials particles and longer ion diffusion path in electrodes (Figure 2c), which results in an enlarged cell polarization and thereby a lower capacity delivered in the fixed voltage window. Second, more nonuniform current distribution ascribed to the heterogeneous electron and ion transport causes a larger state-of-charge variation in electrodes, and thereby a decreased cycling stability.[13] It has been reported that the mass loadings could proportionally enlarge the magnitude of such charge transport heterogeneities.[14] A typical example is the degradation of thick graphite anodes in LIB. The lithium-ion conductivity reduction forms a large lithium concentration gradient in the thickness direction, resulting in an intensified intercalation stress on the graphite close to electrolyte and possible particles fractures.[15] Moreover, the additional overpotential in thicker electrodes could lead to metallic lithium plating on graphite particles in vicinity to the separator in the charging process,[16] resulting in lithium and capacity losses and increased safety risks.[17] Third, higher mass loading causes more severe mechanical strain and stress accumulation in electrodes (Figure 2d), leading to more cracks and exfoliations in the coating layers during cyclic charge/discharge, especially for the materials with serious volume change and lower mechanical strength.[18] The more severe pulverization of active materials results in a faster electrochemical performance degradation.[19]

Given the advantages of improving areal mass loadings (Figure 1) and its adverse effects on electrochemical kinetics (Figure 2), researchers have been increasingly using areal capacity (C_a) as a more practical criterion to evaluate the electrode performance at high mass loadings, as it takes both mass loading and gravimetric capacity (C_g) into consideration ($C_a = M_a \times C_g$). In the past several decades, tremendous work has been devoted to developing novel materials for high C_g, while the investigation on electrodes with high M_a and C_a is relatively overlooked. Currently, most of the reported LIB and SIB electrodes in literature have M_a typically lower than 1 mg cm^{-2},[20] which definitely results in a limited C_a. Even for silicon anodes with extraordinarily high theoretical capacity for lithium storage, most of them show areal capacities <1 mAh cm^{-2}.[21] And for most of SIB electrodes, the achieved areal capacity is also lower.[22] Such areal ion storage performance is significantly lower than that of electrodes in commercial cells (2.5–3.5 mAh cm^{-2}), suggesting plenty of room for improvement. Despite the importance in understanding what people have tried to improve it, the relevant reviews are quite few, except a recent one by Kuang et al.[23] mainly summarizing the general structural designs and fabrication for thick electrodes. The objective of this paper is to provide a more detailed overview of the progresses toward high-areal-capacity LIB/SIB electrodes and helps depict a clear picture of the development pathways in this field.

So, starting from the initial question—what can we do to enhance the areal ion storage performance of an electrode? Theoretically, C_a can be calculated using the following equation: $C_a = C_g M_a = C_g \frac{\rho S h}{S} = C_g \rho h$, where ρ, S, and h correspond to the density, base area, and thickness of the electrode, respectively. As shown, we can work from two aspects to improve M_a: fabricating high-tap-density active materials (increasing ρ) and using thicker electrodes (increasing h). Besides, to maintain a high C_g, we also need to minimize the negative impacts of high M_a on the physical and electrochemical properties. To this end, various materials/electrodes structures have been investigated (**Figure 3**). At the material level, novel binders are developed to enhance the structural stability of conventional electrodes. And at the electrode level, researchers have proposed other architectures such as 2-D layered or vertically aligned configurations, and 3-D electrodes by percolating network or in-situ hybridization. Novel manufacturing techniques are also proposed to engineer thick electrodes to enhance their mechanical properties and charge transport kinetics. In this paper, we review all these progresses by selecting representative examples of each category, and analyzing their working principles, advantages, and possible problems. Tables summarizing main properties of proposed electrodes are given for each group of studies. LIB-related work is reviewed first due to its broad coverage of research types provided by the abundant references. SIB-related ones are discussed later, with a comparison with those of LIBs. Finally, after going over the aforementioned researches, we conclude with the difference in C_a-oriented work from those focusing on simply C_g improvement. We then list several remaining issues associated with high areal capacities, and a future outlook on potential research directions is presented in the end.

2. High-Tap-Density Active Materials

Increasing the tap density (ρ) of active materials is a direct strategy to enhance the areal mass loading (and thus improved areal capacity) of electrodes with a constant electrode thickness. It is generally attained by making microclusters assembled by tightly-packed nanoscale subunits, which can achieve higher tap density compared to loosely dispersed nanomaterials, while utilizing the superiority of nanostructures at the same time.[24] Actually, similar strategies have already been applied in commercial high-energy-density cathode materials such as lithium nickel manganese cobalt oxide (NMC)[25] and lithium nickel cobalt aluminum oxide (NCA)[26] secondary microparticles which are composed of densely-packed primary nanocrystallites.

Figure 4 shows some typical examples of this design concept.[27] Areal lithium storage capacity of the TiO_2/C electrode was significantly improved based on a multilevel structural optimization in crystalline, nanoscale and microscale domains (Figure 4a). First, the (001)-rich facets of TiO_2 confined in graphitic carbon coatings (Figure 4b) prompted the Li^+ intercalation/de-intercalation kinetics

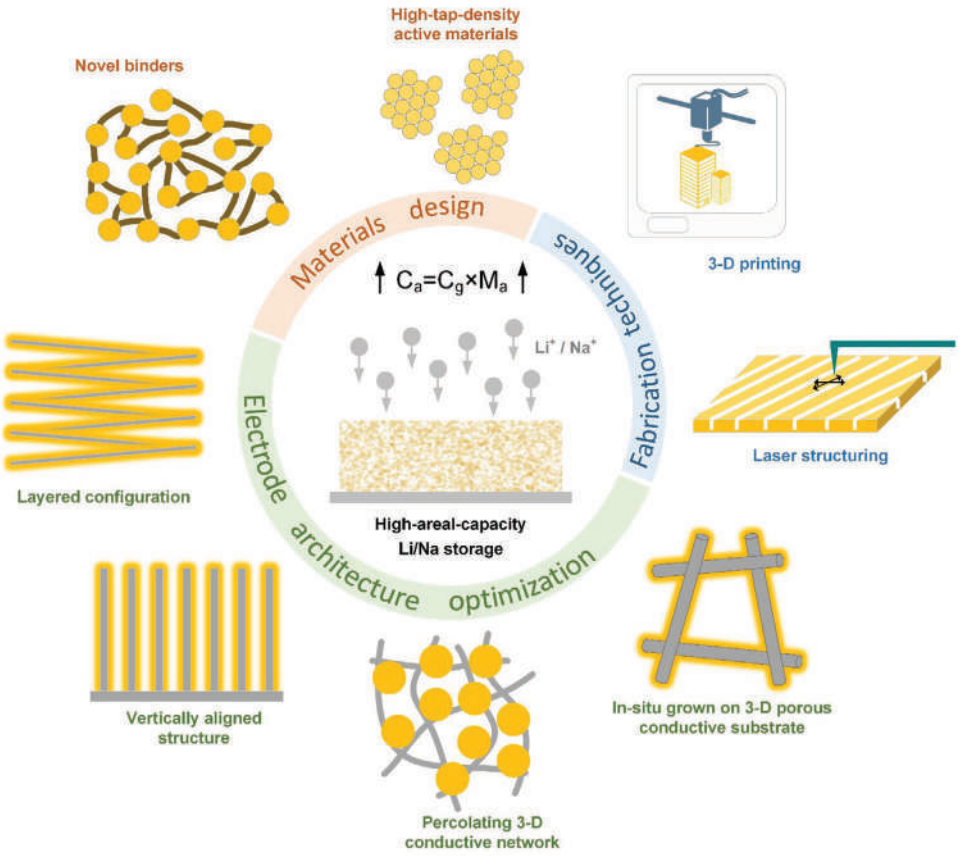

Figure 3. An overview of the solutions to high-areal-capacity lithium and sodium storage. The material-level designs include high-tap-density active materials and novel binders, and are mainly based on conventional slurry-casted electrodes. The electrode architecture innovations include layered configurations, vertically aligned structures, percolating 3-D network, and in situ grown active materials on 3-D substrates. Novel manufacturing techniques are shown using 3-D printing and laser structuring as two typical examples. The yellow, gray, and brown parts in the schematic represent active materials, conductive agents matrix or substrate, and binders, respectively.

and electron transport. Second, the hollow TiO_2 structure (Figure 4c) can buffer the volume variation during repeated charge/discharge, and the interior cavity serves as electrolyte reservoir shortening lithium diffusion pathways. Third, the TiO_2 nanospheres with diameters of 40–60 nm were densely packed to form a pomegranate-like microcluster with a diameter of about 0.9 µm (Figure 4d), resulting in a much higher tap density (1.67 g cm^{-3}) than that of bare nanopowders particles (0.11 g cm^{-3}). In summary, the as-prepared microcluster TiO_2/C anode was capable of high tap density from: i) the {001}-rich high energy facets were piled up in the TiO_2 hollow nanospheres forming a yolk–shell structure; ii) the microclusters were densely constructed of graphitic carbon-conformal TiO_2 hollow nanospheres; iii) a pomegranate-like microsphere was obtained via close packing of the TiO_2/C microclusters. The above three functionality synergistically endowed TiO_2/C anode with high tap density. Given the enhanced charge transport kinetics, well-kept mechanical integrity, and increased tap density, the final microcluster anode exhibited an excellent areal lithium storage capability. A stable and high areal capacity of 4.9 mAh cm^{-2} was obtained at a mass loading up to 23.7 mg cm^{-2} after 5000 cycles.

Yolk–shell structures and mechanical pressure treatment also can be used to achieve high-tap-density property. Zhang et al.[28] efficiently utilized inner voids containing some active materials such as multiple Si yolks, Fe_2O_3 nanoparticles, and carbon nanotubes (CNTs) for Li^+ storage (Figure 4e,g). Moreover, bridged spaces were constructed between the inner Si yolks and outer shell through a conductive CNTs "high-way," allowing flexible expansion and contraction of the conducting networks. Owing to the advanced yolk–shell Si/C structure, a high area capacity of 3.6 mAh cm^{-2} was achieved at 2.83 mg cm^{-2} mass loading and retained 95% after 450 cycles. By giving a mechanical pressure to produce clusters, Lin et al.[29] opened up a promising opportunity for tuning the packing density. Inspired by those predecessors, Sun et al.[30] fabricated a red P/C nanocomposite anode materials, in which amorphous red P nanodomains were embedded in the nanopores of micrometer-scale porous conductive carbon with interior nanoscale void spaces (Figure 4h). Due to the high capacity of the P/C material and its space-efficient packing, the average thickness of P/C electrodes was 21.5 µm, in which mass loading was up to 4.3 mg cm^{-2}, much thinner than the 76.3 and 124.5 µm for $Li_4Ti_5O_{12}$ and graphite electrodes, respectively, under the same industrial-level areal capacity of ≈3.5 mAh cm^{-2} at 0.5 mA cm^{-2}.

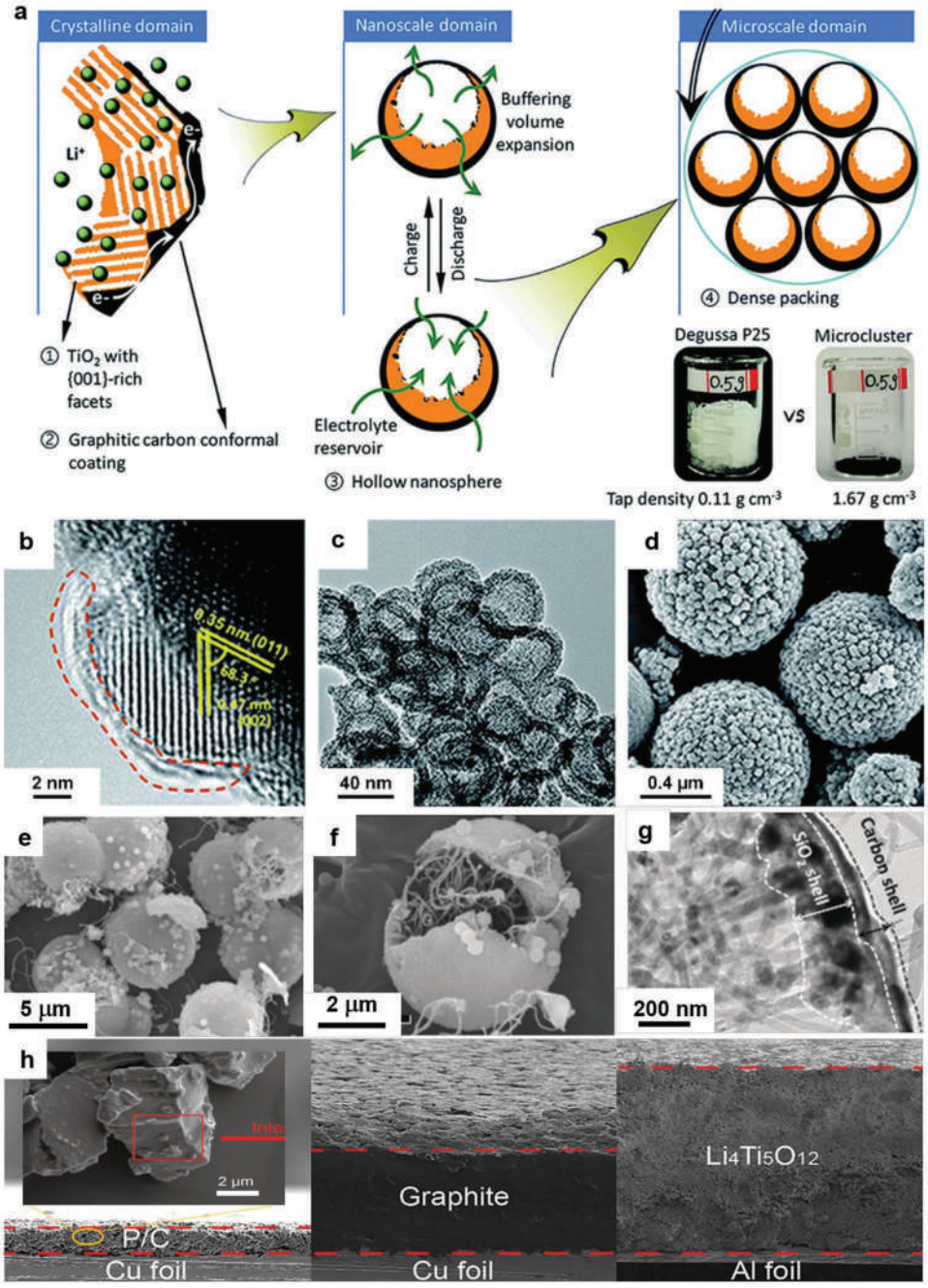

Figure 4. High-tap-density active materials with optimized hierarchical structures for areal capacity enhancement. a) Schematic of the structural engineering in crystalline, nanoscale, and microscale levels. The bottom right corner shows the tap density comparison between the proposed microcluster powders and commercial Degussa P25 TiO_2. b) High-resolution transmission electron microscope (HR-TEM) image, showing the crystalline phase of TiO_2 shell and outer graphitic carbon coating. c) TEM image of the TiO_2 hollow nanospheres. d) Scanning electron microscope (SEM) image of the TiO_2 microclusters composed of tightly packed nanosubunits. Reproduced with permission.[27] Copyright 2018, Royal Society of Chemistry. e,f) SEM images of the yolk–shell Si/C particles. g) HR-TEM image of the C/SiO_2 double shell, in which the inner SiO_2 shell is coated with outer amorphous carbon shell. Reproduced with permission.[28] Copyright 2019, John Wiley and Sons. h) Cross-section SEM images of the P/C, graphite, and $Li_4Ti_5O_{12}$ electrodes with the same areal capacity and different thicknesses. Reproduced with permission.[30] Copyright 2019, Elsevier.

High-tap-density active electrode also tends to provide excellent high power density performance.[31] Traditionally, the most intuitive and common ways to achieve high power and/or rate performance are to create nanosized or porous (usually hierarchical) structure, which minimizes the Li^+ ion solid-state diffusion distances and increases the surface area of the electrode materials in contact with the electrolyte.[32] However, this strategy is contrary to the high-tap-density and high-areal-mass

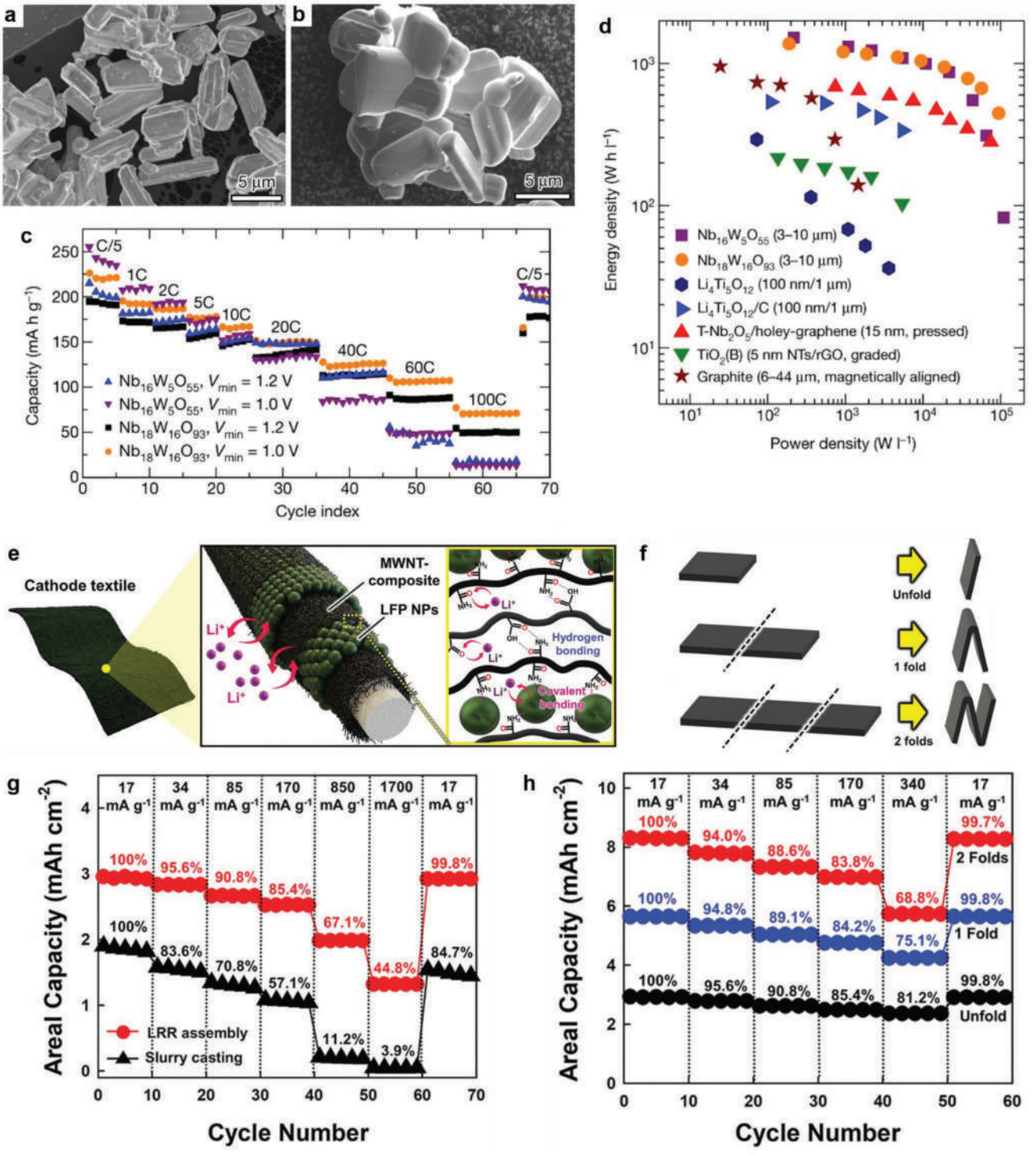

Figure 5. High-tap-density bulk electrodes achieving high-power density and excellent rate performance. SEM images of dense block with 3–10 μm primary and 10–30 μm agglomerate a) $Nb_{16}W_5O_{55}$ and b) $Nb_{18}W_{16}O_{93}$. c) Rate performance summary from 0.5 C up to 100 C. d) Energy density and power density for anode active materials versus. Reproduced with permission.[33] Copyright 2018, Springer Nature. Schematic illustrations of e) LFP-based carbon textile composite hybridized with MWNTs and f) zigzag folding approach for thick electrode. Comparison of rate capabilities of g) carbon textile composites electrode and slurry casting electrodes and h) twofolds, onefold and unfold carbon textile composite electrodes. Reproduced with permission.[35] Copyright 2021, John Wiley and Sons.

loading electrode. In practice, a series of niobium tungsten oxides particles (**Figure 5**a $Nb_{16}W_5O_{55}$ and b $Nb_{18}W_{16}O_{93}$) with micrometer size were fabricated as high-tap-density electrodes, which showed excellent rate performance due to the appropriate host lattice allowing fast Li^+ ion solid-state diffusion.[33] It was noted that their electrochemical performance was illustrated by

Table 1. The literature survey on the high-tap-density active materials for electrodes with high lithium storage performance.

Electrode structure	Tap- density [g cm^{-3}]	I [mA g^{-1}, mA cm^{-2}]	Cycles	M_a[c)] [mg cm^{-2}]	C_a[a)] [mAh cm^{-2}]	Refs.
Graphitic carbon-coated hollow TiO_2 nanospheres-assembled microcluster	5.4	1675	1000	23.7	4.9	[27]
Yolk–shell Si/C nanobeads	–[b)]	0.6	100	2.83	2.5	[28]
Red P/C nanocomposite	1	0.86	500	4.3	3	[30]
Si nanoparticle/carbon shell pomegranate microbeads mixed with CNT	0.4	0.7	100	3.12 (Si+C)	3.1	[37]
Nanostructured silicon secondary cluster	1.38	0.5	100	2.02	2.3	[29]
$Fe_2(MoO_4)_3$ hollow hierarchical microsphere	–	500	30	5	4	[24]
Micrometer-sized porous Fe_2N/C bulk	1.03	50	85	6.2	2.96	[38]
		100	200	7	2.59	
CuO mesocrystal/CNT	–	0.39	400	1.947	1.11	[39]
$Li_4Ti_5O_{12}$ microspheres//$LiNi_{0.5}Mn_{1.5}O_4$	1.32	441	1000	3.5	0.37	[40]
Microsized porous Ge	–	1	100	4.45	3.47	[41]

[a)] C_a listed in the table represents the areal capacities after cyclic tests (the same below); [b)] "–" means the data is not provided in the paper (the same below); [c)] M_a is denoted as the value of mass loading from cited literatures.

studying large dense particles of the block with 3–10 μm primary ones and 10–30 μm agglomerates, which were prepared via gram-scale solid-state synthesis. Given the high crystallinity structure and high-tap density of electrode, bulk niobium tungsten oxides led to exceptional rate performance from 0.5 C (171 mA g^{-1}) up to 100 C (Figure 5c), even high-rate cycling for 250 cycles at 10 C, followed by 750 cycles at 20 C. Compared with state-of-the-art high-rate anode materials, those niobium tungsten oxides bulk consisting of hierarchical particle agglomerates showed higher energy and power densities (Figure 5d).

Different from the intrinsic feature of bulk materials with fast charge transport pathway, it is also an effective strategy to artificially design composite structure with fast ion channels.[34] By reasonable design of ligand replacement reaction-mediated assembly, Kwon et al.[35] obtained $LiFePO_4$ (LFP)-based carbon-textile composite cathode enabling both high areal capacities and superior rate capability. Figure 5e showed the schematic illustration of composite cathode textile, in which LFP nanoparticles were densely assembled on the surface of amine-functionalized multiwalled carbon nanotubes layer-by-layer without agglomerations or segregations, enhancing electron transfer at all interfaces. Compared with slurry casting-based LFP electrode (Figure 5g), the textile-based composite electrode exhibited higher capacities at various current densities, indicating that rational structure design could obtain superior rate capability. Furthermore, due to their flexibility, textile electrodes can be folded into zigzag patterns (Figure 5f) to increase high areal mass loading which is proportional to the number of folds. Based on the excellent structural stability, folded textile electrodes delivered high areal capacities of 5.7 mAh cm^{-2} at 2 C (mass loading up to 45.9 mg cm^{-2}) in Figure 5h.

Other similar microensembles have been reported to achieve a high tap density (**Table 1**). Generally, compared to single sized particles, mixed sized particles perform high-tap density because of their closely topologic packing structure. Furthermore, some dense structures including intrinsic morphology such as pomegranate-like or artificially composite structure such as core-shell and yolk-shell could also achieve high-tap density. Common electrode structures and strategies to improve the high-tap-density active materials are summarized as follows:

i) Pomegranate-like structure: Nanoscale active materials have outstanding advantages in high specific capacity performance; however, they should preferably be self-assembled into larger-sized pomegranate-like clusters to reduce gaps between nanoparticles, achieving maximum electrode density such as pomegranate-like microspheres obtained via closely packing TiO_2/C microclusters;[36] Si nanoparticle/carbon shell that are arranged into pomegranate microbeads.[37] Under such self-assembly strategy, these primary nanoparticles (<100 nm) grow up to secondary microclusters (>1 μm), improving the arrangement of electrode structure, and thus reducing porosity and increasing energy density.
ii) Mixed-sized topology particles: Some classical structures (e.g., yolk–shell and/or core–shell, etc.) are essentially composed of particles with different sizes which are compounded into a more density topology structure. A hollow shell plays an important role in inhibiting the volume expansion of the electrode and reducing electrochemical side reactions. Therefore, some highly active materials could be properly filled in a hollow shell to make full use of the interior space. For example, a carbon-coated rigid SiO_2 outer shell confined with multiple Si nanoparticles (yolks) and CNTs with embedded Fe_2O_3 nanoparticles (yolks) could achieve high tap density and high areal capacity of 3.6 mAh cm^{-2}.[28]
iii) Micrometer-sized block materials: Micrometer-size blocks are usually larger than 2 μm. And there are two main forms, one consists of individual particles with inherent size, the other is made of artificially fabricated larger blocks by mechanical rolling and/or ball milling nanoparticles. For example, niobium tungsten oxides blocks (up to 30 μm) show high tap density due to the intrinsic high crystallinity.[33] By mechanical rolling, nanostructured Si@SiO_2 powders are fabricated to secondary clusters with average size of about 4.4 μm.[29]

Table 2. The literature survey on binder engineering for electrodes with high lithium storage performance.

Type	Binder	Electrode structure	I [mA g^{-1}, mA cm^{-2}]	Cycles	M_a [mg cm^{-2}]	C_a [mAh cm^{-2}]	Refs.
Interaction with active materials	Functionalized poly(ethylene oxide)-based polyurethanes	Si powder + Super P + binder	3000	600	0.3	0.3	[45]
	Guar gum biopolymer	$ZnCo_2O_4$ microparticle + Super P + binder	200	30	6.73	4.4	[44]
	PAA + isocyanate-terminated polyurethane oligomers	Si powder + Super P + binder	600	150	1	3	[46]
	Sodium carboxymethylcellulose + polyacrylic acid + polyethylene oxide	$LiNi_{0.33}Mn_{0.33}Co_{0.332}$ + Super C65 + binder	1.8	200	60	5	[43d]
	Poly(acrylic acid)	Microsized Si–C particles wrapped by graphene sheets + binder	50	100	3.2	3.2	[43a]
Mechanical properties	Self-healing polymer	Self-healing polymer/carbon black composite melted and coated on slurry cast Si electrodes	0.3	140	1.6	2.9	[47]
		Si powder and self-healing poly(ether-thioureas) with balanced rigidity and softness	4200	250	1.2	1.44	[48]
	Trifunctional binder	Si + partially lithiated hard polyacrylic acid and soft Nafion	1500	300	0.94	1.5	[49]
	Self-healing ionomer	Low addition amount of self-healing ionomer Si/graphite + Super P + carboxy methylcellulose + binder	≈1500	100	6	2.15	[50]
	Hard poly(furfuryl alcohol) skeleton interweaved with soft polyvinyl alcohol filler	Si powder + Super P + binder	100	50	4.9	5.7	[51]
	Peach gum + epichlorohydrin network binder	Si powder + carboxyl groups + short-chain chemical crosslinker	500	110	1.99	3	[52]
Electronically conductive	PEDOT:PSS	Si nanoparticle + binder	–	100	1.5	2.3	[53]
	CNTs interwoven in cellulose nanosheets	$LiCoO_2$ + binder	0.5	20	86	12.1	[55]
	Binary network of conductive elastic polymer	Si powder + conducting polymer + stretchable polymer poly(ether-thioureas)	1000	300	0.75	1.65	[55]
Ionically conductive	Ion-type sulfonated polyimide	$LiFePO_4$ + Super P + binder	≈60	200	9	1.3	[56]
	Lithium salt of carboxymethyl cellulose	Graphite powder + styrene butadiene rubber + binder	≈170	50	10.5	3.16	[15]
	Poly(PEGMA-co-MMA-co-IBVE) copolymer binder + LiTFSI	$Li_4Ti_5O_{12}$ + Super P + binder	≈65	47	28	4.2	[57]
	Poly(PEGMA-co-MMA-co-IBVE) copolymer binder + LiTFSI	$LiCoO_2$ + carbon black + binder	≈65	50	30	4.53	[58]

As shown in Table 1, most materials possess hierarchical structures such as $Fe_2(MoO_4)_3$ hollow hierarchical microspheres,[24] micrometer-sized porous Fe_2N/C bulk,[38] as well as artificial structure design, which can not only buffer the volume changes in densely packed structures but also facilitate electrolyte infiltration to the inside of active material clusters. Those works suggest that combining high-tap density with rationally designed material structures represent an effective strategy to achieve high mass loadings and areal capacities.

3. Binder Approach

Binder is an essential part in electrodes owing to its role in adhering active materials and binding them with conducting agents and current collectors, which are particularly important in electrode coatings with high mass loadings; developing novel binders is a promising option for enhancing the mechanical stability and electrochemical performance of thick electrodes (**Table 2**). To this end, the most common strategy is

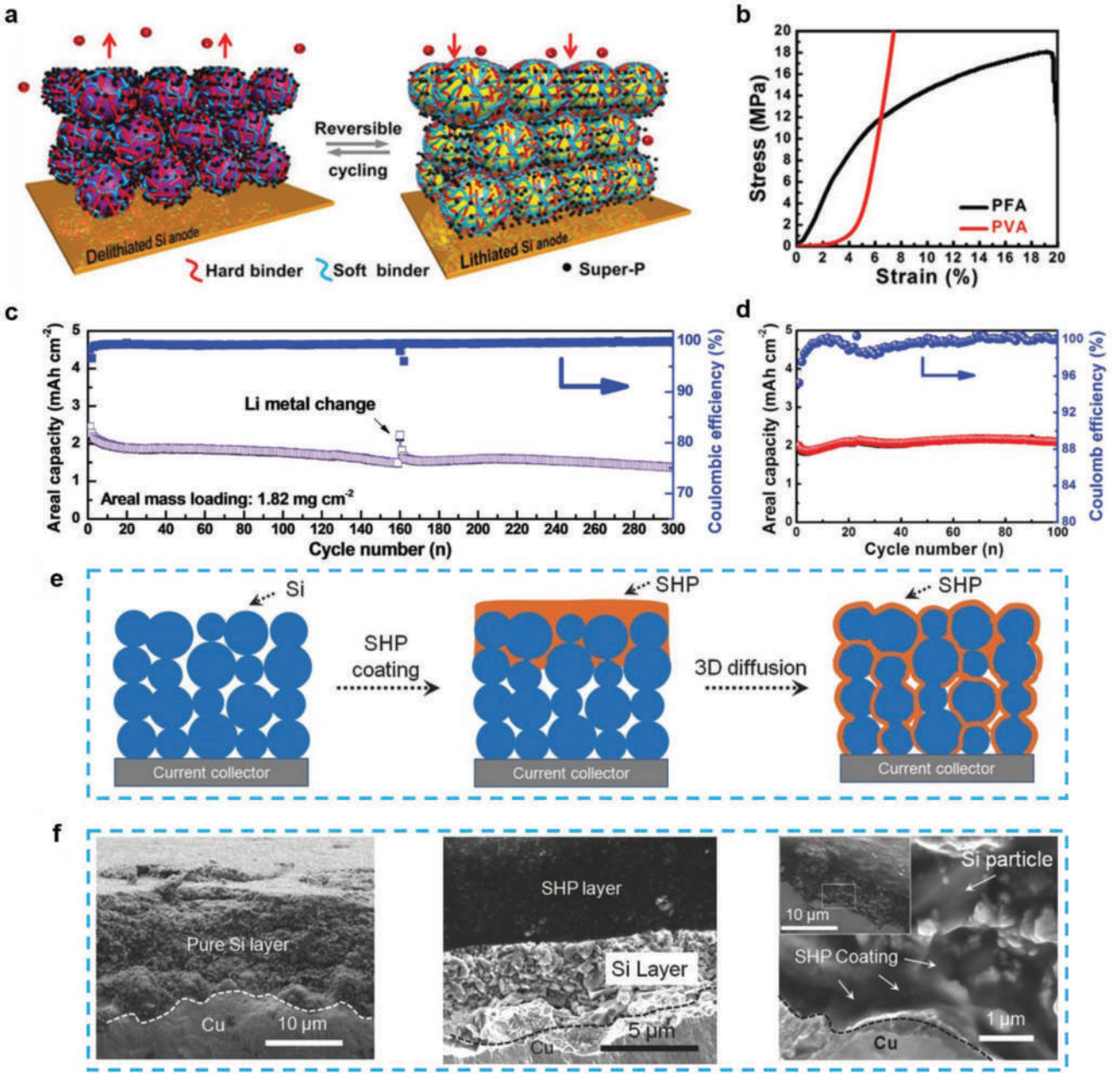

Figure 6. Interweaving 3-D binder network for high-areal-capacity electrodes. a) Schematic of the reversible cycling of silicon anodes in lithiated and delithiated states enabled by the interweaving hard and soft binder network. b) Stress–strain curves obtained from tensile tests, indicating the high stiffness of PFA and elasticity of PVA in the binder systems. c) Long-term cycling of the Si anode at 300 mA g^{-1} using the proposed hard/soft polymer binders. d) Cycling of Fe_2O_3 anodes at 100 mA g^{-1} based on similar binder systems, suggesting the universality of the strategy. Reproduced with permission.[51] Copyright 2019, John Wiley and Sons. e) Schematic design of 3-D spatial distribution of Si-SHP/CB electrodes. f) SEM images of SHP/CB binder infiltrating into the entire thickness of the Si layer. Reproduced with permission.[59] Copyright 2015, John Wiley and Sons.

to strengthen the interaction between binders and active materials. For example, functional binders like carboxymethyl cellulose, poly(acrylic acid), and sodium alginate are frequently used in silicon-based electrodes, rather than traditional PVDF binders. The covalent and/or hydrogen bonding between the carboxyl groups in these binders and the hydroxyl groups on the silicon surface generally contributes to enhanced structural integrity and thus higher cycling stability.[42] Combined with optimization on active materials structures, several reports based on these binders have achieved high mass loadings and areal lithium storage performance.[43] Similar approach has also been applied in $ZnCo_2O_4$ electrodes with guar gum biopolymer as binder.[44]

Designing binders with high intrinsic mechanical stabilities is another way to achieve robust electrodes. Liu et al. designed a 3-D interpenetrating binding network comprising both hard and soft polymers to enhance the silicon electrode stability (**Figure 6**a).[51] The hard part is a poly(furfuryl alcohol) (PFA)

skeleton with high stiffness for bearing the swelling and maintaining the integrity of electrodes, and the soft part is polyvinyl alcohol (PVA) fillers for buffering the large volume change of silicon particles during lithiation/de-lithiation (Figure 6b). The synergistic effect of two binder ingredients resulted in long-term steady cycling of silicon anodes with a high mass loading up to 1.82 mg cm^{-2} (Figure 6c). The proposed bi-network structured binders were also applied on other active materials like Fe_2O_3 to stabilize their electrochemical cycling (Figure 6d). Recently, Chen et al. developed self-healing polymer binders with high stretchability (up to ≈300% strain without breaking) and viscous flow capability for silicon electrodes.[47] As shown in Figure 6e,f, combining with carbon black, the self-healing polymer composites (denoted as SHP/CB) were coated on the Si electrode forming a top layer. Followed by repeatedly blading under heating condition, the SHP/CB composite binders were infiltrated into the entire thickness of the Si layer, forming a 3D distribution maximizing the interaction between binders and active materials inside the electrode. This new electrode design promoted more effective self-healing, even after rupture, it could recover internal conduction pathways and self-healing the physical contact between silicon particles and binders, resulting in high electrode integrity and cycling stability.

Besides the mechanical stability enhancement, endowing electrodes with higher charge transport kinetics can also be achieved by binders with high electron or lithium conductivities. For example, Higgins used the conducting polymer PEDOT:PSS as binder and achieved a high electrical conductivity of 4.2 S cm^{-1} in silicon electrodes.[53]

In summary, lithium conductivities can be enhanced by the incorporation of lithium salts in the binder systems such as lithium bis(trifluoromethanesulfonyl)imide/polyethylene glycol-based polymers[57,58] and lithium salt of carboxymethyl cellulose.[15] However, it should be pointed out that the polymer binders used in electrodes are not always conductors, and a considerable part of those polymers has low conductivity, which inevitably impedes the charge transfer in the electrodes owing to their insulating properties. Also, poorly conductive polymer binders continue to be used in batteries because of their attractive intrinsic mechanical properties, such as self-healing, excellent stiffness etc. An emerging strategy, therefore, is that combining highly conductive binders with excellent mechanical stability polymers as composite binders to explore applications in LIB.

In addition to electrical and mechanical properties of polymer binders, the binding property of the polymer binders should be preferentially prioritized. Generally, the binding capability of polymer binders is governed by molecular interactions between polymers. Due to the bond strength, the binding capability could be divided into three categories: weak supramolecular interaction, strong supramolecular interaction, and covalent cross-linked.[60] Active materials with different storage Li mechanisms (insertion-type, conversion-type and alloying-type) need to match rational polymer binders with different binding capability. For example, polymers with strong supramolecular interactions (e.g., self-healing polymer) usually are used as a binder for Si anode, which spontaneously recover the damage to the Si anode due to the large volume change during cycling. Additionally, during the slurry coating, the solid binders usually need to be dissolved in a liquid (e.g., deionized water or other organic solvents) to mix well with active materials. It is also very important to choose the appropriate liquid solvent according to the solubleness of the solid polymer binders.

The aforementioned two methods including high-tap-density active materials and novel binders are generally based on conventional slurry casted electrodes, and thus are compatible with current batteries production lines, which is one of its advantages. However, in such configuration with active coatings deposited on 2-D planar current collectors, the electrode thickness increase inevitably results in more sluggish charge transport and thereby limits its further performance improvement. To enable well-maintained electrochemical kinetics in thick electrodes, it is important to construct well-defined lithium and electron transport pathways to achieve an electrode-level structural optimization, as discussed in the following sections.

4. Low-Tortuosity Thick Electrode

For conventional electrode configurations, the close packing of nanoparticles generally leads to a tortuous pore structure, which inevitably increases the distance of Li^+ ion diffusing across the entire electrode, impeding the charge kinetics in thick electrode. Therefore, the fast-charging capability at the electrode level is still significantly plagued due to the random stacking of nanoparticles. According to the effective ionic conductivity D_{eff} expression ($D_{\text{eff}} = \frac{\varepsilon}{\tau}D$, where ε is the porosity, τ is the tortuosity, and D is the intrinsic ion conductivity),[61] novel thick electrodes with low tortuosity and high porosity are beneficial to improve ion transport rate capability. Following this fundamental view point, we discuss two types structure designs in thick electrode, including layered electrode configuration and vertically aligned structure. As shown in **Figure 7**, conventional electrode configurations with high tortuosity design generally impede the infiltration of electrolyte and considerably increase the ion transfer distance, decreasing the charge kinetics; To improve electrolyte permeability and the ion transfer rate, utilization of novel electrode architectures with low tortuosity structure have become a key principle for thick electrode design. Following this fundamental view point, we discuss two types of structure designs in thick electrode, including layered electrode configuration and vertically aligned structure.

4.1. Layered Electrode Configuration

Layered electrode configuration transforms single thick coating into multiple thin coatings with each one attached with current collectors, and thereby accelerates electron flow within thick electrodes. The relevant researches are summarized in **Table 3**. Folded electrode is a typical type of such configuration. Cheng et al. first demonstrated using folding paper-based electrodes to increase the areal energy density.[62] As a proof-of-concept, conventional $LiCoO_2$ and $Li_4Ti_5O_{12}$ slurries were deposited on carbon nanotube (CNT)-coated papers to prepare cathodes and anodes, respectively. After folded to a compacted

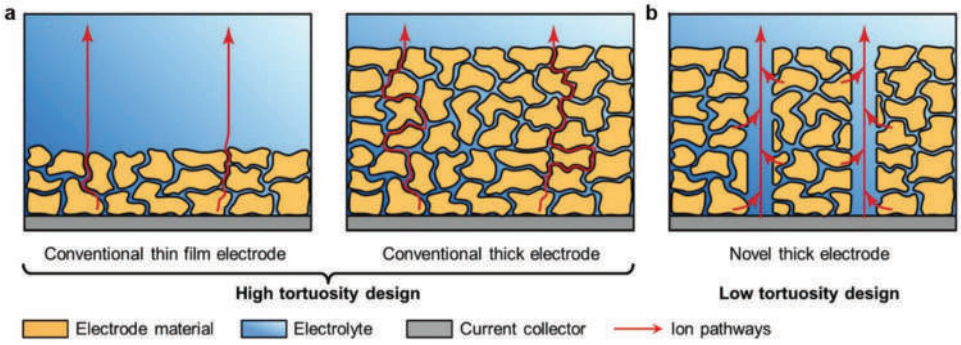

Figure 7. Comparison of ion transfer pathways in diverse electrodes. a) Illustration of ion transport distance arising from the increased thickness of conventional electrode with high tortuosity. b) Illustration of rapid ion transport in novel thick electrode with low tortuosity. Reproduced with permission.[61a] Copyright 2019, John Wiley and Sons.

stack with mass loadings increased to ≈8.8 mg cm^{-2}, the assembled full cell achieved an improved areal capacity of ≈1.3 mAh cm^{-2} after 20 cycles. To further enhance the areal lithium storage capability, researchers have developed folded electrodes based on optimized nanostructures in-situ grown on current collectors.[63] Wang et al. developed SnO_2 nanoparticle-decorated reduced graphene oxide (rGO) composite films and folded them to improve the electrode areal mass loadings (**Figure 8**).[63b] Compared to the densely stacked thick film structure (film electrode), the fold electrodes exhibited faster electrochemical kinetics and structural stability (Figure 8a,b). First, a fold electrode with the same thickness comprised many continuous thin film layer (Figure 8d) and the edges between the adjacent two layers (Figure 8e) provided extra electron transport pathways within whole electrodes. Together with the in-plane transport, the total electron conductivity of electrodes was significantly improved, as reflected in the resistance measurement results (Figure 8c). The fold electrodes showed smaller resistance increase with elevated areal mass loadings than that of the film electrodes, and the resistance of the later was ≈4.1 times higher than that of the fold electrodes at the same mass loading of 5 mg cm^{-2}. Second, the voids between the two layers not only facilitated the infiltration of electrolyte and prompted ion diffusion, but also served as buffering space to accommodate the volume expansion of active materials during charge/discharge and thereby improve cycling stability.[63] As a result, the fold electrodes with a mass loading up to 5 mg cm^{-2} achieved a high areal capacity of 3.67 mAh cm^{-2} at the 100th cycle.

Folded electrode technique is a promising strategy to manufacture high-areal-capacity thick electrode. Currently, an electrode assembly having a cathode/separator/anode structure to form a secondary battery may be broadly classified into a jelly-roll (winding type) assembly and a stack (laminate type) assembly, in terms of structure thereof. In our opinion, we might draw an analogy between folded technique and winding technique such as winding electrode in the cylindrical cell according to the manufacturing process. Both have a jelly-roll form. Therefore, the folded electrode technology has the potential for rapid mass industrial production using equipment that processes winding electrodes. Following this strategy, the folded electrode technology will demonstrate significant cost advantages. Moreover, different the detachment of the electrode and low space utility of active material (due to the lower volumetric ratio of active materials) occurred on the winding electrode, the folded electrode would exhibit higher space utility, in other word, higher volumetric energy density. In the folded electrode systems, the active materials can reach a higher volumetric ratio because there are no excess current collectors. Additionally, the folded electrodes need to be fabricated with low-tortuosity architecture which can address some electrochemical issues existed in thick electrode.

To further improve the ion transport kinetics, layer-by-layer configuration using porous current collectors are developed,[64] which can well retain electrolyte in the network structured electrodes. For example, Zheng et al. sandwiched $LiCoO_2$ between two carbon cloth to fabricate a nonplanar LIB cathode,

Table 3. The literature survey on the layered electrode configurations for high lithium storage performance.

Electrode structure	I [mA g^{-1}, mA cm^{-2}]	Cycles	M_a [mg cm^{-2}]	C_a [mAh cm^{-2}]	Refs.
CuO nanorods on folded Cu foil	–	100	12.6 (CuO)	5.32	[63a]
$Li_4Ti_5O_{12}$ and SnO_2 multilayered hetero-architectures	400	300	3.2	–	[65]
Folded SnO_2/graphene films	1.7	500	5	2.53	[63b]
$LiCoO_2$ or $Li_4Ti_5O_{12}$ slurries cast on folded CNT/PVDF-coated papers	25	20	≈8.8 ($LiCoO_2$ or $Li_4Ti_5O_{12}$)	1.3[a)]	[62]
Stacked Ge nanowire/Cu nanowire/cross-linked poly(acrylic acid)-carboxymethylcellulose sodium salt laminate	0.05	50	8.5 (Ge)	6	[64b]
	0.05	33	14.8 (Ge)	7	
Carbon cloth/$LiCoO_2$ + ketjen black carbon/carbon cloth	3	35	71 ($LiCoO_2$)	9	[64a]

[a)]Capacities for the full cells (the same below).

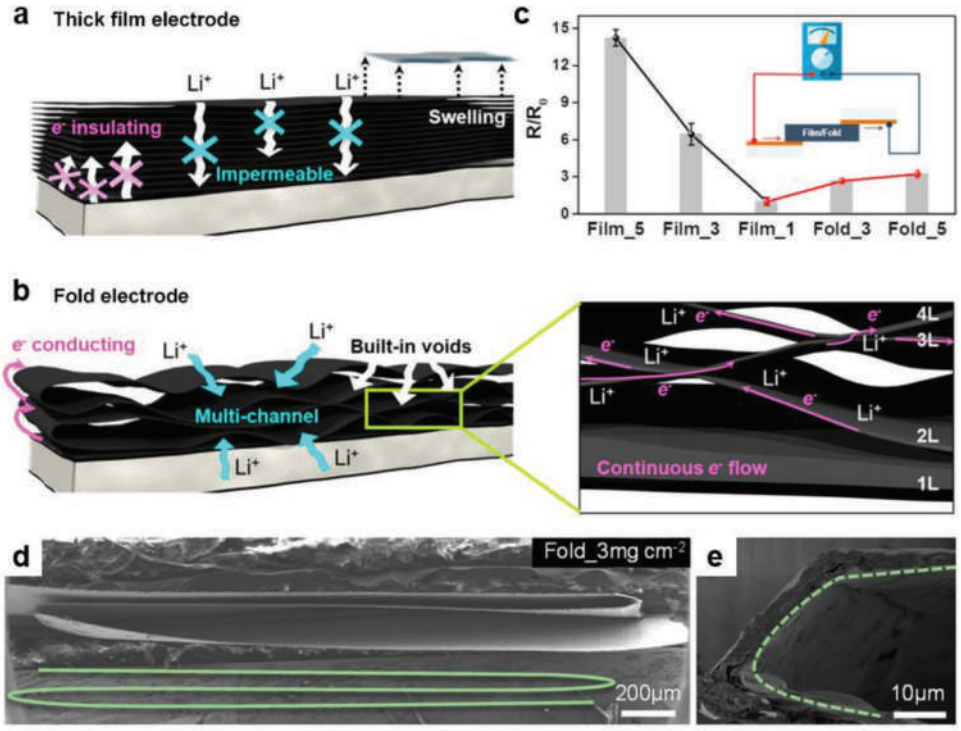

Figure 8. Layered configuration enables faster charge transport in thick electrodes. Schematic of the electrochemical behaviors in a) film electrodes and b) fold electrodes. c) Ratio (R/R_0) of electrode resistance (R) to the Film 1 resistance (R_0) for the film and fold structures with different mass loadings. Resistance is measured between the top and bottom of the electrodes as shown in the inset. For the naming rule of samples, for example, Film 3 means the film electrode with an areal mass loading of 3 mg cm^{-2} and Film 5 means the fold electrode with an areal mass loading of 5 mg cm^{-2}. d) SEM image of the cross section of the fold electrode composed of continuous fold layers. e) SEM image of the fold between the two adjacent layers. Reproduced with permission.[63b] Copyright 2018, American Chemical Society.

exhibiting a high mass loading of 71 mg cm^{-2} and areal capacity up to ≈9 mAh cm^{-2}.[64a]

As shown, layered configuration provides an effective way to enhance the electron conductivity of thick electrodes, and thereby enables higher mass loadings and areal capacities. Besides, many of them have no strict requirements on active materials, and thus can be applicable for a large range of materials. One thing to note is that the interaction of active materials and conductive current collectors in such configuration is essentially a 2-D mode parallel to the electrode plane, and the charge transport kinetics enhancement may be limited in the vertical dimension. Transforming the parallel mode into a vertically aligned electrode configuration can help resolve this issue and further improve the performance.

4.2. Vertically Aligned Structure

The effective ion diffusivity (D_{eff}) in porous electrodes can be calculated by the equation: $D_{eff} = D_0 \frac{\varepsilon}{\tau}$, where ε and τ correspond to the porosity and tortuosity of electrodes, respectively, and D_0 represents the intrinsic lithium diffusion coefficient in electrolyte.[66] As shown, D_{eff} is inversely proportional to τ. Thus, constructing structures with vertically aligned channels to reduce the tortuosity of an electrode can effectively prompt ion transport within the porous electrodes, and thereby enhance the electrochemical performance. The relevant researches are summarized in **Table 4**.

Applying a magnetic field to magnetic active materials is an innovative way for tuning their orientation in electrodes and fabricating such aligned structures. By coating Fe_3O_4 nanoparticles on graphite flakes and rotating magnetic field oriented perpendicularly to the current collector surface during slurry casting process, Billaud et al. fabricated an out-of-plane aligned graphite electrode architecture for faster ion diffusion within electrodes (**Figure 9**a).[67] Compared with the electrodes with random graphite orientation, the aligned electrodes showed a decreased tortuosity by a factor of four, which translated to an capacity improvement of ≈40%, at a loading of 9.1 mg graphite cm^{-2}.

Using a template with pre-existing vertical channels is also an effective approach to constructing aligned structures. Wood materials have intrinsically aligned pores along its growth direction, together with its high availability, low cost and renewability, making it a promising template for making such structures. For example, by sol-gel and calcination process, Lu et al. duplicated the microchannels of woods into thick $LiCoO_2$ cathode, which exhibited a tortuosity 1.5 times lower and lithium ion conductivity 2 times higher than that of the $LiCoO_2$-randomly distributed electrodes (Figure 9b).[69] As a result, a significantly improved areal capacity of 24.5 mAh cm^{-2} was

Table 4. The literature survey on aligned electrode structures for high lithium storage performance.

Type	Electrode structure	I [mA g^{-1}, mA cm^{-2}]	Cycles	M_a [mg cm^{-2}]	C_a [mAh cm^{-2}]	Refs.
Magnetic	Magnetically aligned Fe_3O_4-modified graphite flakes	≈150	50	9.1	0.93	[67]
Wood-templating	$LiFePO_4$ slurry in carbonized natural wood with vertically aligned channels	2	140	60 ($LiFePO_4$)	3.8	[68]
	Freestanding bulk $LiCoO_2$ cathode with vertically aligned channels using wood as template	≈5 ≈40	– 30	206 206	24.5 12.9	[69]
Ice-templating	MoS_2 nanoflakes on vertically aligned carbon aerogel	5000	1000	16 (MoS_2)	9.81	[70]
	Copolymer aligned structure of NMC_{811} secondary particle	≈35	50	50	8.84	[71]
	$LiFe_{0.7}Mn_{0.3}PO_4$ nanoplates on 3-D graphene frameworks with aligned vertical channels	2.46	500	21.2	1.77	[72]

attained at an ultra-high areal mass loading of 206 mg cm^{-2}. In the future studies, a simpler and controllable process is required to obtain the wood templates, as the pre-treatment of natural wood to obtaining a clean aligned porous network is usually a complex work for now.[74]

Freeze-casting is another method to template the pore structures in materials. By nucleating and growing ice crystals along the temperature gradient from one side of precursor, followed by a freeze-drying process, anisotropic pore channels in a replica of the sublimated ice crystals are formed in the products (Figure 9c). In ice-templating process, the final structures can be flexibly controlled by various parameters like concentration, cooling speed, etc.[75] to tune the ion transport behaviors in electrodes. Following this approach, vertically aligned graphene frameworks and carbon aerogels have been fabricated to load $LiFe_{0.7}Mn_{0.3}PO_4$ nanoplates[72] and MoS_2 nanoflakes,[70] respectively, to achieve high-areal-mass loading LIB electrodes. Note that, ascribed to the introduction of water, freeze-casting may not be suitable for the water-sensitive materials, such as part of LIB cathodes like $LiCoO_2$ and NMC.

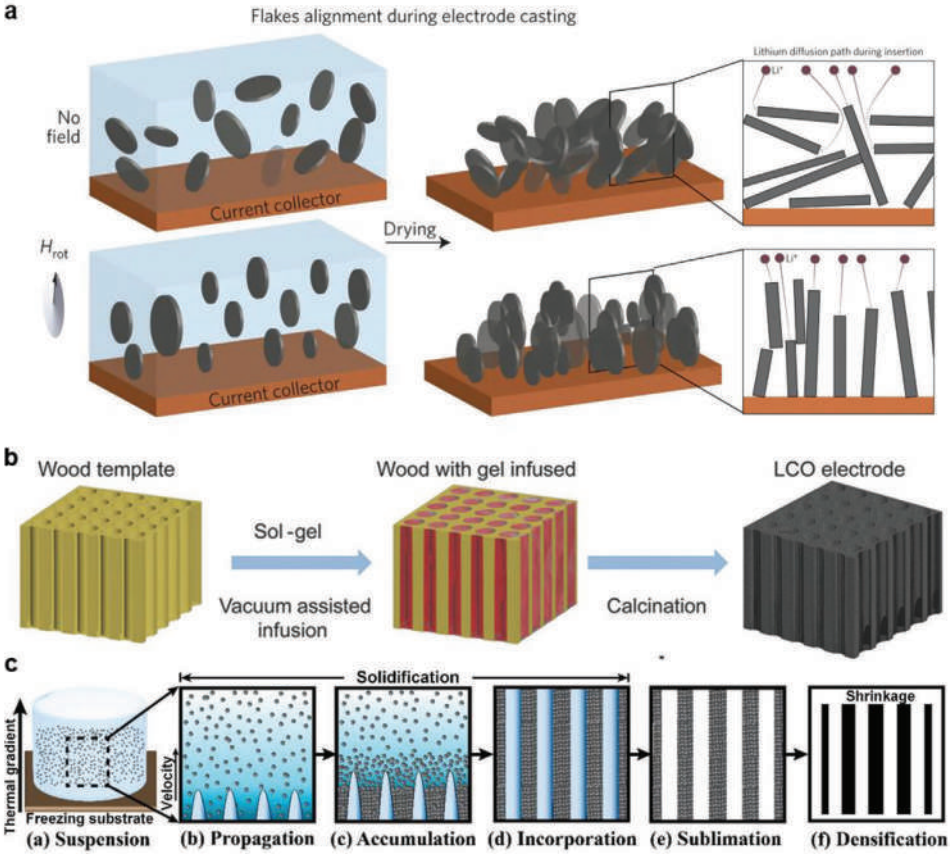

Figure 9. Aligned structure with low tortuosity for thick electrode designs. a) Schematic of the fabrication of magnetically aligned graphite electrodes. Reproduced with permission.[67] Copyright 2016, Springer Nature. b) Schematic of the fabrication of the $LiCoO_2$ electrodes with vertically aligned channels using wood templates. Reproduced with permission.[69] Copyright 2017, John Wiley and Sons. c) Schematic of freeze-casting approach for forming aligned pore structures. Reproduced with permission.[73] Copyright 2018, Elsevier.

Table 5. The literature survey on constructing percolating conductive network to composite with active materials for high lithium storage performance.

Type	Electrode structure	I [mA g^{-1}, mA cm^{-2}]	Cycles	M_a [mg cm^{-2}]	C_a [mAh cm^{-2}]	Refs.
	Segregated network composite of CNT with Si and $LiNi_{0.8}Mn_{0.1}Co_{0.1}O_2$ particles	0.54 0.8	2 10	14.3 156	45 29	[76]
	Micrometer-size bulk-porous Si/carbonized polyacrylonitrile composites	200	50	1.6	3	[79]
	Si nanoparticle/carbon shell pomegranate microbeads mixed with CNT	0.7	100	3.12 (Si+C)	3.1	[37]
	Mesoporous $Li_3V_2(PO_4)_3$ interweaved with CNT nest	1000	200	8.4 ($Li_3V_2(PO_4)_3$)	0.76	[80]
	Intertwined ultrathin $H_2V_3O_8$ nanoribbons and self-coiled nanoscrolls/CNT film	4000 0.91	1000 –	3.1 13	0.51 2.7	[81]
	$LiCoO_2$/CNT paper coated with Al_2O_3	155	–	40 ($LiCoO_2$)	5.6	[82]
	$LiFePO_4$ particles distributed within 3-D polyacrylonitrile nanofiber framework interlaced with CNT	0.2	50	78.9	11.5	[83]
Physical mixing with carbon fiber	Carbon fiber percolation network with $LiCoO_2$ or graphite microparticles supported on a pierced and serrated current collector	–	–	–	19.8 24.1	[11a]
Physical mixing with graphene	MoS_2 microparticles/rGO film	100	200	8.2	2.8	[84]
	$H_2V_3O_8$ nanobelts/reduced graphene oxide percolation network	100	50	8.3	1.45	[85]
	TiO_2 nanoparticles/CNT/graphene sheet film	0.05	100	3.79 (TiO_2)	0.81	[86]
	ZnO nanomembrane within carbon foam	250 2000	100 100	7.78 (ZnO) 7.78 (ZnO)	3.42 2.02	[87]
Slurry infiltration in porous substrate	$LiFePO_4$ slurry in NiCrAl foams	Charge ≈65, discharge ≈130	20 20	47.5 ($LiFePO_4$) 77 ($LiFePO_4$)	5.2 4.4	[88]
	$LiFePO_4$ slurry in NiCrAl foams with different cell sizes	1	50	56.3 ($LiFePO_4$)	9	[89]
	$LiCoO_2$ or graphite slurry in Al or Cu foam	0.38	–	138 ($LiCoO_2$) 55 (graphite)	16.7[a)]	[90]
	$Li_4Ti_5O_{12}$ or $LiFePO_4$ slurry in the CNT-polyester textile	≈18 –	350 –	145 ($Li_4Ti_5O_{12}$) 168 ($LiFePO_4$)	≈21.7 –	[91]
	$Li_4Ti_5O_{12}$ or $LiCoO_2$ + rGO + PTFE binder slurry, roll-pressed with carbon fabric	≈70 ≈35	100 100	≈7.5 ($Li_4Ti_5O_{12}$) ≈7.5 ($LiCoO_2$)	1.09 1.02	[92]
	FeOF/TiO_2 hetero-nanostructures within CNT sponges	100	100	8.7	1.48	[93]
	Reticulate dual-nanowire aerogel composed of FeS_2 nanowires and carbon nanotubes	500	100	14.4	10	[94]
	Electrophoretic deposition of $LiFePO_4$ onto 3-D carbon fiber cloth	≈17	100	20 ($LiFePO_4$)	2	[95]
Electrospun	Electrospun Si nanoparticle/carbon black/poly(acrylic acid) fiber mate	≈300	50	3.49	3.1	[96]
	Electrospun TiO_2/carbon nanoparticles/poly(acrylic acid) fiber mat	≈33.5 ≈335	– –	54.1 54.1	3.9 2.5	[97]

For the templating method, an important but often ignored part is the structural stability of the formed aligned network under high vertical pressure. It can be a potential problem in both wood-templated structures due to the generally limited mechanical strength of carbon materials, and ice-templated structures with weak interaction among active materials, and thus requires further studies. On the other side, replacing the 2-D structure (either vertical or parallel) with a 3-D network configuration is a promising strategy to enhance the electrode kinetics and electrochemical performance.

5. Introducing 3-D Porous Conductive Network

Incorporation of active materials with a 3-D porous conductive network enlarges the contact area of current collector/active materials/electrolyte interfaces, enabling faster electron transport and shortening ions diffusion pathways.[34] As a result, the decreased cell polarization contributes to an improved capacity and cycling stability. The built-in host framework also promotes the mechanical properties of electrodes and contributes to more stable battery performance.

Following this approach, introducing a secondary percolating network is a simple way to construct the 3-D porous conductive matrix (**Table 5**). It is a physical process in most of cases and applicable for a variety of materials. Due to the relatively low cost and reasonable electron conductivity, carbon black particles are used to form the conductive percolating network in traditional slurry-casted electrode coatings. However, the contact among different carbon black particles or between active materials and carbon black is generally in point-to-point form which is area-limited and unstable. It leads to low and inhomogeneous electron conductivity and thus limits the electrochemical performance, especially for thick electrodes.[76]

Constructing carbon/active materials hybrid nanostructures can transform the high-impedance contact between active materials and carbon black to the carbon-carbon contact with relatively lower impedance, and thereby improve the electron transport within the electrodes.[34b,35,43b,c,77] Kuang et al. developed another strategy to enhance the performance.[78] They innovatively constructed a conductive network of carbon black particles by electrostatic assembly of neutral carbon black particles on negatively charged cellulose nanofibers. The decoupled electron and ion transport pathways enabled a high areal capacity of 8.8 mAh cm^{-2} at mass loading up to 60 mg cm^{-2}.

For the inferior electron conductivity in electrodes with carbon black particles as conductive agents, the root cause is their 0-D structure-induced short-range, discontinuous and unstable electron transport in electrodes. Constructing an intertwined network based on 1-D or 2-D carbon additives subunits, which has a lower electrical percolation threshold due to longer electron transport along certain dimensions, can significantly improve the performance.

To this end, it is a common approach of physically mixing active materials with 1-D or 2-D carbon additives followed by slurry casting or vacuum filtration. Park et al. proposed high-areal-capacity thick battery electrodes enabled by CNT segregated network/active material microparticles composites (**Figure 10**a).[76] As a typical example of such hybrid structure (Figure 10b,c), after simply physical mixing, micro silicon particles (μ-Si) were wrapped by membranes composed of entangled CNT bundles/ropes and formed the μ-Si/CNT electrodes. Compared with traditional slurry based on polymeric binders and carbon black additives, which could easily form cracks after drying for thick electrodes, the segregated CNT network resulted in a larger cracking thickness (CCT) and more robust electrode due to its significantly enhanced mechanical toughness (Figure 10d). Together with the highly conductive 3-D CNT matrix, the silicon and NMC-based composite electrodes achieved mass loadings up to 14.3 and 156 mg cm^{-2}, leading to ultra-high areal capacities of ≈45 and 29 mAh cm^{-2}, respectively (Figure 10e). Other similar structures using 1-D carbon fibers or 2-D graphene to construct percolating framework have also been reported, such as $LiCoO_2$/carbon fiber supported on pierced and serrated current collectors[11a] and MoS_2 microparticles/rGO composite films.[84]

Physically mixing active materials and conductive additives is an easy method to construct 3-D hybrid network. However, its mechanical stability may remain a problem due to the weak physical interaction among the subunits of the network, which could be broken or collapse under external forces during the manufacturing process (Figure 2b). Making hybrids based on pre-existing 3-D porous substrates is a promising way to enhance the mechanical properties of the electrodes. The simplest way is direct slurry interpenetration in carbon matrix [91,92] or metal foams.[88–90,98] But it still requires binders to make slurries, which may increase the portion of inactive components and also block electron conduction in electrodes. Directly growing or depositing active materials within the network[87,93–95] is an alternative approach. For example, by growing FeS_2 nanowires within carbon nanotube sponges via a solvothermal method, our group fabricated a reticulate FeS_2/CNT dual-nanowire aerogel as a free-standing LIB anode, which yielded a high areal capacity of 10.0 mAh cm^{-2} at a mass loading of 14.4 mg cm^{-2} after 100 cycles.[94]

Electrospinning is another method for constructing 3-D porous network structure with high mass loadings. Different from casted monolithic 2-D coatings in conventional electrodes, the slurry (e.g., Si nanoparticle/carbon black/PAA[96] and TiO_2/carbon nanoparticles/PAA[97]) is electrospun to a fiber mat composed of continuous nanofibers and controlling the substrate movement enables geometry tuning of the formed network. By confining materials in a single long fiber, the intact contact between active materials and conductive matrix prompts the electron conductivity in both radial and axial directions of the fiber. Besides, the intra- and interfiber void space in the mat facilitates the infiltration of electrolyte and shorten the ion diffusion pathways. As a result, the charge transport throughout the whole electrodes is significantly improved. Besides, the electrospinning technique is a relatively universal fabrication method applicable for diverse types of active materials, due to its low requirement on the precursor—even conventional electrode slurry is qualified. However, the low throughput is hindering the commercialization of electrospinning mat electrodes for now.

In the percolating network electrodes, the active materials and conductive skeletons generally interact in a physical point-to-point/line/plane way, leading to a relatively higher electrical impedance. In addition, the surfaces of the conductive matrix do not get full contact with the materials, resulting in a lower utilization of such matrix. In situ growing nanostructures on 3-D substrate have been extensively studied to mitigate these issues and further improve the electrochemical kinetics in the thick electrodes (**Table 6**). In addition to the general advantages, the in-situ composition of active materials and substrates in this case endows electrodes more functionalities (**Figure 11**). First, the conductive 3-D substrate plays a role of current collector, conductive agents and binder at the same time, decreasing the amount of inactive components in electrodes as much as possible. Second, the in situ growth results in more closed and stable contact between active materials and conductive substrate, enabling faster and more durable electron transport. Third, the growth usually occurs on a single subunit like a nanotube or nanosheet, which can notably increase the utilization of the inside network of substrate and raise the loadings of active materials; meanwhile, the resultant hybrids can inherit the original porous structure of the substrates which efficiently facilitates the ion transport within electrodes.

Porous metal such as nickel foams,[103,104] copper foams,[102] and dealloyed nanoporous metals[101] have been investigated as substrates to load active materials. For example, Li et al. deposited NiO nanoflowers on NiO interlayer-coated nickel foam to form a 3-D NiO@NiO/nickel network, and achieved a high areal capacity of 1.45 mAh cm^{-2} at 1.2 mA cm^{-2} after 100 cycles.[103] The high intrinsic electron conductivity of metal facilitated the electron transport within thick electrodes and their high mechanical strength enabled a well-maintained framework during cycling. Nevertheless, there are also issues associated with the use of metal substrates. First, its relatively high density leads to an increased inactive weight in electrodes and could reduce the total energy density at cell level. Besides, the metal burrs may pierce the separator especially under high pressure during cell assembly, which may cause

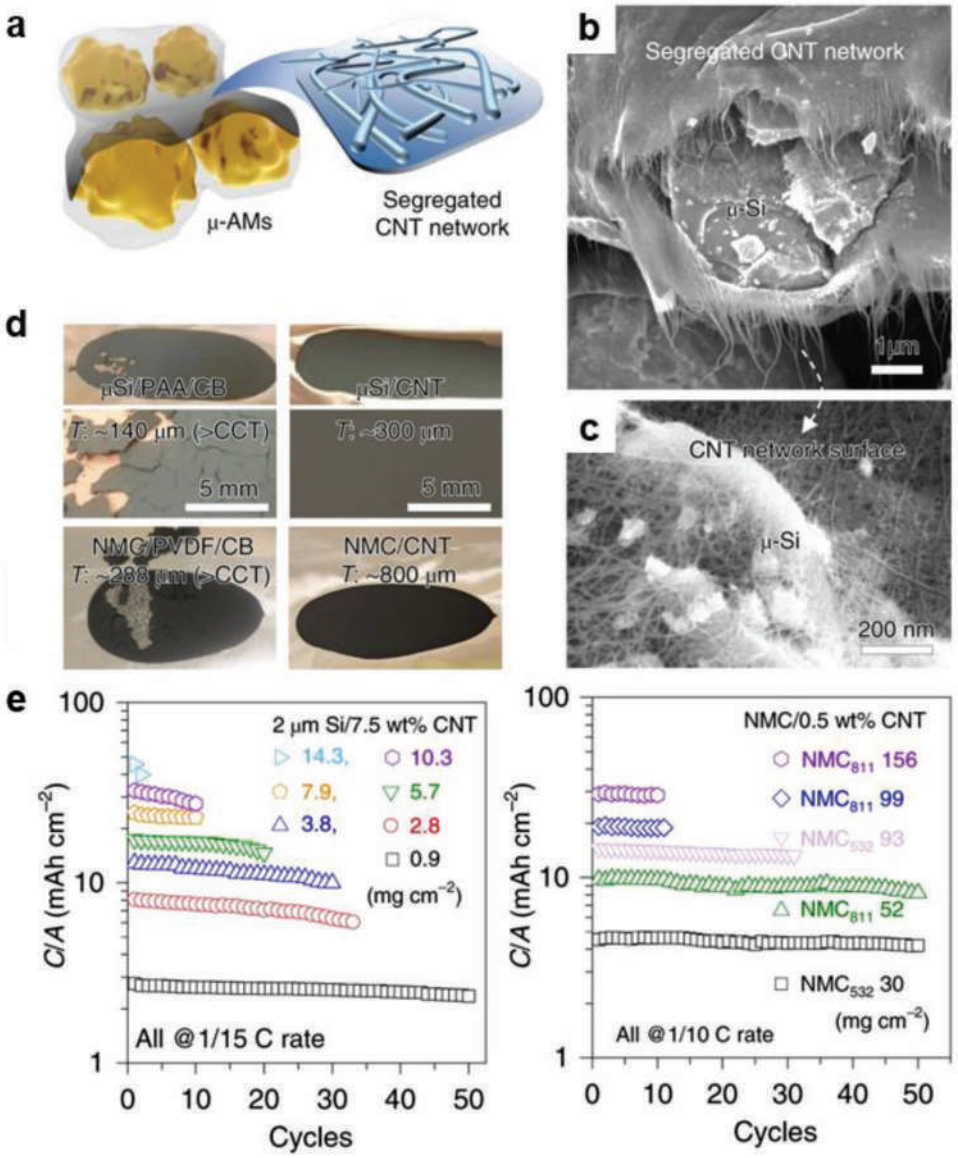

Figure 10. Segregated carbon nanotube network enables high-areal-capacity electrodes. a) Schematic of the electrode composition of segregated CNT network and active material microparticles (μ-AMs). b,c) SEM images of the silicon microparticles (μ-Si)/CNT composite anode. d) Photographs of the thick silicon and NMC electrodes based on traditional active material-polymeric binder-carbon black additives composition (left) and the proposed hybrid network structured electrodes (right). PAA and CB represent polyacrylic acid and carbon black, respectively. T represents the thickness of the electrode coating. e) Areal capacities of the proposed electrodes based on composites of 2 μm Si microparticles with 7.5 wt% CNT addition (2 μm Si/7.5wt% CNT) and $LiNi_{0.8}Mn_{0.1}Co_{0.1}O_2$ (NMC811) microparticles with 0.5 wt% CNT addition (NMC/0.5wt% CNT), at different areal mass loadings. Reproduced with permission.[76] Copyright 2019, Springer Nature.

safety risks. Metal materials like Al and Cu also suffer from corrosion caused by organic electrolytes containing $LiPF_6$ during cycling.,[82] affecting the durability of the metal substrates. One way to resolve these issues is to replace metal substrates by lighter, softer, and chemically inert carbon materials.

Porous carbon network composed of 1-D subunit like carbon nanotube and carbon fiber is a promising candidate. Such 1-D subunits act as relatively long-range electron conductors and porosity enhancers due to their linear shapes distributed in the electrodes,[125] which enables high electron conductivity and generates enough pores for electrolyte infiltration even at highly compacted state. Attributed to the large surface area, high intrinsic conductivity, good flexibility and low density, carbon nanotube (CNT) has been used as substrate to load active materials, such as V_2O_5[107] and Si[106] nanoshells. Compared with CNT, carbon fibers have relatively lower cost and large-scale production capability, and thus have also been investigated extensively for coating various materials, including metal oxides,[109,112,113] sulfides,[111] vanadates,[110] etc. to achieve high mass loadings.

In addition to the carbon network assembled by 1-D subunits like CNTs or carbon fibers, graphene-based 2-D structures

Table 6. The literature survey on the in situ grown nanostructures on 3-D porous and conductive substrates for high lithium storage performance.

Substrate type	Electrode structure	I [mA g^{-1}, mA cm^{-2}]	Cycles	M_a [mg cm^{-2}]	C_a [mAh cm^{-2}]	Refs.
Metal-based	Cu_3P-Ni_2P-NiO heterogenous coated on Ni foam	1	100	–	3	[99]
	3D bicontinuous nanostructured polyimide-based nanoparticles/Ni	15 000	250	–	–	[100]
	3-D nanoporous network composed of NiCuMn@oxide core@shell structures with oxygen vacancies and Cu doping supported by an intercalary Cu film	1	100	6.9 (NiCuMn oxide)	6.1	[101]
	FeO_x porous nanoblocks array on Cu foam	0.25	50	2.5 (FeO_x)	3.33	[102]
	Outer few-layer NiO nanoflowers@medial NiO layer@Ni foam	1.2	100	–	1.45	[103]
	Thick mesoporous Co_3O_4 nanosheet on Ni foam	0.74	30	4.15 (Co_3O_4)	4.39	[104]
CNT based	Carbon-encapsulated Fe_3O_4 nanospheres anchored on CNT network	4	500	0.8	0.32	[99]
	CNT sponge grafted with Co_3O_4 nanoparticles	200	30	14.3	12	[105]
	Silicon-CNT coaxial sponge	≈840	50	8	8.8	[106]
	CNT/V_2O_5 core/shell sponge	1.1	100	≈3.8 (V_2O_5)	2.66	[107]
	$LiMn_2O_4$@C grown on CNT	≈100	1000	2	0.11	[108]
Carbon fiber-based	$LiMn_2O_4$@C grown on carbon nanofiber	≈100	1000	2	0.18	[108]
	Carbon fiber cloth coated with exfoliated porous N-doped carbon fiber, NiO nanosheets, and carbon quantum dots	3	250	10.58	2.91	[109]
	$Mn_2V_2O_7$ nanobelts@carbon cloth	200	50	3.5	4.04	[110]
	$Co_3V_2O_8$ nanobranch@carbon cloth				5.87	
	$Cu_3V_2O_8$ nanoparticle@carbon cloth				3.57	
	$Ni_3V_2O_8$ nanoparticle@carbon				4.76	
	MoS_2 nanoflakes grown on the twine carbon fibers of the carbonized cotton cloth	2.5	35	4.4 (MoS_2)	5.2	[111]
	VO_2 nanobelt arrays on carbon fiber cloth	100	100	5.2 (VO_2)	0.72	[112]
	V_2O_5 nanosheet arrays on polydopamine-decorated carbon cloth	300	100	2.1 (V_2O_5)	0.25	[113]
Graphene based	Si particle wrapped in multiple graphene shells	1000	200	4	≈0.5	[114]
	MoS_2/carbon hybrids on graphene foam	100	100	12	7.21	[115]
		100	100	3	1.79	
	Fe_2O_3 nanowires on graphene ribbons	500	100	4	4.24	[116]
		2000	1000	4	2.72	
		5000	3000	4	1.68	
	3-D holey graphene frameworks	8	2000	4	5	[117]
	SnO_2 microparticles/3-D holey graphene frameworks	2.4	400	12	9.5	[118]
	SnO_2 nanoparticles/3-D holey graphene frameworks	500	1000	4	2.9	[119]
		2000	2000	4	2.3	
	Holey Fe_2O_3 nanosheets grown on the holey rGO nanosheets	200	120	3.1	4.65	[120]
		5000	1600	3.1	3.1	
	Nb_2O_5@3-D holey-graphene framework composites	0.5	–	22	3.9	[121]
		2000	10 000	6	1	
Other carbon-based	Red P wrapped in an engineered carbon host	16 700	1000	≈1	≈0.5	[122]
	Ge nanoparticles encapsulated in a 3-D double N-doped ultrathin graphite/void/ultrathin graphite tube network	≈16	100	10	7.71	[123]
	Ordered mesoporous TiO_2/carbon hybrids	25	55	26.4	4	[124]

are also promising substrates to load active materials. Such 2-D substrate generally shows a high in-plane electron conductivity and can facilitate electron transport in this dimension. Furthermore, compared to the 1-D structure with cylindrical surface, the relatively flat 2-D plane allows higher loading of active materials and is adaptive to different types of nanostructures. However, large 2-D sheets tend to form compact stack structures and affect the ion diffusion within the electrodes, especially at large mass loadings under high pressure. Ke et al. found that a higher content of graphene additives prolongs the ion diffusion pathways in thick $LiFePO_4$ electrodes and results in poorer electrochemical performance than those with 0-D Super P additives.[126]

To circumvent the problem, researchers have developed graphene ribbons[116] with decreased 2-D dimension sizes, holey graphene with engineered in-plane pores,[118–121] and

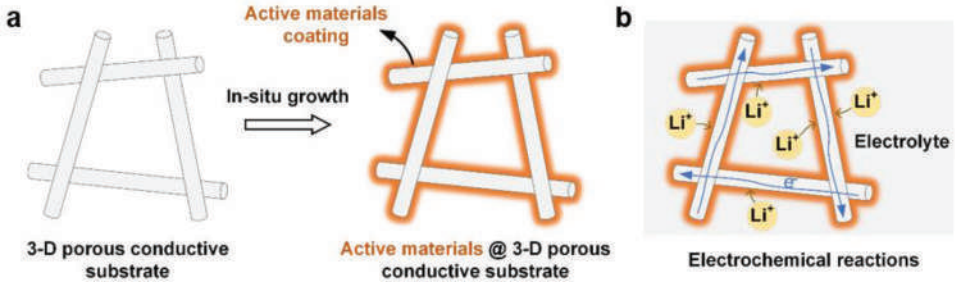

Figure 11. Schematic of the concept of in-situ growing active materials on 3-D porous conductive substrate for enhancing areal lithium storage performance. a) Illustration of the in-situ growing process to fabricate a 3-D network structured hybrid electrode. b) Rapid electron transport through the conductive skeleton and shortened ion diffusion pathways in the porous electrodes.

macroporous graphene network[115] as substrate to avoid forming densely stacked sheets. For example, Sun et al. developed 3-D holey-graphene/Nb_2O_5 composite architectures to enhance the charge transport rate at high mass loadings (**Figure 12**a).[121] By etching graphene sheets (Figure 12b) to introduce micro- and mesopores (Figure 12c), together with the deposition of Nb_2O_5 (Figure 12d) and a self-assembly process to form macro-pores, a free-standing hybrid foam (Nb_2O_5/HGF) consisting of hierarchical porous structures (Figure 12e) was developed. Compared with the bare Nb_2O_5-graphene composites (Nb_2O_5/G) without the hierarchical pores, the Nb_2O_5/HGF structure exhibited significantly improved ion diffusion throughout the whole electrode

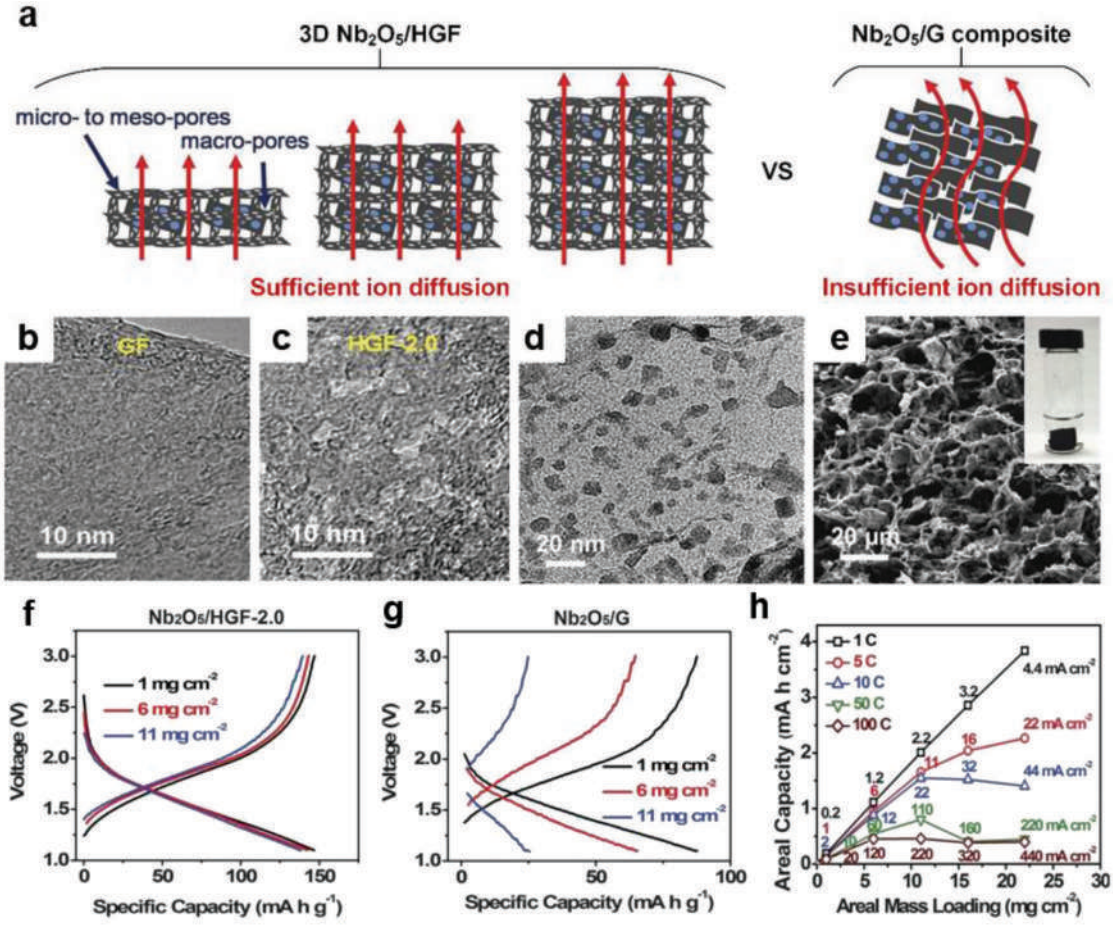

Figure 12. Holey graphene network enables high-areal-capacity lithium storage. a) Schematic of ion diffusion in 3-D Nb_2O_5/HGF and Nb_2O_5/G composite electrodes. SEM images of b) the pristine graphene (GF) sheets, c) holey graphene (HGF) sheets, d) Nb_2O_5 nanoparticles decorated graphene, and e) 3-D porous Nb_2O_5/HGF framework with the inset photo of the free-standing monolithic hybrid foam. Voltage profiles of f) the 3-D Nb_2O_5/HGF and g) Nb_2O_5/G electrodes with areal mass loadings of 1, 6, and 11 mg cm^{-2}, at a rate of 10 C. h) The relationship between areal capacities and mass loadings at different rates. HGF-2.0 represents the holey graphene framework prepared by H_2O_2 etching for 2.0 h. Reproduced with permission.[121] Copyright 2017, American Association for the Advancement of Science.

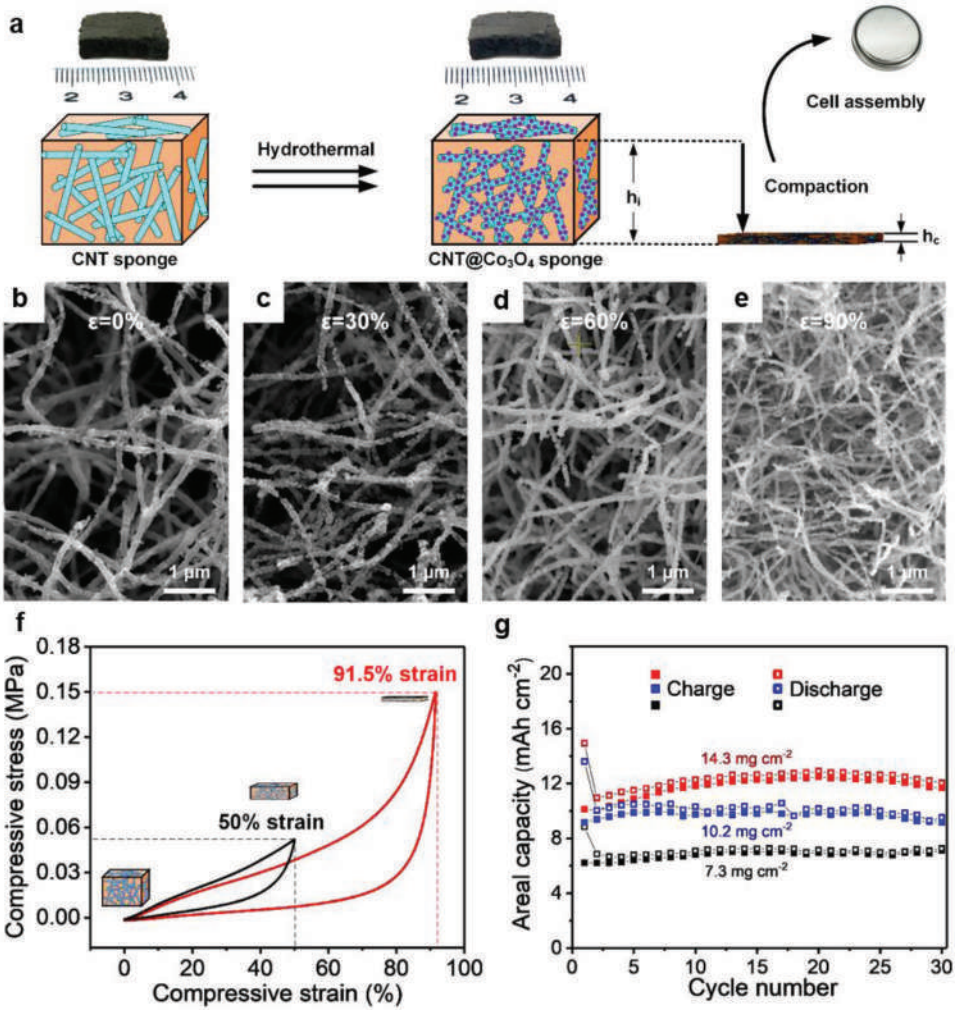

Figure 13. Compressible CNT@Co_3O_4 sponges for high-areal-capacity lithium storage. a) Schematic illustration of the fabrication process of the CNT@Co_3O_4 sponge electrodes and compaction for cell assembly. SEM images of the CNT@Co_3O_4 sponges at different compressive strains of b) $\varepsilon = 0$, c) 10%, d) 60%, and e) 90%. f) Stress–strain curves of the hybrid sponges (at compressive strain $\varepsilon = 50\%$ and 91.5%). g) Areal capacities of the hybrid sponge electrodes with different areal mass loadings at 200 mA g^{-1}. Reproduced with permission.[105] Copyright 2018, John Wiley and Sons.

architecture (Figure 12a). As a result, the gravimetric capacity of Nb_2O_5/HGF still maintained at 139 mAh g^{-1} at a loading of 11 mg cm^{-2}, only 7% less than that at 1 mg cm^{-2} (Figure 12f). While for Nb_2O_5/G, the capacity decreased drastically from 85 to 25 mAh g^{-1} (Figure 12g). With the mass loading further pushed to 22 mg cm^{-2} in thicker electrode, an areal capacity as high as 3.9 mAh cm^{-2} was attained (Figure 12h). The impressive performance demonstrated in the Nb_2O_5/HGF composite electrodes showed that in-situ depositing active materials in a holey graphene framework with a hierarchical porous structure were effective strategy to improve the areal lithium storage capability. Other carbon networks, like double-walled ultrathin graphite tube-assembled scaffold[123] and block copolymer-templated continuous carbon matrix[124] have also been developed as substrates.

As shown in the above discussion, in situ growing nanostructures of active materials on 3-D porous metal or carbon substrates represent an effective approach to enhancing the mass loadings and areal lithium storage performance. And in practice, the stability of the constructed network is very important to make sure the advantages of the proposed structures can be inherited after cell assembly and during battery operation. Our group has reported a high-areal-capacity LIB anode[105] based on compressible CNT@Co_3O_4 sponges. The composite contained Co_3O_4 nanoparticles uniformly grafted on 3-D porous CNT skeletons fabricated by a hydrothermal process (**Figure 13**a). The hybrid network inherited the compressibility of the CNT substrate and could be compacted to a thin film for cell assembly, which allows us to use thick sponges to increase the electrode mass loadings. The SEM images (Figure 13b–e) of the hybrid network at increasing compression degrees indicated that the 3-D porous network and the coating structure were well-maintained during the densification process, which was significant for the electron and ion transport in the compacted electrodes with high loadings. The stress-strain curves (Figure 13f) show that the structure can sustain up to 91.5% compressive strain (corresponding to a densification ratio ≈11.7) and recover after releasing loads, further indicating the highly stable networked structure of the sponge. Owing to the robust hybrid network

Table 7. The literature survey on the novel manufacturing techniques for electrodes with high lithium storage performance.

Technique	Electrode structure	I [mA g^{-1}, mA cm^{-2}]	Cycles	M_a [mg cm^{-2}]	C_a [mAh cm^{-2}]	Refs.
Immersion precipitation	Freestanding $Li_4Ti_5O_{12}$/Super P/PVDF electrode	175	–	24	3.7	[20]
		175	100	14	1.95	
UV curing	$LiNi_{0.5}Mn_{0.3}Co_{0.2}O_2$/carbon black/radiation curable binder (acrylated polyurethane resin)/carboxymethyl cellulose	–	–	25	4	[127]
Powder extrusion molding	Additive-free $Li_4Ti_5O_{12}$ and $LiFePO_4$ electrodes	≈14.2	10	110	11.1	[128]
		≈14.2	6	90	11.1	
	$Li_4Ti_5O_{12}$/C pellets	7.3	20	138	15.2	[129]
Cold-pressing	Ti_3C_2 and Nb_2C pellets	30	50	50	5.9	[130]
					6.7	
Spark plasma sintering	Thick porous $LiFePO_4$/C or $Li_4Ti_5O_{12}$/C composite electrodes using NaCl microsize particles as template	≈8.5	20	≈150	21	[131]
		≈8.5	15	≈150	18	
3-D printing	Printing ink: $LiFePO_4$ + acetylene black + CNT + PVDF-HFP in NMP	–	17	50	7.5	[132]
	Printing ink: $LiFePO_4$ or $Li_4Ti_5O_{12}$ + Ketjenblack carbon + 1 M LiTFSI/propylene carbonate solution + PVP	0.2	46	108 ($LiFePO_4$)	≈10.5[a)]	[133]
	Printing ink: $LiFePO_4$ + CNT + CMC in water	1.088	100	32	5.05	[134]
	Printing ink: FeO_X coated $LiMn_{1.5}Ni_{0.5}O_4$ particles + carbon black + PVDF in NMP	≈20	100	25	2.1	[135]
	Printing ink: silver nanowires + graphene + $Li_4Ti_5O_{12}$ in water	1.06	50	30	4.61	[136]
Laser structuring	Laser-structured line patterns on electrodes	–	–	54.7	9	[137]
	Laser-structured line patterns on electrodes	≈18	5	41.1	5.34	[138]

prompting electrochemical kinetics, the electrode mass loadings and areal capacities can be lifted stepwise by using thicker sponges (Figure 13g). And finally, a high areal capacity of 12.0 mAh cm^{-2} was achieved, about three times that of the conventional graphite anodes.

6. Novel Manufacturing Techniques for Thick and Porous Electrodes

The abovementioned approaches mainly focus on the material-level optimization to improve the electrode mass loading and areal capacities. The rapidly developing manufacturing technologies have provided new tools for engineering thick electrodes to improve their mechanical and electrochemical properties (**Table 7**).

The solvent evaporation in traditional electrode manufacturing is a main cause of cracking and delamination problems in thick electrodes (Figure 2a). Developing other methods to solidify binders in slurries, such as immersion precipitation[20] and electron beam curing,[127] can avoid the drying process and accompanying problems. Besides, electrode fabrication can directly start from powders without involving liquid slurries by cold-pressing[130] and powder extrusion molding.[128,129] Although the mechanical properties are enhanced by these new fabrication routes, the electrochemical kinetics issues in the resultant 2-D thick electrodes remain problematic.[11a] Introducing extra pores during manufacturing to construct a 3-D porous network in the coatings can facilitate the electrolyte infiltration, buffer the volume changes of active materials and thereby promote the electrode performance. For example, by forming dense active materials/NaCl composite pellets using spark plasma sintering technique followed by leaching of NaCl in water, Elango et al. fabricated thick porous $LiFePO_4$ cathodes and $Li_4Ti_5O_{12}$ anodes (≈1 mm thick) with ultrahigh mass loadings of 150 mg cm^{-2} (**Figure 14**a).[131] The large porosity (40%) and uniformly distributed pores throughout the bulk electrodes enabled faster lithium diffusion (Figure 14b). As result, the assembled full cells based on the thick electrodes exhibited high areal capacities >18 mAh cm^{-2} (Figure 14c).

3-D printing has attracted increasing attention from battery community. By extruding inks containing active materials to substrates layer by layer, a 3-D porous object based on a computer-aid design model can be created. It shows excellent process flexibility and geometry controllability,[140] and can easily create porous structures for high-areal-mass-loading electrodes. The high movement accuracy also makes it suitable for microdevices like on-chip integration of thin film batteries. Wang et al. achieved free-standing 3-D $LiFePO_4$ structures as LIB cathodes by printing the ink composed of commercial $LiFePO_4$ nanoparticles, acetylene black and CNT dispersed in NMP, followed by a water coagulation bath and freeze-drying process (Figure 14d).[132] Electrodes with three different circle-shaped patterns (grid, ring, and line) were created (Figure 14e). The layer-by-layer printing allowed an increased electrode thickness with well-maintained structures. As a result, a high areal capacity of ≈7.5 mAh cm^{-2} was achieved in an ultrathick (1500 µm) eight-layer line-patterned $LiFePO_4$ electrode with a mass loading up to ≈50 mg cm^{-2}. Besides designing various patterns, optimizing ink by using rationally designed active material nanostructures[135] or introducing highly conductive additives[136] can further enhance the electrode performance. 3-D printing is a universal method for various inorganic or organic materials, making it applicable for both cathodes and

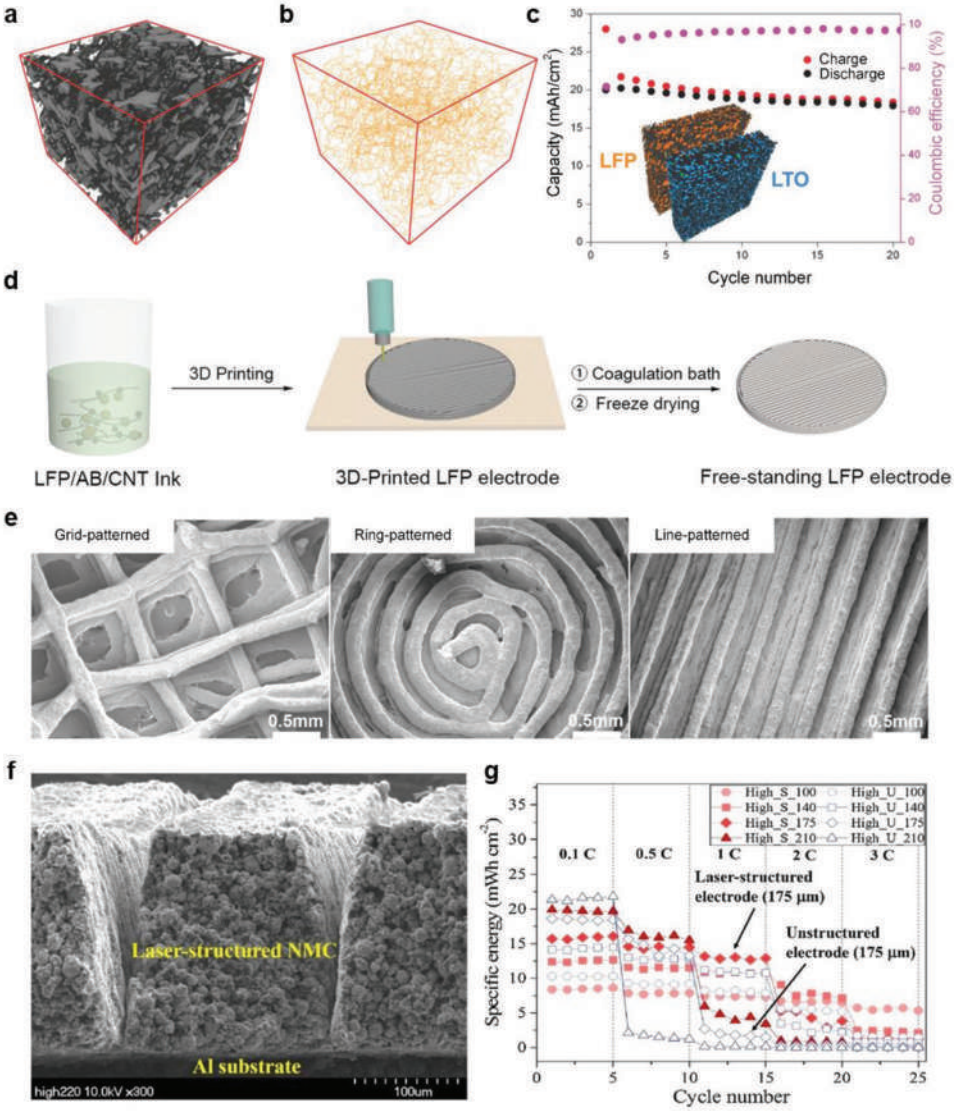

Figure 14. Novel manufacturing techniques for thick and porous electrodes. a) Tomography images of the thick $Li_4Ti_5O_{12}$ anodes, showing its typical porous structures after leaching of NaCl templates. The $LiFePO_4$ electrodes had similar results. b) Tomography skeleton of the thick $Li_4Ti_5O_{12}$ anodes, showing the well-interconnected pores that provide promising lithium diffusion pathways. The $LiFePO_4$ electrodes had similar results. c) The cycling performance of the $LiFePO_4/Li_4Ti_5O_{12}$ full cell at C/20 rate. The inset shows the tomography images of the electrodes, with solid matter in black, pores in orange and light blue for $Li_4Ti_5O_{12}$ and $LiFePO_4$, respectively. Reproduced with permission.[131] Copyright 2018, John Wiley and Sons. d) Schematic of the fabrication of 3-D structural electrodes by 3-D printing process. e) SEM images of the printed electrodes with different patterns. Reproduced with permission.[132] Copyright 2018, American Chemical Society. f) SEM image of the laser-structured $LiNi_{0.5}Mn_{0.3}Co_{0.2}O_2$ electrodes. g) Areal specific energies of structured and unstructured electrodes with thicknesses of 100–210 μm at different rates. Reproduced with permission.[139] Copyright 2019, Elsevier.

anodes in batteries[134] and even separators, and packing materials, which enables fully 3-D printed and packaged LIBs.[133] For now, limited scalability is one big issue for 3-D printing technique due to its nature of additive manufacturing, compared to the one-step slurry coating.[23] The precise control in high-resolution 3-D printers is even more time-consuming in thick electrodes fabrication. Developing more advanced printers to shorten the fabrication process and produce hierarchically porous structures is essential for the practical application of 3-D printing in the future.[141]

Laser structuring, featured by its rapid manufacturing capability, high process reliability, and design flexibility,[142] has been used recently to convert conventional flat and dense electrode coatings into patterned microstructures through a scanning laser beam.[139] For instance, Park et al. created inverted triangle-shaped microgrooves on the 210 μm thick $LiNi_{0.5}Mn_{0.3}Co_{0.2}O_2$ cathodes (Figure 14f), to facilitate the electrolyte infiltration and shorten the ion diffusion pathways.[139] It translated to the improved specific energy in thick electrodes at high charge/discharge rates, compared to the unstructured ones (Figure 14g). Note that laser structuring is mainly used for creating grooves on electrodes surface, whereas constructing 3-D hierarchical porous network is challenging. Besides, the heat accumulation and thermal damage on the active materials

during manufacturing require more attention, especially for thick electrodes with longer etching time.[142]

Phase inversion method is also an efficient strategy to obtain thick electrode with high-areal capacity in LIB.[143] During phase inversion, the instant solidification of components such as active materials, binders, conductive carbon black etc. enables the fabrication of ultrathick yet robust electrodes. **Figure 15**a showed the fabrication process of a bilayer $LiFePO_4$ (LFP) electrode using a templated phase inversion method.[143c] A mixed slurry was cast on a plate with a stainless-steel mesh under the surface of the casting film. Due to a small amount of water injected, the polymers and water began to diffuse toward each other until reaching equilibrium, leaving a trilayer LFP membrane (Figure 15b) or bilayer LFP membrane (Figure 15c) by lifting off the mesh. After polishing the surface of the bilayer LFP electrode, the membrane was revealed open and aligned microchannels with an average diameter of ≈100 µm (Figure 15d), which could provide direct and short ion transport pathways. Benefiting from the instant solidification of the components, three different mass loading electrodes of 45, 60, and 100 mg cm^{-2} were fabricated without mechanical deterioration, which exhibited a higher current density of 8.5 mA cm^{-2} (0.5 C) even at LFP mass loading up to 100 mg cm^{-2} (Figure 15e). Furthermore, the strategy of phase inversion to fabricate thick electrode with high mass loading also could be applied to SIB system.[143a] During the phase inversion process, as soon as the casted membrane was immersed into a nonsolvent, the solvent–nonsolvent exchange occurred until thermodynamic equilibrium. Based on nonsolvent-induced phase inversion method, a $Na_3V_2(PO_4)_3$ based cathode with ultrahigh mass loading up to 60 mg cm^{-2} and areal capacity up to 4.0 mAh cm^{-2} was fabricated. In summary, benefiting from the structural advantages from phase inversion method, the thickness of electrode could reach to 1.2 mm, and areal mass loading

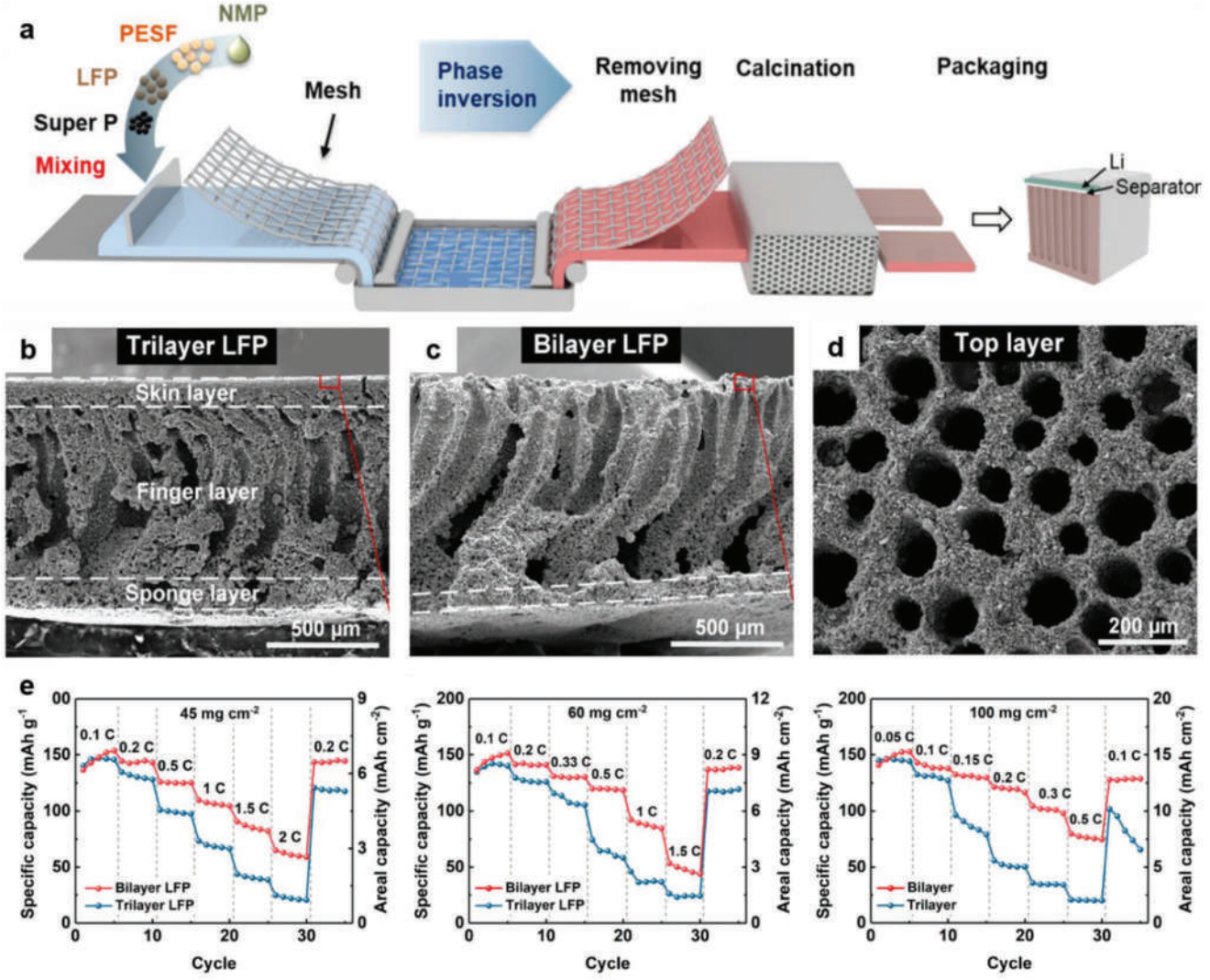

Figure 15. High-areal-mass loading electrode fabricated by phase inversion method. a) The fabrication process of multi-layer LFP electrodes using the phase inversion method. Cross-section SEM images of b) trilayer LFP and c) bilayer LFP electrodes. d) Top surface SEM image of multi-layer LFP electrode after polishing to reveal microchannels. e) Electrochemistry performance of multi-layer LFP thick electrodes with LFP areal mass loading up to 45, 60, and 100 mg cm^{-2}. Reproduced with permission.[143c] Copyright 2021, American Chemical Society.

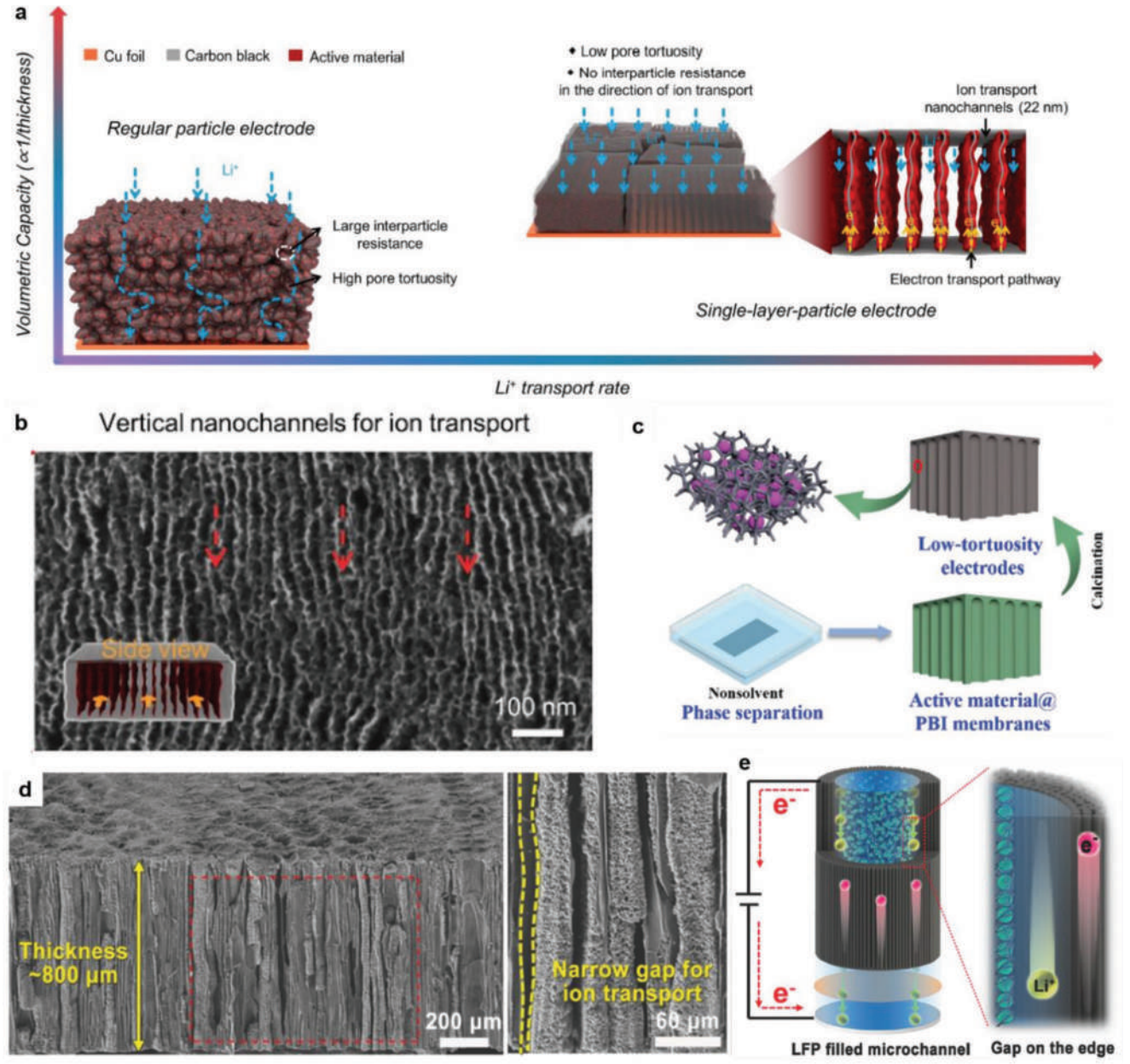

Figure 16. The effects of pore structures on electron/ion transport and electrolyte uptake in thick electrode. a) The comparison of Li^+ ion transport rate between high and low tortuosity electrodes. b) SEM image of vertical inner nanochannels with low tortuosity. Reproduced with permission.[144] Copyright 2022, John Wiley and Sons. c) Schematic illustration of several porous nanoclusters assembled into a vertical array with low tortuosity. Reproduced with permission.[143a] Copyright 2021, John Wiley and Sons. d) Hierarchical channel frameworks with low tortuosity and high porosity. e) The electrolyte-filled gaps at the edge of the channels. Reproduced with permission.[145] Copyright 2017, John Wiley and Sons.

was also up to 100 mg cm^{-2}. Using phase inversion method was a reliable strategy to prepare thick electrodes.

Efforts for thick electrodes manufacturing are becoming more systematic and comprehensive. Meanwhile, the researchers also pay attention to other accompanying problems: 1) the effects of pore structures (such as tortuosity and porosity) on charge transport in the thick films; 2) the electrolyte uptake in thick electrodes for long-life and high-areal-capacity LIBs; 3) stable solid-electrolyte interface for accommodating the volume expansion in the thick electrodes.

Figure 16 shows the effects of pore structures on electron/ion transport and electrolyte uptake in thick electrodes. Owing to high tortuosity and large packing thickness, typical particle electrodes consisting of nanoscale active materials with conducting species could shorten the charge transport distance and improve conductivity at the nanoparticle level (Figure 16a, left).[144] However, fast-charging capability at the electrode level is still significantly plagued due to the random stacking of nanoparticles and low packing density. Although high tortuosity and high porosity can improve the electrolyte uptake in

thick electrodes, the excessive contact of electrode-electrolyte also leads to a large number of solid-electrolyte interfaces, which reduces Coulombic efficiency.[61a] Therefore, considering the thickness, tortuosity and/or porosity, electrolyte uptake and Coulombic efficiency, as well as the volume change during charge/discharge processes, those problems are necessary to be addressed while designing a thick electrode. Tu et al. fabricated a single-layer chunky particle electrode with vertically aligned and low pore tortuosity architecture, which approved a high areal capacity of 5.6 mAh cm^{-2} (Figure 16a, right).[144] Vertical inner nanochannels with low tortuosity enabled fast ions and electrons transport in single-layer chunky particle electrode (Figure 16b).

Given the reasonable hierarchical channels design, it can also achieve a balance between low tortuosity, high porosity, and high electrolyte uptake in the thick electrode. The best approach to expedite the infiltration of electrolyte is to build high porosity structure. By self-assembling of several porous nanoclusters, such as vertically or parallelly aligned, a framework with low tortuosity can be obtained. According to the effective ionic conductivity D_{eff} expression ($D_{eff} = \frac{\varepsilon}{\tau} D$, where ε is the porosity, τ is the tortuosity, and D is the intrinsic ion conductivity),[61a] low tortuosity and high porosity are beneficial to improve ionic conductivity. Taking the porous carbon matrix embedded by active materials as subunit, a low-tortuosity, vertically aligned composite electrode with ultrahigh mass loading were reported, which could offer well-pleasing electron/ion transport pathway and relatively high electrolyte permeability (Figure 16c).[143a] Such a low-tortuosity, high-porosity hierarchical channel frameworks were also demonstrated by directly carbonized from natural wood as an ultrathick electrode (up to 800 µm) with active material mass loading up to 60 mg cm^{-2}, which delivered a rational capacity of 7.6 mAh cm^{-2} (Figure 16d).[145] Benefitting from the uniqueness of the multichanneled framework, the electrolyte-filled gaps at the edge of the channels with low tortuosity provided straight pathways for the fast transport of Li^+ ion (Figure 16e).

In practice, it is commonly essential to design special electrolytes for a specific pair of cathode and anode materials to meet the performance requirement of battery packs.[146] The electrolytes used to match the thick and porous electrodes have also been optimized, such as high concentration electrolyte,[147] electrolyte additives,[148] solid-state electrolytes[149] etc., to accommodate the volume change of thick electrode during operation. Alloys (e.g., Li_xSi, Li_yAl, Li_zBi) are among promising anode materials for LIB, yet they suffer from fast degradation due to large volume expansion. Chen et al. reported a strategy of electrolyte additive by developed that 2.0 M $LiPF_6$ in a 1:1 v/v mixture of tetrahydrofuran and 2-methyltetrahydrofuran electrolyte, which facilitated the formation of thin and uniform LiF-based solid-electrolyte interfaces (SEIs) with a low adhesion to anode surfaces (**Figure 17**a).[148] In addition, concentration electrolytes were also developed for Si-based anodes. Jia et al. designed localized high-concentration electrolytes with only 1.2 wt% fluoroethylene carbonate (FEC), which achieved minimum volume change (45.8%) on the electrode swelling at 100% state-of-charge and end-of-life, compared to pristine electrode (82.7%) and conventional-10 wt% FEC additive (67.6%) (Figure 17c–e).[147] The volume change of electrode during repeated cycles could also be effectively suppressed. Xiao et al. attained inorganic solid-state LIB using a "melt-infiltration" solid-state electrolytes technology, by which dense-calendered electrodes could be produced and wound in the whole thick and porous electrodes (Figure 17b). The method enabled to obtain both high volumetric energy density and excellent interface compatibility to relieving volume expansion.[149]

7. High-Areal-Capacity SIB Electrodes

Compared to LIB, relatively less high-areal-performance SIB electrodes are reported (**Table 8**), due to their different development stages. Basically, most of them show designs of hybridizing active materials like oxides or sulfides with 3-D metal or carbon substrates based on either in-situ growth or percolating network, which are similar to those for LIBs as demonstrated in the above sections. Nevertheless, due to the greater challenges caused by larger ionic radius of Na^+ than Li^+, the SIB electrodes also show differences from those for lithium storage; these special aspects are reflected both on the electrode structures and the selection of active materials and will be discussed in detail below.

Regarding the electrode structures, the SIB electrodes rely more on the introduction of 3-D porous conductive network, while bare nanostructures-based slurry coatings are relatively less reported. It is because the relatively more sluggish electrochemical behaviors in SIB electrodes require a more reliable electron and ion transport for thick electrode designs, compared with those for LIB electrodes.[175] Such designs can be mainly classified into two types in terms of the specific structures.

The first type is incorporated with a percolating conductive network by physical processes, such as MoS_2 nanosheets/CNT hybrid network[161] and few-layer bismuthene/graphene composite films.[166] Given the different transfer paths of electrons and ions within the electrode, the percolating conductive network performs electron transfer path, while the ion transfer path is based on the aligned low-tortuosity architecture filled by electrolyte.[61a] By physical mixing as-exfoliated MoS_2 nanosheets with 20 wt% single-wall carbon nanotubes, Liu et al. constructed a MoS_2/CNT hybrid network with high porosity and extremely conductive,[176] which could perform high both electron and ion transfer pathways. Followed by vacuum filtration, a dense packing process, they obtained a flexible free-standing MoS_2/CNT membrane with tunable thickness up to 90 µm (**Figure 18**a), which achieved striking volumetric capacity (≈650 mAh cm^{-3}) and areal capacity (>6.0 mAh cm^{-2}) (Figure 18b) as the working electrode of SIBs directly with an extremely high loading up to 15 mg cm^{-2}. By readily adjusting the content of advanced 2-D materials with lower electrical percolation threshold such as graphene, it is a relatively important strategy to fabricate high-mass-loading electrode with superior conductivity.[61a] Zhou et al. designed 2-D structure of few-layer bismuthene specifically with a large aspect ratio (Figure 18c), which could relieve the expansion strain along the z-axis.[177] Then, by vacuum filtration, a few-layer bismuthene/graphene films with tunable thickness were fabricated (Figure 18d). The composite electrodes displayed excellent stability as well as the

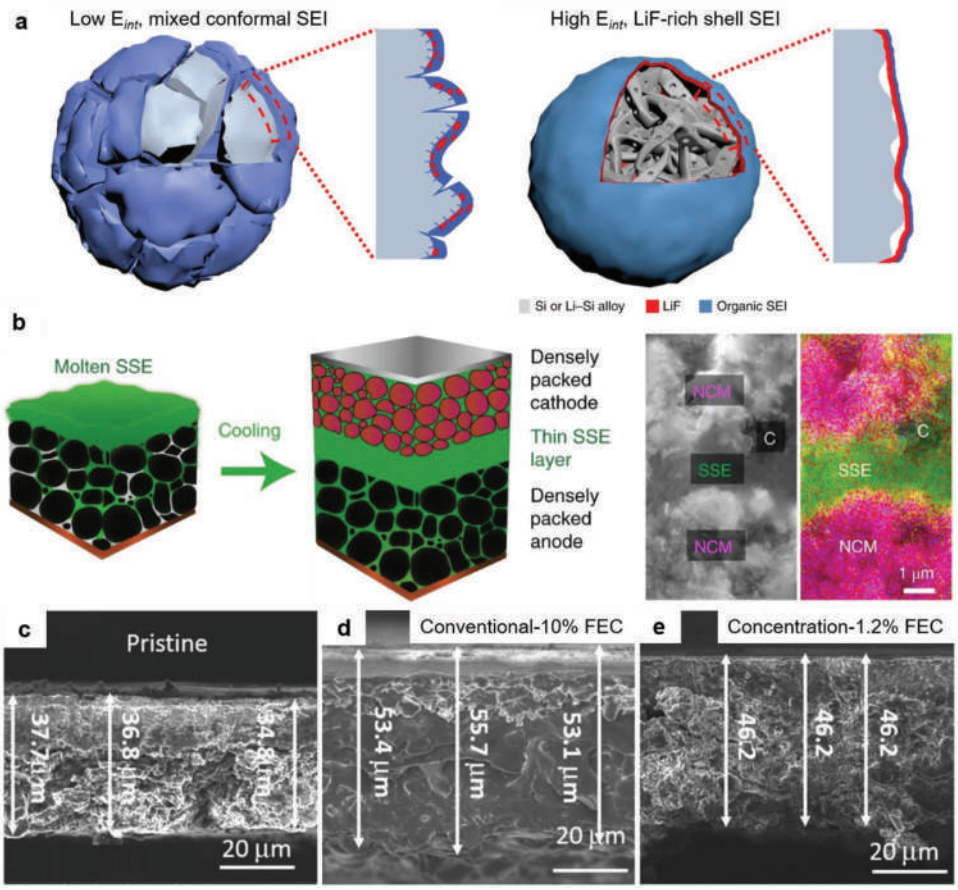

Figure 17. Electrolytes optimization for accommodating the volume expansion in thick electrodes. a) Compared between organic, low interfacial energy (E_{int}) and nonuniform (left) and inorganic, high E_{int} and uniform SEI interface (right). Reproduced with permission.[148] Copyright 2020, Springer Nature. b) "Melt infiltration" of solid-state electrolyte in thick and porous electrode. Reproduced with permission.[149] Copyright 2021, Springer Nature. c) The effects of localized high-concentration electrolytes on the electrode swelling. Reproduced with permission.[147] Copyright 2019, John Wiley and Sons.

capacities of electrodes were linear scales with the areal loading, reaching an exceptional value of 12.1 mAh cm^{-2} (Figure 18e).

The second type is nanostructures in situ grown on 3-D porous conductive substrate, in which the multilayer hybrids like a ternary sandwich structure are more frequently applied. It is mainly because the larger volume variation during sodiation and de-sodiation requires higher buffering capability provided by hierarchical structures, to enhance the structural stability and prevent electrode pulverization and degradation.[72] For example, Chen et al. constructed a hierarchical carbon fiber/Fe_7S_8/graphene network structure for sodium storage by two-step coating followed by an annealing process (**Figure 19**a).[22] Based on the free-standing cotton fibers with negatively charged oxygen-containing groups, surface-aminated positively charged FeS_2 were first coated via an electrostatic interaction, and then graphene oxide film covered the hybrid fibers. After the annealing process to realize the carbonization of cotton fiber (Figure 19b) and reduction of graphene oxide, the Fe_7S_8 microparticles decorated 3-D carbon framework embedded in graphene films were obtained (Figure 19c–e). Attributed to the synergistic effect of improved charge transport kinetics and structural stability enabled by the hierarchical structures, the hybrid electrodes achieved high areal capacities of 2.12 mAh cm^{-2} at 0.25 mA cm^{-2} at mass loadings of 3 mg Fe_7S_8 cm^{-2}.

Regarding the materials selection for high-mass-loading SIB electrodes, suitable channels for efficient sodium diffusion are highly required. It is generally achieved by two types of materials. The first is layered transition metal dichalcogenides like MoS_2,[161] $MoSe_2$,[153] SnS_2,[155] etc. or metal oxides compounds like Nb_2O_5,[152] $Na_{0.67}CoO_2$[151] and CaV_4O_9,[174] which prompts the sodium diffusion by their relatively large interlayer spacings. The second is NASICON-type materials such as anodic $NaTi_2(PO_4)_3$ and cathodic $Na_3V_2(PO_4)_3$.[163–165] The pre-existing 3-D tunnels in their stable crystal structures enable zero-strain Na^+ (de)intercalation.[163] In addition, due to the intrinsically high electron conductivity and plentiful sodium storage sites, hard carbon materials[169–171] and conductive metal organic framework (MOF)[173] have also attracted researchers' attention. Park et al. developed a novel cobalt-based 2D conductive MOF with stable and plentiful dense active sites for sodium storage.[173] Coordinated with cobalt (II) ion nodes, redox-active hexaaminobenzene (HAB) linker in the Co-HAB material stably underwent three-electron reversible reaction for sodium storage (Figure 19f). Attributed to the high electron conductivity (1.57 S cm^{-1}) and dense redox active sites and subnanometer

Table 8. The literature survey on the high-areal-performance SIB electrodes.

Type	Electrode structure	I [mA g^{-1}, mA cm^{-2}]	Cycles	M_a [mg cm^{-2}]	C_a [mAh cm^{-2}]	Refs.
In situ grown on 3-D conductive substrates	Ni_3Se_2 nanorod array on Ni foam	0.2	100	4 (Ni_2Se_2)	1.55	[150]
	$Na_{0.67}CoO_2$ bundle arrays on Ni foam	189	100	10 ($Na_{0.67}CoO_2$)	1.24	[151]
	CNT@Nb_2O_5@C sponge	100	200	16.6	2.7	[152]
	CNT@$MoSe_2$@C sponge	100	50	13.9	4	[153]
	CNT/$CoSe_2$/C sponge	0.2	100	4	1.55	[154]
	CNT/SnS_2@C sponge	100	200	6.5	3.93	[155]
	$Li_4Ti_5O_{12}$ nanosheets on carbon cloth	200	300	≈1.7 ($Li_4Ti_5O_{12}$)	0.27	[156]
	$Ni_3V_2O_8$ nanosheets on carbon cloth	500	1000	4	0.54	[157]
	Fe_7S_8 microparticles embedded in graphene film welded on carbonized cotton cloth	6 0.25	5000 1	3 (Fe_7S_8) 3 (Fe_7S_8)	0.75 2.12	[22]
	Vertically aligned 2-D self-branched (big nanoflake core and small nanosheet branches) SnS_2 nanoarrays on a graphene foam	200	200	3.98	3.3	[158]
	Sn nanodots on nitrogen-doped carbon sheets	100	100	20	1.5	[159]
Percolating network	Carbon-reinforced Nb_2CT_x MXene/MoS_2 nanosheet/flower	1000	2000	≈1.3	≈0.5	[160]
	Network of exfoliated MoS_2 nanosheets reinforced with single-wall CNT	0.2	100	15	3.7	[161]
	Amorphous MoS_3/CNT	100	100	12.1	5.3	[162]
	$NaTi_2(PO_4)_3$ supported on carbon nanotube fabrics	≈135	700	8.02	1.01	[163]
	$Na_3V_2(PO_4)_3$ supported on carbon nanotube fabrics	≈130	700	7.63	0.79	[163]
	$Na_3V_2(PO_4)_3$@C anchored on the surface of carbon fibers and embedded in carbon framework between carbon fibers	≈135	100	3.5 ($Na_3V_2(PO_4)_3$@C)	0.39	[164]
	$Na_3V_2(PO_4)_3$–carbon nanofibers composites	≈270	200	8.5 ($Na_3V_2(PO_4)_3$)	0.78	[165]
	Few-layer bismuthene/graphene composite film	–	50	42.1	12.5	[166]
	$Fe_{1-x}S$@porous carbon nanowires/rGO film	100	100	11.2	1	[167]
Carbon and conductive MOF	Nb_2O_5 grafted in carbon nanoreactor	1000	1000	≈8	≈2	[168]
	Network carbon with macropores	–	200	5.1	1.91	[169]
	Carbonized wood	0.1	100	5	1.25	[170]
	Poplar wood-derived hard carbon	660	630	7	2[a)]	[171]
	MOF-derived Fe_7S_8 nanoparticles/N-doped carbon nanofibers	1000	2000	≈0.7	≈0.35	[172]
	Cobalt-based 2-D conductive metal-organic framework	50	–	9.6	2.6	[173]
Other	CaV_4O_9 nanosheet microflowers	100	100	3.65	0.82	[174]

pores (Figure 19g), the Co-HAB electrode exhibited a pseudocapacitive charge storage mechanism and a well-maintained electrochemical kinetics even at an areal mass loading up to 9.6 mg cm^{-2}, resulting in a high areal sodium storage capacity of 2.6 mAh cm^{-2} (Figure 19h).

Taking both electrode structure and active materials selection into account, our group recently reported CNT@T-Nb_2O_5@C sponge electrodes[152] for stable and high-areal-capacity sodium storage (**Figure 20**). The 3-D porous network (Figure 20a) in the hybrid sponges consisted of interconnected CNT skeletons coated successively by uniform and conformal T-Nb_2O_5 and carbon layers to form the nanocable structure (Figure 20b). The sandwiched T-Nb_2O_5 served as active materials to store sodium ions; CNT substrate and outer carbon shell provided well-defined electron and lithium transport pathways at both meso- and nanoscale, and contributed to higher structural stability (Figure 20c). Different from previous research mainly focusing on thicker electrodes for high electrode loadings, we proposed raising the content of active materials in the hybrid structure to achieve the same goal. Specifically, with the Nb_2O_5 coatings thickening from 7.1 to 21.2 nm (Figure 20d), the areal mass loading of the sponge electrodes increased from 7.2 to 16.6 mg cm^{-2} with their macroelectrode height kept constant. And owing to the rationally designed hierarchical structure, the charge transport kinetics and structural stability were well-maintained in the hybrid electrodes, which enabled steady cycling for 200 cycles and high areal capacities of 2.7 mAh cm^{-2} at mass loadings up to 16.6 mg cm^{-2} (Figure 20e). The post-mortem analysis (Figure 20f–h) indicated that the outer carbon shell coating played a significant role in protecting the 3-D nanocable structure from damage and thereby contributed to higher structural and electrochemical stability. As shown, the CNT@T-Nb_2O_5 sponges network (Figure 20f) turned into a chaotic mixture of partly uncovered CNTs and detached or

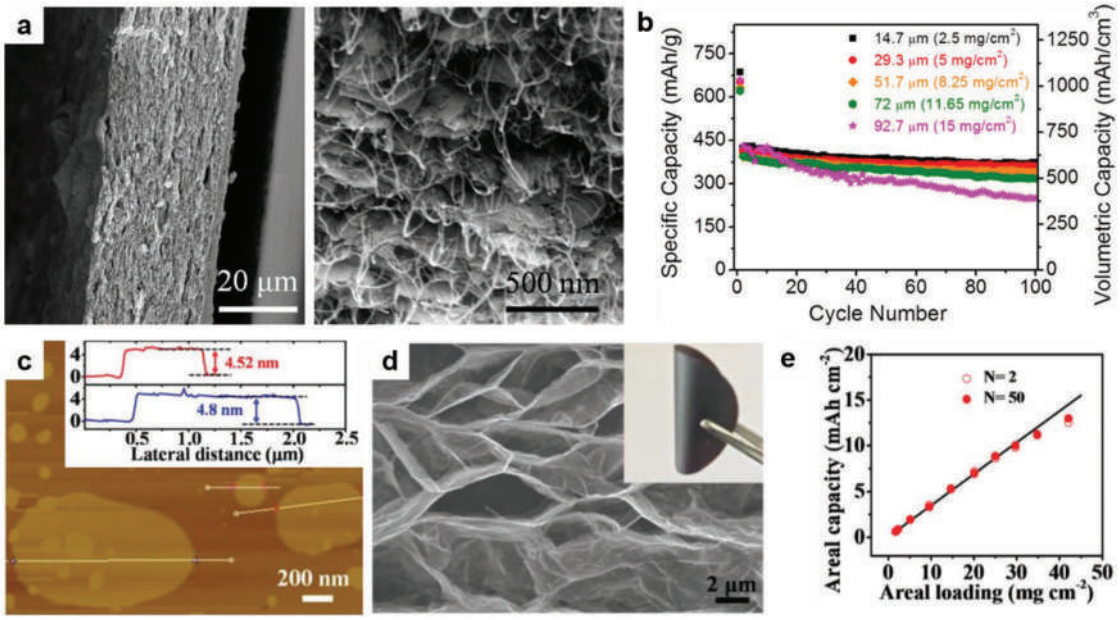

Figure 18. Electrode designs by physical processes using a percolating conductive network for high-areal-capacity sodium storage. a) Cross-section SEM images of freestanding MoS_2/CNT membrane. b) Electrochemistry performance of MoS_2/CNT membranes with different thicknesses/mass loading. Reproduced with permission.[176] Copyright 2016, American Chemical Society. c) The height of 2-D bismuthene sheets. d) Cross-section SEM image and a digital photograph of bismuthene/graphene films. e) Areal capacity measured at the 2nd cycle and 50th cycle plotted versus areal mass loading using bismuthene/graphene films as working electrode directly. Reproduced with permission.[177] Copyright 2019, John Wiley and Sons.

aggregated Nb_2O_5 clusters leading to loss of active materials; in contrast, the CNT@T-Nb_2O_5@C sponge with outer carbon coatings preserved its clean porous network (Figure 20g) and hybrid nanocable structure Figure 20h), which kept providing stable active sites for sodium reaction and resulted in better cycling stability of the hybrid electrodes. The work showed that sandwiching active materials between 3-D porous conductive underlayers and outer protective coatings represented an effective strategy to achieving high-areal-capacity electrodes cycling stably at elevated mass loadings.

As an essential component of SIB, cathode electrode designs also have an effect on the electrochemical performance. Inspired by the technologies of preparing high-areal capacity in LIB, efforts to optimize the architecture of cathodes by radially aligned dense columnar structure and the hierarchical porous 3D network had been reported.[178] Compared to the conventional bulk single particle cathode with disordered accumulation (**Figure 21**a), Hwang et al.[179] designed a unique radially aligned dense and hierarchical columnar structure in spherical particles with varied chemical compositions from the inner end ($Na[Ni_{0.75}Co_{0.02}Mn_{0.23}]O_2$) to the outer end ($Na[Ni_{0.58}Co_{0.06}Mn_{0.36}]O_2$) (Figure 21b), which accentuated the volumetric energy density of ≈1177 Wh L^{-1} at a high tap density of ≈2.5 g cm^{-3} due to the presence of fewer voids in the columnar structure.

In order to explore the intrinsic electrochemical performance of metal vanadium phosphates such as $Na_3V_2(PO_4)_3$ (NVP), researchers developed various hierarchical porous 3-D networks (e.g., micro/mesoporous 3D foam,[180] honeycomb-structured hierarchical composite microspheres[181] as well as encapsulating organic carbonyl compounds in an ordered porous network[182]) in which the surfaces and/or channels of the individual framework were grafted with NVP nanoparticles, achieving satisfactory performance parameters. Zhou et al. prepared nanostructured NVP 3-D foam via assembly of recombinant elastin-like polypeptides which obtained fibrous and micro/mesoporous composite cathode (Figure 21c).[180] Following this viewpoint, Wang et al. reported an architecture named "honeycomb-type porous microspheres," which was composed of hierarchical pores and numerous interconnective nanochannels, filled with NVP nanoparticles (Figure 21d).[181] In addition, hard templates with aligned channels such as CMK-3 were encapsulated in organic carbonyl compounds to develop highly dense nanoparticles (Figure 21e).[182]

8. The Cell-Level Energy Density Base on High-Areal-Capacity Thick Electrodes

In a battery system, increasing electrode thickness (e.g., high-areal capacity) means changing the proportion of battery components and thus increasing the volume ratio of active materials, which is one of the effective methods to develop high energy density LIB and also can reduce the manufacturing cost.[183] However, the excess electrode thickness also increases cell polarization and underutilization of active materials.[184] Nowadays, there are three different types of cell formats such as pouch cell, cylindrical cell, and prismatic cell, as shown in **Figure 22**a.[185] Take the most common pouch cell as an example. Figure 22b exhibited the proportion of each component of a pouch cell with 50 wt% positive materials and 19 wt% negative materials, reaching a high energy density of 297 Wh kg^{-1}.[186] Besides, with the thickness of electrode increased from 50 to 100 μm, the total cell cost reduces notably as high as ≈30%.[9] Yang et al.

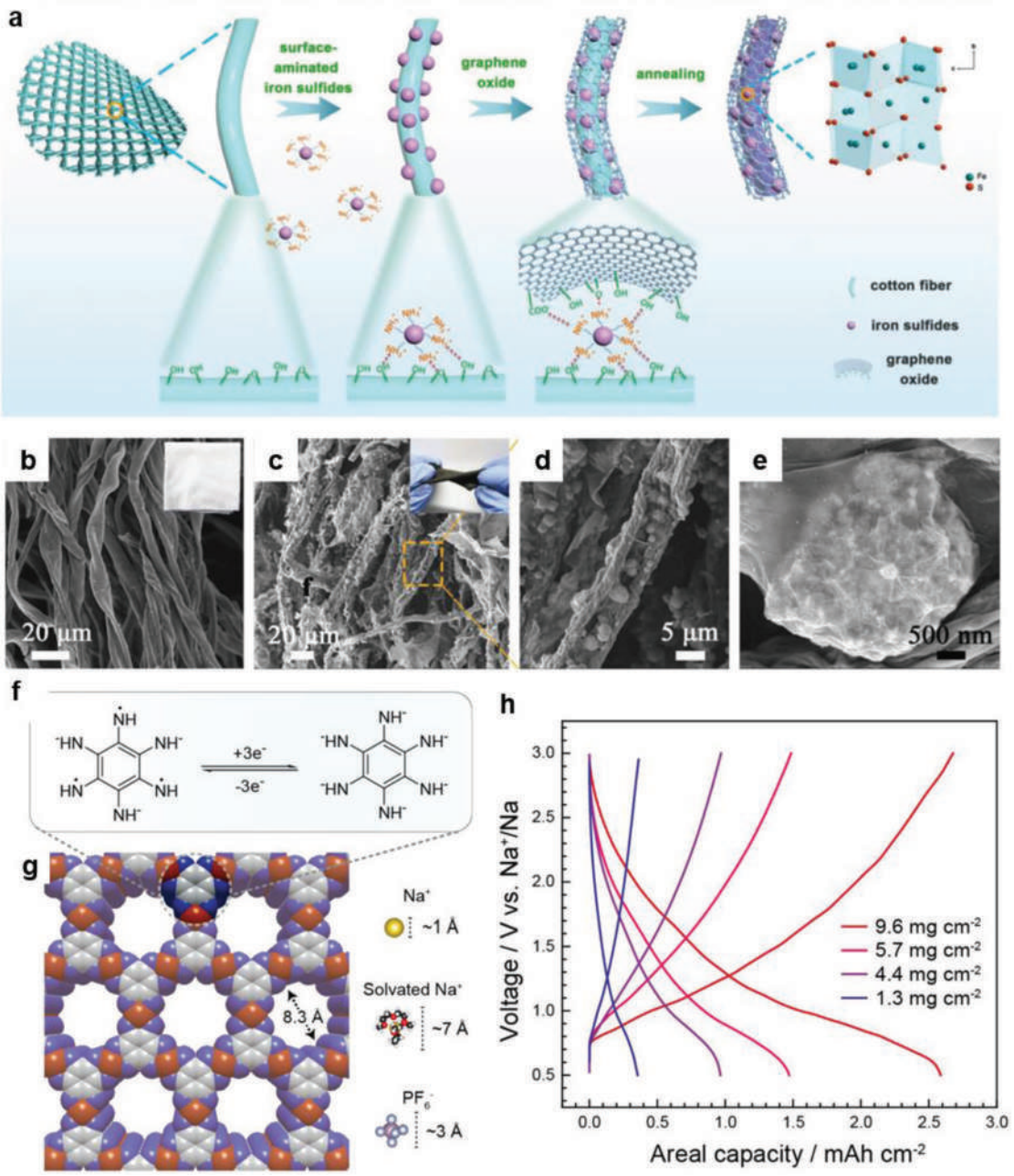

Figure 19. Electrode designs by in situ grown on 3-D porous conductive substrate for high-areal-capacity sodium storage. a) Schematic of the fabrication of carbon/Fe_7S_8/graphene hybrid network. b) SEM image of the carbonized cotton fibers. Inset shows the photo of pristine cotton cloth. c–e) SEM images of the carbon/Fe_7S_8/graphene hybrid structure at different magnifications. Inset in (c) shows the photo of the twisted hybrid electrode. Reproduced with permission.[22] Copyright 2019, John Wiley and Sons. f) Proposed three-electron reaction in Co-HAB. g) Structural model of Co-HAB calculated by density functional theory, with pore sizes compared to those of ions in SIB electrolyte. h) Voltage profiles of the Co-HAB electrodes at different areal mass loadings. Reproduced with permission.[173] Copyright 2018, American Chemical Society.

illustrated the energy density and cell components ratios simulation shown as Figure 22c.[187] When the cathode materials mass loading increased from 5 mg cm^{-2} up to 20 mg cm^{-2} (close to the value in the state-of-the-art liquid-electrolyte-based LIB), the ratio of the cathode materials reached 56 wt%. Under these conditions, a high energy density of 378 Wh kg^{-1} was expected to be obtained, which could meet the energy density requirement of long-range electric vehicles. Over the last decades, the gradual improvement in energy density was mostly due to cell components optimization, such as making current collectors and separators thinner, double-coating electrode (Figure 22d), and continuously increasing the active materials ratio.[188] However, it was worth noting that the average discharge voltage gradually decreased due to the polarization with the increase of cathode thickness, resulting in a maximum point of the volumetric energy density (Figure 22e).[26b] And

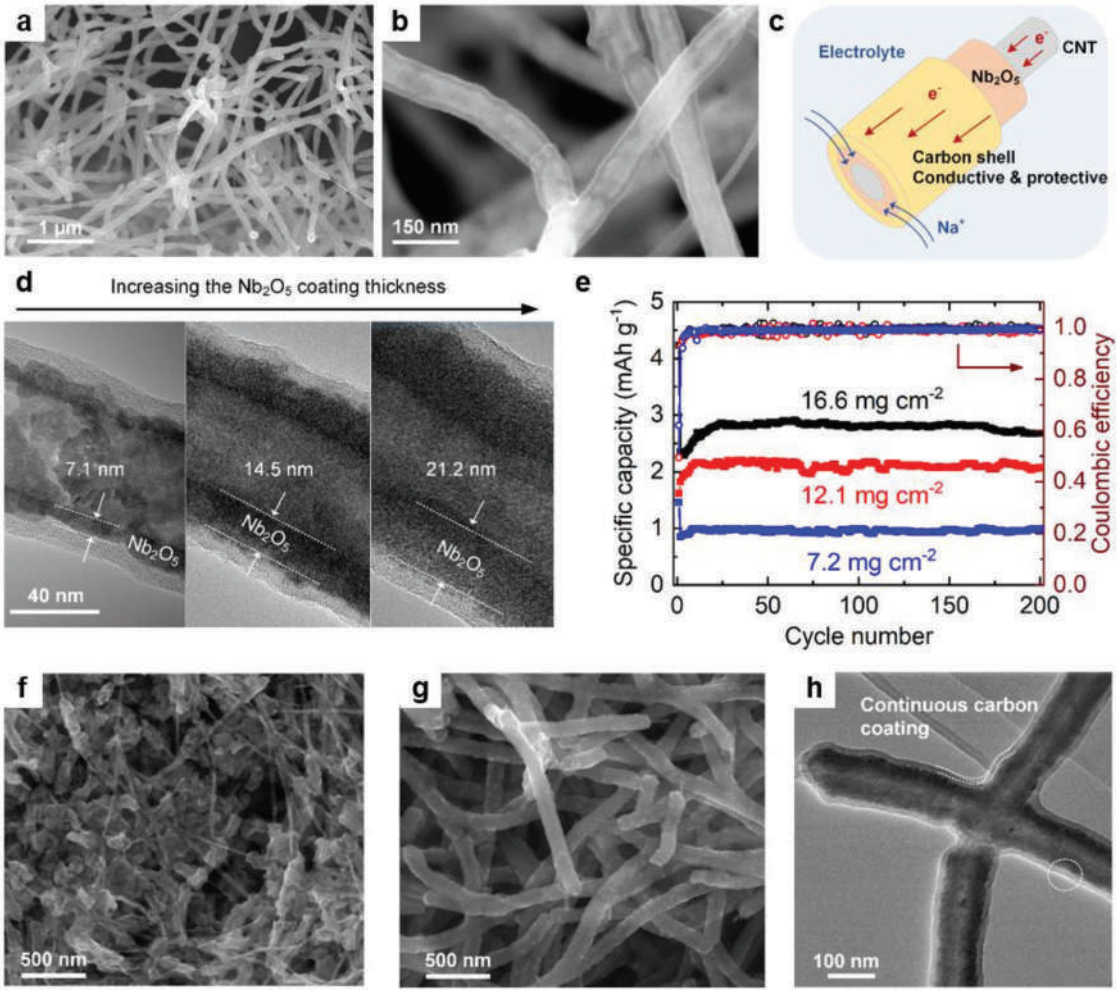

Figure 20. CNT@T-Nb_2O_5@C nanocable with thick active intermediate layer for stable and high-areal-capacity sodium storage. a) SEM image of the 3-D porous network in the CNT@T-Nb_2O_5@C sponge. b) Enlarged SEM image showing the uniform and conform coatings of Nb_2O_5 and carbon on the interconnected CNT skeletons. c) Schematic illustration of the charge transport in the nanocable structures. d) TEM images of the CNT@T-Nb_2O_5@C nanocable with increasing thicknesses of the Nb_2O_5 intermediate layers for higher electrode mass loadings. e) Areal capacities of the CNT@T-Nb_2O_5@C electrodes with elevated areal mass loadings corresponding to the hybrid structures with three increasing thicknesses of the Nb_2O_5 coatings shown in (d). f) SEM image of the CNT@T-Nb_2O_5 electrode after 200 charge/discharge cycles. g) SEM and h) TEM images of the CNT@T-Nb_2O_5@C electrode after 200 charge/discharge cycles. Reproduced with permission.[152] Copyright 2020, John Wiley and Sons.

the solid phase Li^+ ion concentration (the infiltration of electrolyte) was inversely proportional to the thickness of electrodes (Figure 22f). Therefore, it needed to pay attention to the critical value of electrode thickness.

Based on the electrodes with different thicknesses, the projection of cell-level energy density is attractive and essential. Take a pouch cell assembled by Du et al.[26b] for example. The pouch cell design parameters were shown as **Table 9** used by nominal capacity close to 52 Ah. Here, $LiNi_{0.8}Co_{0.15}Al_{0.05}O_2$ (NCA)/graphite was chosen as the cathode and anode active materials, respectively. The cell dimensions were 26.5 × 22.5 cm, and the electrode dimensions were 24 × 21 cm. Owing to the close nominal capacity of the pouch cells, increasing the thickness of the cathode meant to decrease the layers number of double-coated cathodes significantly. For example, as listed in Table 9, instead of 21 layers of 60-μm-thick NCA electrode, there were only 8 layers of 150-μm-thick NCA electrode. Therefore, the corresponding other materials such as current collectors and separators were also reduced, in other words, reducing the manufacturing cost of the pouch cell. **Figure 23**a shows the relations between cathode thickness and areal capacity, layers of cathode, pouch cell volume, and energy density based on pouch-cell parameters in Table 9. Clearly, with the increase of cathode thickness, the areal capacity increased linearly, on the contrary, the layers number of cathode gradually decreased. It was worth noting that both values of pouch cell volume and energy density were slowly leveling off corresponding 150–200 μm thick cathode and about 6.2–8.7 mAh cm^{-2}-areal capacity, suggesting that the volume was approaching limit, as well as the volumetric energy density was also up to the highest value. The energy-power Ragone plots of 52 Ah pouch cells were shown in Figure 23b. Simply increasing the cathode thickness was not conducive to achieving high power density. The energy-power values of pouch cells were constrained by the curves due

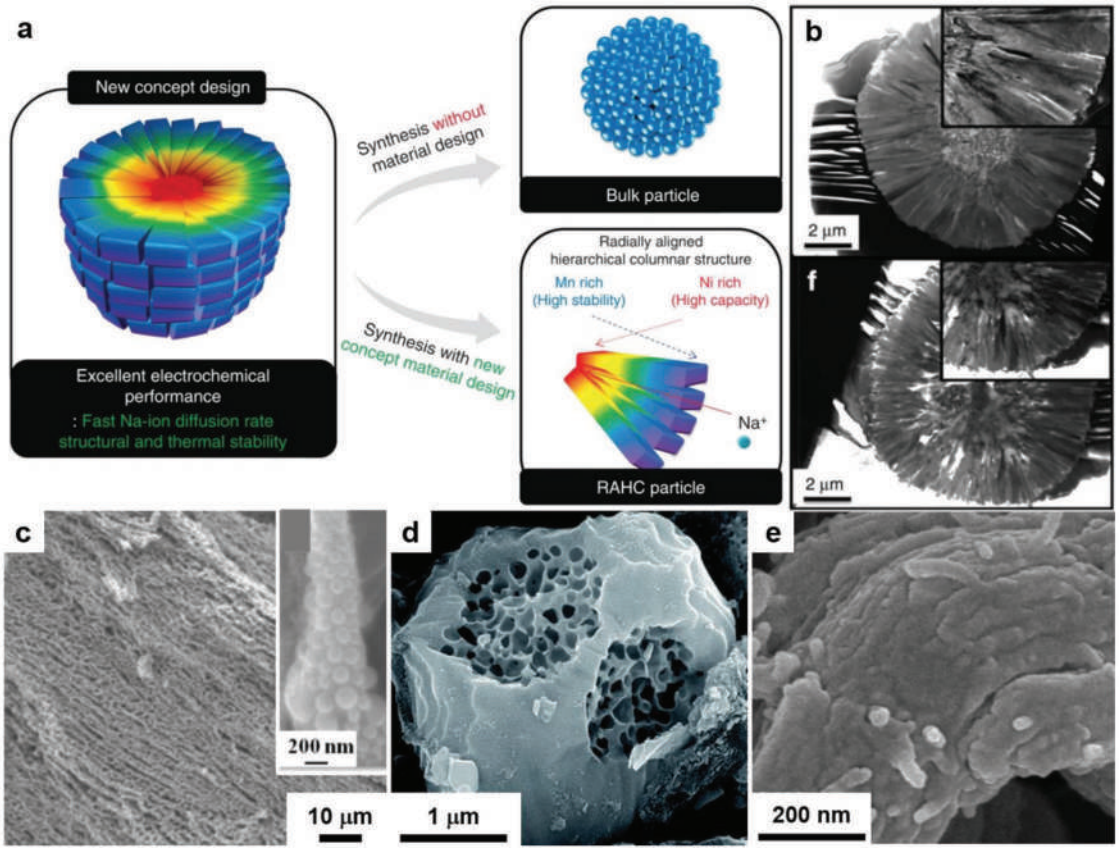

Figure 21. Cathode structure designs by dense columnar assemble and composite with 3-D hierarchical porous network. a) Comparison of bulk nanoparticles and radially aligned dense columnar structure. b) SEM images of radially aligned dense columnar structure. Reproduced with permission.[179] Copyright 2015, Springer Nature. c) SEM images of NVP 3-D foam with fibrous and micro/mesoporous. Reproduced with permission.[180] Copyright 2015, American Chemical Society. d) SEM image of honeycomb-type porous NVP/C microspheres. Reproduced with permission.[181] Copyright 2015, Royal Society of Chemistry. e) SEM image of hard templates such as CMK-3 with aligned channels encapsulating organic carbonyl compounds. Reproduced with permission.[182] Copyright 2015, Royal Society of Chemistry.

to the sluggish charge transfer and underutilization of active materials near the current collectors. Although the pouch cell assembled by 240 μm thick cathode exhibited highest energy density than others, the improvement was not significant, as shown in Figure 23b, because the power density decayed rapidly due to the electrolyte depletion probably. Cathodes with a thickness range from 120 to 180 μm appeared to have the best power density performance for the charge transfer capability.

Capacity matching is also essential during cell assembly, which represents that the areal capacities of cathodes and anodes should be close to each other due to their face-to-face configuration. Thus, achieving high areal capacity is important for both electrodes to obtain high volumetric energy density. Compared to anode, LIB cathode materials usually perform lower specific capacity, meaning that the electrodes of cathode are thicker than those of anode. LIB anode materials usually have simpler chemical compositions and can be synthesized by solvothermal methods, which enables easier in-situ growth of nanostructures on a bulk porous substrate. On the contrary, conventional LIB cathode materials like $LiCoO_2$ and NMC are generally fabricated by solid-state reaction at high temperature in air, hindering the incorporation of carbon or metal substrates. Furthermore, most of the composite cathodes are obtained by physically mixing active materials with conductive agents via slurry interpenetration or vacuum infiltration methods. As a result, bottom-up and facile wet chemistry-based synthetic approaches to those cathode materials require more exploration to achieve desired in situ hybridized structures. Currently, the other strategy to achieve high-areal capacity of cathode is to synthesize mixed-sized topological particles which could perform a higher tap density duo to the dense packing structure. On the other side, metal fluorides have attracted increasing attention recently as promising next-generation cathodes due to their high theoretical capacities and electrode potential.[189] Additionally, attributed to their relatively simple composition, in-situ deposition of metal fluorides on 3-D porous substrate could be a promising approach to developing high-tap-density LIB cathodes.

3-D porous current substrate is a promising route used to manufacture high-areal-capacity thick electrodes. However, the strategy is still fundamental research in Lab. Additionally, cost estimates of cell packs fabricated by this technique have rarely been reported. Take the SIB anode materials for example. Nowadays, SIBs are also commercially available, and the anode materials used in them are coal coke (a 3-D porous carbon matrix), which show lower cost. In

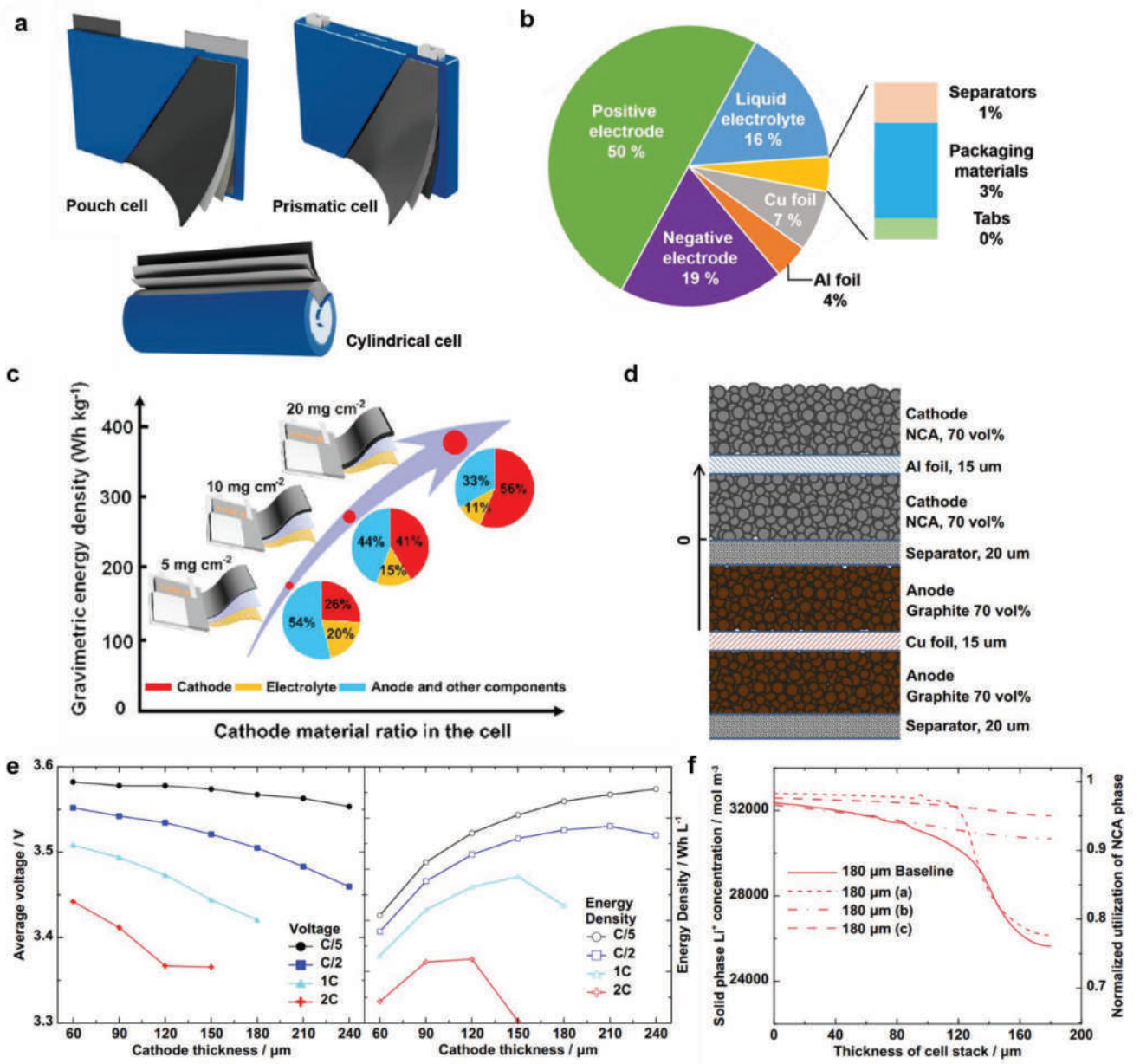

Figure 22. The performance of thick electrodes in pouch cell level. a) Three different types of cell formats. Reproduced with permission.[185] Copyright 2022, John Wiley and Sons. b) The proportion of each component of a pouch cell. Reproduced with permission.[186] Copyright 2019, Elsevier. c) Evolution of energy density with cathode component ratio from low to high. Reproduced with permission.[187] Copyright 2022, Elsevier. d) The illustration of double coating electrodes in the practice process. e) Average discharge voltages and volumetric energy density as a function of cathode thickness under different rates. f) Solid phase Li^+ ion concentration gradually decreased with the increase of electrode thickness. Approach (a) corresponded to decreasing NCA particle size to 500 nm; Approach (b) corresponded to increasing electrolyte molarity to 1.5 mol L^{-1}; Approach (c) corresponded to decreasing NCA particle size to 500 nm and increasing electrolyte molarity to 1.5 mol L^{-1}. Reproduced with permission.[26b] Copyright 2017, Springer Nature.

this "rocking chair batteries" system, those 3-D porous carbon anodes are used to storage Li/Na ion rather than as a 3-D current collector.[190] Therefore, how to introduce active materials with a high specific capacity (Si, Sn, P, etc.) to a cheap 3-D porous carbon matrix is the real technical problem. We appeal to that in situ deposition of high-specific-capacity active materials on 3-D porous carbon matrix could be a promising approach to developing high-areal-capacity LIB.

9. Conclusions and Outlook

Raising areal mass loadings of electrodes can significantly improve the cell-level energy densities and reduce the fabrication cost. However, most of previously reported high-performance electrodes show relatively low mass loadings of <1 mg cm^{-2} and thus limited areal capacities of <1 mAh cm^{-2}. The main obstacle is the degradation of the mechanical and electrochemical properties of thick electrodes

Table 9. Pouch cell design parameters used by nominal capacity close to 52 Ah. Reproduced with permission.[26b] Copyright 2017, Springer Nature.

NCA electrode thickness [μm]	Areal capacity [mAh cm^{-2}]	Layers of cathode	Pouch cell volume [cm^3]	Volume fraction of cell stack	Cell capacity [Ah]	Energy density [Wh L^{-1}]
60	2.50	21	393.6	0.81	52.8	480.94
90	3.75	14	362.7	0.80	52.9	521.87
120	5.00	10	331.6	0.80	50.3	542.92
150	6.23	8	322.8	0.80	50.3	556.71
180	7.50	7	331.8	0.80	52.9	568.78
210	8.72	6	327.4	0.80	52.7	573.96
240	9.96	5	309.5	0.80	50.2	576.56

during fabrication and battery operation. To cope with the challenges, various electrode materials and structures have been proposed, including nano-subunits-assembled high-tap-density microclusters as active materials, novel binder systems, layered electrode configuration, vertically aligned structures, and incorporation of 3-D porous conductive matrix. Advanced manufacturing techniques such as 3-D printing and laser structuring have also played roles in engineering porous structures or enhancing mechanical integrity in thick electrodes to improve their performance. Both LIBs and SIBs electrodes are discussed.

As demonstrated in this review, the work orienting to high areal capacity shows some special characteristics compared with previous thin-film electrodes mainly focusing on gravimetric capacity improvement. On one hand, some commonly adopted strategies for thin-film electrodes may be no longer suitable at elevated mass loadings. For example, simply morphology engineering on single-phase nanomaterials becomes less effective, and plenty of high-areal-capacity designs involve porous conductive network hybridized with active materials to achieve well-defined charge transport pathways through the whole electrodes at high mass loadings. 2-D nanosheets like graphene have been extensively studied in thin-film electrodes due to their large surface area, nevertheless are relatively less adopted as substrates in thick electrodes compared to 1-D carbon nanotubes or fibers, as they tend to form stacks with decreased porosity and affect ion diffusion. The problem can be alleviated by the creation of in-plane holes or morphology transformation from nanosheets to nanoribbons in the graphene-based structures. On the other hand, new structure designs have been proposed to promote the areal performance. For example, high-tap-density active materials usually exhibit relatively lower gravimetric capacity and are thus rarely reported in thin-film electrodes, but is an effective strategy to improve mass loadings and achieve high areal capacities. With regard to the electrode fabrication approaches, techniques like physical vapor deposition or atomic layer deposition are generally used for thin film fabrication and are seldom reported to make thick electrodes. Instead, novel manufacturing methods like powder extrusion molding, phase inversion method and spark plasma sintering are investigated more in the areal-capacity-related studies.

Although various strategies have been proposed to enhance the areal lithium/sodium storage performance of electrodes, some details require more attention in these designs, in order to mitigate possible problems in the practical operation of batteries. And resolving these issues represents potential research directions associated with high-areal-mass-loading electrodes in the future.

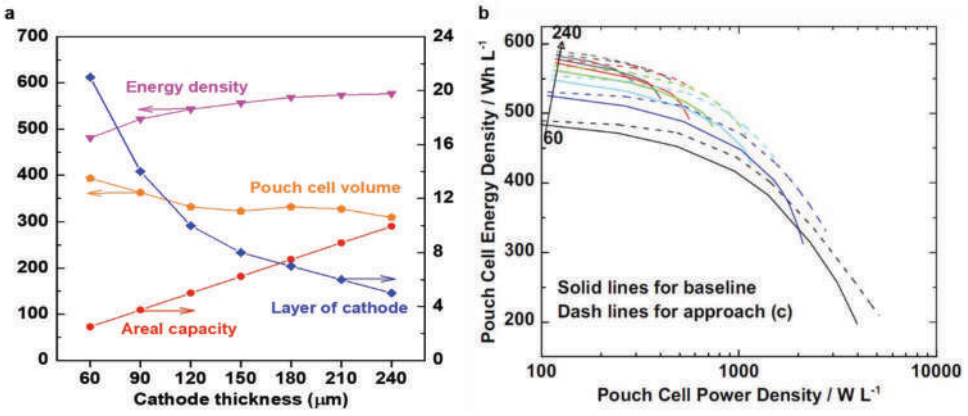

Figure 23. The performance of pouch cell assembled by differently thick cathodes. a) The relations between cathode thickness and areal capacity, layers of cathode, pouch cell volume, and energy density. b) The energy-power Ragone plots of 52 Ah pouch cells. Approach (c) corresponded to decreasing NCA particle size to 500 nm and increasing electrolyte molarity to 1.5 mol L^{-1}. Reproduced with permission.[26b] Copyright 2017, Springer Nature.

1) Structure engineering of thick electrode: Porous structures are significant in thick electrodes to enable faster ion diffusion, higher electrolyte permeability, and buffer volume changes during charge/discharge. However, a larger porosity could lead to higher interfacial side reactions, which not only constraints Coulombic efficiency but also increases the volume of whole electrode in batteries and thus reduces cell-level energy densities. Besides, as pore size and distribution impact considerably on the charge transport behaviors, the rational designs of porous structures (e.g., creating hierarchical channels with low tortuosity) represent a promising direction to optimize the electrode performance. In this regard, combining experimental pore engineering with theoretical models and calculation might provide valuable insights.
2) Optimizing cell component engineering: Optimizing cell component engineering is a common strategy to achieve high proportion of active materials in the total packaged cell. In this case, the thickness of electrode is an important parameter as it affects the overall energy density output and manufacturing costs of cell stacks. Active materials determine the energy density level, while reduction of inactive materials by various methods such as thick cathode with high press density, thinner separators and current collectors, bipolar technology, etc. can help to increase that value upon a specific level. Currently, most of the studies are based on i) developing new active materials; ii) structural designs of electrodes to decrease the adverse effects of increasing electrode thicknesses. However, much fewer researches focus on optimizing cell component, which could be an essential challenge on the industry in the future.
3) Cell manufacturing engineering: Cell manufacturing is a complex process. It is of significance to obtain a thick electrode with complete structure and excellent performance during the fabrication process. Generally speaking, the electrode fabrication consists of four steps including "mixing-coating-drying-calendering."[191] Due to the solvent volatilization and external rolling, the structural failure of thick electrode (e.g., cracking and delamination) is likely to occur during irreversible fabricated steps of drying and calendaring, resulting in lower cell performance and there are no subsequent remedial measures. Much less efforts have been reported to solve those issues encountered in real practice production than has been made to develop new electrode structures. As well as the issue of failure in up-scaling of active materials should receive enough attention. Fundamental understanding of the process combined with advanced manufacturing engineering of thick electrodes is key to overcoming the challenges.
4) Application extension and interdisciplinary research: Nowadays, a variety of energy storage systems have been developed to fit different application scenarios. In this review, we mainly summarize the researches on LIB and SIB electrodes with high mass loadings and areal capacities. In practice, certain strategies such as high-tap-density active materials, compressible 3-D network structures and novel manufacturing techniques, can be applied on the design of other metal ion batteries like potassium or zinc ion batteries, and even those with different battery chemistries like lithium–sulfur batteries and solid-state batteries. For wearable or implantable microelectronics, flexible power modules with high areal capacities are required. From this point, it is important to make electrodes with both high mass loadings and mechanical flexibility, which can be realized in structures with robust and long-range entanglements. In addition, interdisciplinary research helps create innovative ideas. Combining them with the state-of-the-art data processing and calculation methods can accelerate the design and discovery of electrode materials and structures for high-areal-capacity energy storage.

Acknowledgements

Y.C. and B.Z. contributed equally to this work. A.C. acknowledges financial support from the National Key R&D Program of China (Grant No. 2017YFA0206701).

Conflict of Interest

The authors declare no conflict of interest.

Keywords

areal capacity, areal mass loading, electrode architecture, lithium-ion batteries, sodium-ion batteries

Received: May 28, 2022
Revised: August 25, 2022
Published online:

[1] a) N. Nitta, F. X. Wu, J. T. Lee, G. Yushin, *Mater. Today* **2015**, *18*, 252; b) J. M. Tarascon, M. Armand, *Nature* **2001**, *414*, 359.
[2] a) J. Y. Hwang, S. T. Myung, Y. K. Sun, *Chem. Soc. Rev.* **2017**, *46*, 3529; b) C. Vaalma, D. Buchholz, M. Weil, S. Passerini, *Nat. Rev. Mater.* **2018**, *3*, 18013.
[3] J. S. Meng, H. C. Guo, C. J. Niu, Y. L. Zhao, L. Xu, Q. Li, L. Q. Mai, *Joule* **2017**, *1*, 522.
[4] Y. Y. Liu, G. M. Zhou, K. Liu, Y. Cui, *Acc. Chem. Res.* **2017**, *50*, 2895.
[5] M. Li, J. Lu, Z. W. Chen, K. Amine, *Adv. Mater.* **2018**, *30*, 24.
[6] A. W. Golubkov, D. Fuchs, J. Wagner, H. Wiltsche, C. Stangl, G. Fauler, G. Voitic, A. Thaler, V. Hacker, *RSC Adv.* **2014**, *4*, 3633.
[7] Y. Gogotsi, P. Simon, *Science* **2011**, *334*, 917.
[8] J. B. Quinn, T. Waldmann, K. Richter, M. Kasper, M. Wohlfahrt-Mehrens, *J. Electrochem. Soc.* **2018**, *165*, A3284.
[9] G. Patry, A. Romagny, S. Martinet, D. Froelich, *Energy Sci. Eng.* **2015**, *3*, 71.
[10] Z. J. Du, K. M. Rollag, J. Li, S. J. An, M. Wood, Y. Sheng, P. P. Mukherjee, C. Daniel, D. L. Wood, *J. Power Sources* **2017**, *354*, 200.
[11] a) L. Zolin, M. Chandesris, W. Porcher, B. Lestriez, *Energy Technol.* **2019**, *7*, 1900025; b) S. Lim, K. H. Ahn, M. Yamamura, *Langmuir* **2013**, *29*, 8233.
[12] A. J. Blake, R. R. Kohlmeyer, L. F. Drummy, J. S. Gutierrez-Kolar, J. Carpena-Nunez, B. Maruyama, R. Shahbazian-Yassar, H. Huang, M. F. Durstockt, *ACS Appl. Mater. Interfaces* **2016**, *8*, 5196.
[13] a) G. S. Zhang, C. E. Shaffer, C. Y. Wang, C. D. Rahn, *J. Electrochem. Soc.* **2013**, *160*, A610; b) A. M. Bruck, L. Wang, A. B. Brady, D. M. Lutz, B. L. Hoff, K. R. Li, N. Stavinski, D. C. Bock, K. J. Takeuchi, E. S. Takeuchi, A. C. Marschilok, *J. Phys. Chem. C*

2019, *123*, 18834; c) S. Malifarge, B. Delobel, C. Delacourt, *J. Electrochem. Soc.* **2018**, *165*, A1275.
[14] N. Dufour, M. Chandesris, S. Genies, M. Cugnet, Y. Bultel, *Electrochim. Acta* **2018**, *272*, 97.
[15] K. C. Kil, U. Paik, *Macromol. Res.* **2015**, *23*, 719.
[16] a) K. G. Gallagher, S. E. Trask, C. Bauer, T. Woehrle, S. F. Lux, M. Tschech, P. Lamp, B. J. Polzin, S. Ha, B. Long, Q. L. Wu, W. Q. Lu, D. W. Dees, A. N. Jansen, *J. Electrochem. Soc.* **2016**, *163*, A138; b) M. Singh, J. Kaiser, H. Hahn, *J. Electrochem. Soc.* **2015**, *162*, A1196.
[17] C. Uhlmann, J. Illig, M. Ender, R. Schuster, E. Ivers-Tiffee, *J. Power Sources* **2015**, *279*, 428.
[18] a) C. Meyer, M. Kosfeld, W. Haselrieder, A. Kwade, *J. Energy Storage* **2018**, *18*, 371; b) H. Gao, Q. Wu, Y. X. Hu, J. P. Zheng, K. Amine, Z. H. Chen, *J. Phys. Chem. Lett.* **2018**, *9*, 5100.
[19] Z. Karkar, D. Mazouzi, C. R. Hernandez, D. Guyomard, L. Roue, B. Lestriez, *Electrochim. Acta* **2016**, *215*, 276.
[20] P. P. R. M. L. Harks, C. B. Robledo, C. George, C. Wang, T. van Dijk, L. Sturkenboom, E. D. W. Roesink, F. M. Mulder, *J. Power Sources* **2019**, *441*, 227200.
[21] W. F. Ren, J. T. Li, Z. G. Huang, L. Deng, Y. Zhou, L. Huang, S. G. Sun, *ChemElectroChem* **2018**, *5*, 3258.
[22] W. H. Chen, X. X. Zhang, L. W. Mi, C. T. Liu, J. M. Zhang, S. Z. Cui, X. M. Feng, Y. L. Cao, C. Y. Shen, *Adv. Mater.* **2019**, *31*, 9.
[23] Y. D. Kuang, C. J. Chen, D. Kirsch, L. B. Hu, *Adv. Energy Mater.* **2019**, *9*, 1901457.
[24] C. N. Liang, Y. X. Tao, N. Yang, D. K. Huang, S. Li, K. Han, Y. Z. Luo, H. Chen, L. Q. Mai, *Electrochim. Acta* **2019**, *311*, 192.
[25] M. M. Thackeray, K. Amine, *Nat. Energy* **2021**, *6*, 933.
[26] a) C. W. Park, J.-H. Lee, J. K. Seo, W. Y. Jo, D. Whang, S. M. Hwang, Y.-J. Kim, *Nat. Commun.* **2021**, *12*, 2145; b) Z. Du, D. L. Wood, C. Daniel, S. Kalnaus, J. Li, *J. Appl. Electrochem.* **2017**, *47*, 405.
[27] B. S. Chang, J. P. Liu, G. Y. Qing, T. L. Sun, *J. Mater. Chem. A* **2018**, *6*, 11916.
[28] L. Zhang, C. Wang, Y. Dou, N. Cheng, D. Cui, Y. Du, P. Liu, M. Al-Mamun, S. Zhang, H. Zhao, *Angew. Chem., Int. Ed.* **2019**, *58*, 8824.
[29] D. Lin, Z. Lu, P.-C. Hsu, H. R. Lee, N. Liu, J. Zhao, H. Wang, C. Liu, Y. Cui, *Energy Environ. Sci.* **2015**, *8*, 2371.
[30] Y. Sun, L. Wang, Y. Li, Y. Li, H. R. Lee, A. Pei, X. He, Y. Cui, *Joule* **2019**, *3*, 1080.
[31] J. Wu, Z. Ju, X. Zhang, A. C. Marschilok, K. J. Takeuchi, H. Wang, E. S. Takeuchi, G. Yu, *Adv. Mater.* **2022**, *34*, 2202780.
[32] B. Zhao, Q. Liu, Y. Chen, Q. Liu, Q. Yu, H. B. Wu, *Adv. Funct. Mater.* **2020**, *30*, 2002019.
[33] K. J. Griffith, K. M. Wiaderek, G. Cibin, L. E. Marbella, C. P. Grey, *Nature* **2018**, *559*, 556.
[34] a) Y. Ko, M. Kwon, W. K. Bae, B. Lee, S. W. Lee, J. Cho, *Nat. Commun.* **2017**, *8*, 536; b) D. Nam, M. Kwon, Y. Ko, J. Huh, S. W. Lee, J. Cho, *Appl. Phys. Rev.* **2021**, *8*, 011405.
[35] M. Kwon, D. Nam, S. Lee, Y. Kim, B. Yeom, J. H. Moon, S. W. Lee, Y. Ko, J. Cho, *Adv. Energy Mater.* **2021**, *11*, 2101631.
[36] B. Chang, J. Liu, G. Qing, T. Sun, *J. Mater. Chem. A* **2018**, *6*, 11916.
[37] N. Liu, Z. Lu, J. Zhao, M. T. Mcdowell, H. W. Lee, W. Zhao, Y. Cui, *Nat. Nanotechnol.* **2014**, *9*, 187.
[38] D. N. Liu, X. M. Xu, J. Tan, J. X. Zhu, Q. Li, Y. Z. Luo, P. J. Wu, X. Zhang, C. H. Han, L. Q. Mai, *Small* **2019**, *15*, 1803572.
[39] J. M. Xu, Y. F. Liu, L. He, C. J. Zhang, Y. H. Zhang, *Ceram. Int.* **2016**, *42*, 12027.
[40] D. Wang, H. Liu, M. Li, X. Wang, S. Bai, Y. Shi, J. Tian, Z. Shan, Y. S. Meng, P. Liu, Z. Chen, *Energy Storage Mater.* **2019**, *21*, 361.
[41] K. Mishra, X. C. Liu, F. S. Ke, X. D. Zhou, *Composites, Part B* **2019**, *163*, 158.
[42] a) D. Mazouzi, Z. Karkar, C. R. Hernandez, P. J. Manero, D. Guyomard, L. Roue, B. Lestriez, *J. Power Sources* **2015**, *280*, 533; b) J. Yoon, D. X. Oh, C. Jo, J. Lee, D. S. Hwang, *Phys. Chem. Chem. Phys.* **2014**, *16*, 25628; c) L. M. Wei, C. X. Chen, Z. Y. Hou, H. Wei, *Sci. Rep.* **2016**, *6*, 19583.
[43] a) R. Yi, J. T. Zai, F. Dai, M. L. Gordin, D. H. Wang, *Nano Energy* **2014**, *6*, 211; b) L. J. Yan, J. Liu, Q. Q. Wang, M. H. Sun, Z. G. Jiang, C. D. Liang, F. Pan, Z. Lin, *ACS Appl. Mater. Interfaces* **2017**, *9*, 38159; c) M. S. Han, E. Yu, *Energy Technol.* **2019**, *7*, 1900084; d) L. Ibing, T. Gallasch, P. Schneider, P. Niehoff, A. Hintennach, M. Winter, F. M. Schappacher, *J. Power Sources* **2019**, *423*, 183.
[44] J. Liu, Y. X. Xuan, D. G. D. Galpaya, Y. X. Gu, Z. Lin, S. Q. Zhang, C. Yan, S. H. Feng, L. Wang, *J. Mater. Chem. A* **2018**, *6*, 19455.
[45] C.-Y. Tsai, Y.-L. Liu, *Electrochim. Acta* **2021**, *379*, 138180.
[46] Z. Liu, C. Fang, X. He, Y. Zhao, H. Xu, J. Lei, G. Liu, *ACS Appl. Mater. Interfaces* **2021**, *13*, 46518.
[47] Z. Chen, C. Wang, J. Lopez, Z. D. Lu, Y. Cui, Z. A. Bao, *Adv. Energy Mater.* **2015**, *5*, 1401826.
[48] H. Chen, Z. Wu, Z. Su, S. Chen, C. Yan, M. Al-Mamun, Y. Tang, S. Zhang, *Nano Energy* **2021**, *81*, 105654.
[49] Z. Li, Y. Zhang, T. Liu, X. Gao, S. Li, M. Ling, C. Liang, J. Zheng, Z. Lin, *Adv. Energy Mater.* **2020**, *10*, 1903110.
[50] S. Huang, J. G. Ren, R. Liu, Y. Bai, X. L. Li, Y. Y. Huang, M. Yue, X. Q. He, G. H. Yuan, *New J. Chem.* **2018**, *42*, 6742.
[51] T. F. Liu, Q. L. Chu, C. Yan, S. Q. Zhang, Z. Lin, J. Lu, *Adv. Energy Mater.* **2019**, *9*, 1802645.
[52] Z. Li, Z. Wan, X. Zeng, S. Zhang, L. Yan, J. Ji, H. Wang, Q. Ma, T. Liu, Z. Lin, M. Ling, C. Liang, *Nano Energy* **2021**, *79*, 105430.
[53] T. M. Higgins, S.-H. Park, P. J. King, C. Zhang, N. McEvoy, N. C. Berner, D. Daly, A. Shmeliov, U. Khan, G. Duesberg, *ACS Nano* **2016**, *10*, 3702.
[54] H. Wang, J. Fu, C. Wang, R. Zhang, Y. Yang, Y. Li, C. Li, Q. Sun, H. Li, T. Zhai, *Adv. Funct. Mater.* **2021**, *31*, 2102284.
[55] Y. Su, X. Feng, R. Zheng, Y. Lv, Z. Wang, Y. Zhao, L. Shi, S. Yuan, *ACS Nano* **2021**, *15*, 14570.
[56] C.-H. Tsao, T.-K. Yang, K.-Y. Chen, C.-E. Fang, M. Ueda, F. H. Richter, J. Janek, C.-c. Chiu, P.-L. Kuo, *ACS Appl. Mater. Interfaces* **2021**, *13*, 9846.
[57] B. Tran, I. O. Oladeji, Z. D. Wang, J. Calderon, G. Y. Chai, D. Atherton, L. Zhai, *Electrochim. Acta* **2013**, *88*, 536.
[58] B. Tran, I. O. Oladeji, Z. D. Wang, J. Calderon, G. Y. Chai, D. Atherton, L. Zhai, *J. Electrochem. Soc.* **2012**, *159*, A1928.
[59] Z. Chen, C. Wang, J. Lopez, Z. Lu, Y. Cui, Z. Bao, *Adv. Energy Mater.* **2015**, *5*, 1401826.
[60] J. Kang, D.-Y. Han, S. Kim, J. Ryu, S. Park, *Adv. Mater.* 2203194.
[61] a) Y. Kuang, C. Chen, D. Kirsch, L. Hu, *Adv. Energy Mater.* **2019**, *9*, 1901457; b) Z. Ju, X. Zhang, J. Wu, S. T. King, C.-C. Chang, S. Yan, Y. Xue, K. J. Takeuchi, A. C. Marschilok, L. Wang, E. S. Takeuchi, G. Yu, *Nano Lett.* **2022**, *16*, 6700.
[62] Q. Cheng, Z. M. Song, T. Ma, B. B. Smith, R. Tang, H. Y. Yu, H. Q. Jiang, C. K. Chan, *Nano Lett.* **2013**, *13*, 4969.
[63] a) Z. W. Zhang, M. Zhang, P. X. Lu, Q. L. Chen, H. Wang, Q. S. Liu, *J. Alloys Compd.* **2019**, *809*, 151823; b) B. Wang, J. Ryu, S. Choi, G. Song, D. Hong, C. Hwang, X. Chen, B. Wang, W. Li, H. K. Song, S. Park, R. S. Ruoff, *ACS Nano* **2018**, *12*, 1739.
[64] a) J. X. Zheng, Q. Zhao, X. T. Liu, T. Tang, D. C. Bock, A. M. Bruck, K. R. Tallman, L. M. Housel, A. M. Kiss, A. C. Marschilok, E. S. Takeuchi, K. J. Takeuchi, L. A. Archer, *ACS Energy Lett.* **2019**, *4*, 271; b) W. C. Chang, S. P. Lu, H. C. Chu, H. Y. Tuan, *ACS Sustainable Chem. Eng.* **2019**, *7*, 156.
[65] S. H. Lee, C. Huang, P. S. Grant, *Energy Storage Mater.* **2021**, *38*, 70.
[66] a) I. V. Thorat, D. E. Stephenson, N. A. Zacharias, K. Zaghib, J. N. Harb, D. R. Wheeler, *J. Power Sources* **2009**, *188*, 592; b) M. Ebner, V. Wood, *J. Electrochem. Soc.* **2015**, *162*, A3064.
[67] J. Billaud, F. Bouville, T. Magrini, C. Villevieille, A. R. Studart, *Nat. Energy* **2016**, *1*, 16097.

[68] C. J. Chen, Y. Zhang, Y. J. Li, Y. D. Kuang, J. W. Song, W. Luo, Y. B. Wang, Y. G. Yao, G. Pastel, J. Xie, L. B. Hu, *Adv. Energy Mater.* **2017**, *7*, 1700595.
[69] L. L. Lu, Y. Y. Lu, Z. J. Xiao, T. W. Zhang, F. Zhou, T. Ma, Y. Ni, H. B. Yao, S. H. Yu, Y. Cui, *Adv. Mater.* **2018**, *30*, 1706745.
[70] P. Zhang, Y. Q. Liu, Y. Yan, Y. Yu, Q. H. Wang, M. K. Liu, *ACS Appl. Energy Mater.* **2018**, *1*, 4814.
[71] K. Yang, L. Yang, Z. Wang, B. Guo, Z. Song, Y. Fu, Y. Ji, M. Liu, W. Zhao, X. Liu, S. Yang, F. Pan, *Adv. Energy Mater.* **2021**, *11*, 2100601.
[72] Z. D. Zhao, M. Q. Sun, W. J. Chen, Y. Liu, L. Zhang, N. C. Dongfang, Y. B. Ruan, J. J. Zhang, P. Wang, L. Dong, Y. Y. Xia, H. B. Lu, *Adv. Funct. Mater.* **2019**, *29*, 1809196.
[73] Y. Du, N. Hedayat, D. Panthi, H. Ilkhani, B. J. Emley, T. Woodson, *Materialia* **2018**, *1*, 198.
[74] H. L. Zhu, W. Luo, P. N. Ciesielski, Z. Q. Fang, J. Y. Zhu, G. Henriksson, M. E. Himmel, L. B. Hu, *Chem. Rev.* **2016**, *116*, 9305.
[75] S. Deville, *Scr. Mater.* **2018**, *147*, 119.
[76] S. H. Park, P. J. King, R. Y. Tian, C. S. Boland, J. Coelho, C. F. Zhang, P. McBean, N. McEvoy, M. P. Kremer, D. Daly, J. N. Coleman, V. Nicolosi, *Nat. Energy* **2019**, *4*, 560.
[77] Z. C. Xiao, Y. Li, C. L. Liang, Y. Liu, R. Y. Bao, M. B. Yang, W. Yang, *J. Electroanal. Chem.* **2019**, *840*, 430.
[78] Y. D. Kuang, C. J. Chen, G. Pastel, Y. J. Li, J. W. Song, R. Y. Mi, W. Q. Kong, B. Y. Liu, Y. Q. Jiang, K. Yang, L. B. Hu, *Adv. Energy Mater.* **2018**, *8*, 1802398.
[79] X. Han, Z. Q. Zhang, G. R. Zheng, R. You, J. Y. Wang, C. Li, S. Y. Chen, Y. Yang, *ACS Appl. Mater. Interfaces* **2019**, *11*, 714.
[80] X. Zhu, Z. M. Li, X. L. Jia, W. J. Dong, G. Wang, F. Wei, Y. F. Lu, *ACS Sustainable Chem. Eng.* **2018**, *6*, 15608.
[81] Y. H. Dai, Q. D. Li, S. S. Tan, Q. L. Wei, Y. X. Pan, X. C. Tian, K. N. Zhao, X. Xu, Q. Y. An, L. Q. Mai, Q. J. Zhang, *Nano Energy* **2017**, *40*, 73.
[82] M. Xie, B. Li, Y. Zhou, *J. Mater. Chem. A* **2015**, *3*, 23180.
[83] H. Huang, X. K. Ju, P. Deng, S. Y. Li, B. H. Qu, T. H. Wang, *ChemElectroChem* **2018**, *5*, 2330.
[84] Y. F. Chao, K. Z. Wang, R. Jalili, A. Morlando, C. Y. Qin, A. Vijayakumar, C. Y. Wang, G. G. Wallace, *ACS Appl. Mater. Interfaces* **2019**, *11*, 46746.
[85] Z. W. Liu, R. X. Xu, W. Wei, P. Jing, X. Li, Q. Y. Zhu, H. J. Sun, Y. Y. Dong, G. S. Zakharova, *Solid State Ionics* **2019**, *329*, 74.
[86] J. Q. Luo, F. L. Li, Y. M. Zhou, S. J. Liu, J. G. Ma, J. L. Liu, *J. Alloys Compd.* **2018**, *749*, 697.
[87] Y. T. Zhao, G. S. Huang, Y. L. Li, R. Edy, P. B. Gao, H. Tang, Z. H. Bao, Y. F. Mei, *J. Mater. Chem. A* **2018**, *6*, 7227.
[88] K. Y. Song, G. S. Jang, J. Tao, J. H. Lee, S. K. Joo, *J. Nanosci. Nanotechnol.* **2018**, *18*, 992.
[89] G. F. Yang, K. Y. Song, S. K. Joo, *RSC Adv.* **2015**, *5*, 16702.
[90] D. J. Noelle, M. Wang, Y. Qiao, *J. Power Sources* **2018**, *399*, 125.
[91] L. B. Hu, F. L.a Mantia, H. Wu, X. Xie, J. McDonough, M. Pasta, Y. Cui, *Adv. Energy Mater.* **2011**, *1*, 1012.
[92] S. H. Ha, K. H. Shin, H. W. Park, Y. J. Lee, *Small* **2018**, *14*, 1703418.
[93] W. X. Li, Y. J. Chen, A. Zangiabadi, Z. Y. Li, X. H. Xiao, W. L. Huang, Q. Cheng, S. F. Lou, H. R. Zhang, A. Y. Cao, X. Roy, Y. Yang, *ACS Appl. Mater. Interfaces* **2020**, *12*, 33803.
[94] Z. P. Wang, Y. S. Wang, Y. J. Chen, M. Yousaf, H. S. Wu, A. Y. Cao, R. P. S. Han, *Adv. Funct. Mater.* **2019**, *29*, 1807467.
[95] K. Moyer, R. Carter, T. Hanken, A. Douglas, L. Oakes, C. L. Pint, *Mater. Sci. Eng., B* **2019**, *241*, 42.
[96] E. C. Self, M. Naguib, R. E. Ruther, E. C. McRen, R. Wycisk, G. Liu, J. Nanda, P. N. Pintauro, *ChemSusChem* **2017**, *10*, 1823.
[97] E. C. Self, R. Wycisk, P. N. Pintauro, *J. Power Sources* **2015**, *282*, 187.
[98] H. Abe, M. Kubota, M. Nemoto, Y. Masuda, Y. Tanaka, H. Munakata, K. Kanamura, *J. Power Sources* **2016**, *334*, 78.
[99] S. Zhou, P. Huang, T. Xiong, F. Yang, H. Yang, Y. Huang, D. Li, J. Deng, M.-S. Balogun, *Small* **2021**, *17*, 2100778.
[100] Y. Ham, N. J. Fritz, G. Hyun, Y. B. Lee, J. S. Nam, I.-D. Kim, P. V. Braun, S. Jeon, *Energy Environ. Sci.* **2021**, *14*, 5894.
[101] S. F. Zhang, Z. J. Zhang, H. W. Li, Z. Y. Yu, Q. Huang, Z. J. Qiao, L. S. Zong, L. Yan, J. X. Li, J. L. Kang, *Chem. Eng. J.* **2020**, *383*, 123097.
[102] F. Zhang, C. K. Yang, H. Q. Guan, Y. R. Hu, C. Jin, H. H. Zhou, L. M. Qi, *ACS Appl. Energy Mater.* **2018**, *1*, 5417.
[103] Y. F. Li, Y. H. Shi, S. G. Wang, J. H. Liu, J. Lin, Y. Xia, X. L. Wu, C. Y. Fan, J. P. Zhang, H. M. Xie, H. Z. Sun, Z. M. Su, *Adv. Energy Mater.* **2019**, *9*, 1902068.
[104] X. H. Wang, Y. Fan, R. A. Susantyoko, Q. Z. Xiao, L. M. Sun, D. Y. He, Q. Zhang, *Nano Energy* **2014**, *5*, 91.
[105] Y. Chen, Y. Wang, Z. Wang, M. Zou, H. Zhang, W. Zhao, M. Yousaf, L. Yang, A. Cao, R. P. S. Han, *Adv. Energy Mater.* **2018**, *8*, 10.
[106] L. B. Hu, H. Wu, Y. F. Gao, A. Y. Cao, H. B. Li, J. McDough, X. Xie, M. Zhou, Y. Cui, *Adv. Energy Mater.* **2011**, *1*, 523.
[107] X. Y. Chen, H. L. Zhu, Y. C. Chen, Y. Y. Shang, A. Y. Cao, L. B. Hu, G. W. Rubloff, *ACS Nano* **2012**, *6*, 7948.
[108] X. L. Yu, J. J. Deng, X. Yang, J. Li, Z. H. Huang, B. H. Li, F. Y. Kang, *Nano Energy* **2020**, *67*, 104256.
[109] Y. C. Huang, H. Yang, T. Z. Xiong, D. Adekoya, W. T. Qiu, Z. M. Wang, S. Q. Zhang, M. S. Balogun, *Energy Storage Mater.* **2020**, *25*, 41.
[110] C. S. Zhou, J. M. Lu, M. X. Hu, Z. H. Huang, F. Y. Kang, R. T. Lv, *Small* **2018**, *14*, 1801832.
[111] X. Y. Shan, S. Zhang, N. Zhang, Y. J. Chen, H. Gao, X. T. Zhang, *J. Colloid Interface Sci.* **2018**, *510*, 327.
[112] S. T. Li, G. Liu, J. Liu, Y. K. Lu, Q. Yang, L. Y. Yang, H. R. Yang, S. L. Liu, M. Lei, M. Han, *J. Mater. Chem. A* **2016**, *4*, 6426.
[113] K. Ma, X. Liu, Q. L. Cheng, P. Saha, H. Jiang, C. Z. Li, *J. Power Sources* **2017**, *357*, 71.
[114] S. Y. Kim, C. H. Kim, C.-M. Yang, *J. Power Sources* **2021**, *486*, 229350.
[115] H. X. Zhang, Y. Liu, H. Jiang, Z. N. Deng, H. L. Liu, C. Z. Li, *Chem. Eng. Sci.* **2019**, *207*, 611.
[116] L. H. Zhang, T. Wei, Z. M. Jiang, Z. J. Fan, *Chem.-Eur. J.* **2019**, *25*, 5022.
[117] J. F. Liang, Y. Q. Xu, H. T. Sun, X. Xu, T. X. Liu, H. T. Liu, H. Wang, *Energy Technol.* **2020**, *8*, 1901002.
[118] J. F. Liang, H. T. Sun, Z. P. Zhao, Y. L. Wang, Z. Y. Feng, J. Zhu, L. Guo, Y. Huang, X. F. Duan, *iScience* **2019**, *19*, 728.
[119] J. F. Liang, H. T. Sun, Y. Q. Xu, T. X. Liu, H. Wang, H. Liu, L. Guo, *Inorg. Chem. Front.* **2019**, *6*, 1367.
[120] Z. H. Chen, J. D. Chen, F. X. Bu, P. O. Agboola, I. Shakir, Y. X. Xu, *ACS Nano* **2018**, *12*, 12879.
[121] H. Sun, L. Mei, J. Liang, Z. Zhao, C. Lee, H. Fei, M. Ding, J. Lau, M. Li, C. Wang, X. Xu, G. Hao, B. Papandrea, I. Shakir, B. Dunn, Y. Huang, X. Duan, *Science* **2017**, *356*, 599.
[122] S. Zhang, C. Liu, H. Wang, H. Wang, J. Sun, Y. Zhang, X. Han, Y. Cao, S. Liu, J. Sun, *ACS Nano* **2021**, *15*, 3365.
[123] R. W. Mo, Z. Y. Lei, D. Rooney, K. N. Sun, *ACS Nano* **2019**, *13*, 7536.
[124] T. S. Dorr, S. Fleischmann, M. Zeiger, I. Grobelsek, P. W. de Oliveira, V. Presser, *Chem. - Eur. J.* **2018**, *24*, 6358.
[125] M. Singh, J. Kaiser, H. Hahn, *Batteries* **2016**, *2*, 35.
[126] L. Ke, W. Lv, F. Y. Su, Y. B. He, C. H. You, B. H. Li, Z. J. Li, Q. H. Yang, F. Y. Kang, *Carbon* **2015**, *92*, 311.
[127] Z. J. Du, C. J. Janke, J. L. Li, D. L. Wood, *Green Energy Environ.* **2019**, *4*, 375.
[128] M. E. Sotomayor, C. de la Torre-Gamarra, B. Levenfeld, J. Y. Sanchez, A. Varez, G. T. Kim, A. Varzi, S. Passerini, *J. Power Sources* **2019**, *437*, 226923.

[129] M. E. Sotomayor, C. de la Torre-Gamarra, W. Bucheli, J. M. Amarilla, A. Varez, B. Levenfeld, J. Y. Sanchez, *J. Mater. Chem. A* **2018**, *6*, 5952.
[130] S. J. Kim, M. Naguib, M. Q. Zhao, C. F. Zhang, H. T. Jung, M. W. Barsoum, Y. Gogotsi, *Electrochim. Acta* **2015**, *163*, 246.
[131] R. Elango, A. Demortiere, V. De Andrade, M. Morcrette, V. Seznec, *Adv. Energy Mater.* **2018**, *8*, 1703031.
[132] J. W. Wang, Q. Sun, X. J. Gao, C. H. Wang, W. H. Li, F. B. Holness, M. Zheng, R. Y. Li, A. D. Price, X. H. Sun, T. K. Sham, X. L. Sun, *ACS Appl. Mater. Interfaces* **2018**, *10*, 39794.
[133] T. S. Wei, B. Y. Ahn, J. Grotto, J. A. Lewis, *Adv. Mater.* **2018**, *30*, 1703027.
[134] L. Zhou, W. W. Ning, C. Wu, D. Zhang, W. F. Wei, J. M. Ma, C. C. Li, L. B. Chen, *Adv. Mater. Technol.* **2019**, *4*, 1800402.
[135] J. Li, Y. Gao, X. H. Liang, J. Park, *Batteries Supercaps* **2019**, *2*, 139.
[136] C. Sun, S. R. Liu, X. L. Shi, C. Lai, J. J. Liang, Y. S. Chen, *Chem. Eng. J.* **2020**, *381*, 122641.
[137] P. H. Zhu, H. J. Seifert, W. Pfleging, *Appl. Sci.* **2019**, *9*, 4067.
[138] J. H. Rakebrandt, P. Smyrek, Y. Zheng, H. J. Seifert, W. Pfleging, *Proc. SPIE* **2017**, *10092*, 100920M.
[139] J. Park, S. Hyeon, S. Jeong, H. J. Kim, *J. Ind. Eng. Chem.* **2019**, *70*, 178.
[140] F. Zhang, M. Wei, V. V. Viswanathan, B. Swart, Y. Y. Shao, G. Wu, C. Zhou, *Nano Energy* **2017**, *40*, 418.
[141] a) M. S. Saleh, J. Li, J. Park, R. Panat, *Addit. Manuf.* **2018**, *23*, 70; b) P. Chang, H. Mei, S. Zhou, K. G. Dassios, L. Cheng, *J. Mater. Chem. A* **2019**, *7*, 4230.
[142] W. Pfleging, *Nanophotonics* **2018**, *7*, 549.
[143] a) Z. Lv, M. Yue, M. Ling, H. Zhang, J. Yan, Q. Zheng, X. Li, *Adv. Energy Mater.* **2021**, *11*, 2003725; b) J. Wang, M. Wang, N. Ren, J. Dong, Y. Li, C. Chen, *Energy Storage Mater.* **2021**, *39*, 287; c) J. Wu, Z. Ju, X. Zhang, C. Quilty, K. J. Takeuchi, D. C. Bock, A. C. Marschilok, E. S. Takeuchi, G. Yu, *ACS Nano* **2021**, *15*, 19109; d) X. Zhang, Z. Ju, L. M. Housel, L. Wang, Y. Zhu, G. Singh, N. Sadique, K. J. Takeuchi, E. S. Takeuchi, A. C. Marschilok, G. Yu, *Nano Lett.* **2019**, *19*, 8255.
[144] S. Tu, Z. Lu, M. Zheng, Z. Chen, X. Wang, Z. Cai, C. Chen, L. Wang, C. Li, Z. W. Seh, S. Zhang, J. Lu, Y. Sun, *Adv. Mater.* **2022**, 2202892.
[145] C. Chen, Y. Zhang, Y. Li, Y. Kuang, J. Song, W. Luo, Y. Wang, Y. Yao, G. Pastel, J. Xie, L. Hu, *Adv. Energy Mater.* **2017**, *7*, 1700595.
[146] X. Fan, C. Wang, *Chem. Soc. Rev.* **2021**, *50*, 10486.
[147] H. Jia, L. Zou, P. Gao, X. Cao, W. Zhao, Y. He, M. H. Engelhard, S. D. Burton, H. Wang, X. Ren, Q. Li, R. Yi, X. Zhang, C. Wang, Z. Xu, X. Li, J.-G. Zhang, W. Xu, *Adv. Energy Mater.* **2019**, *9*, 1900784.
[148] J. Chen, X. Fan, Q. Li, H. Yang, M. R. Khoshi, Y. Xu, S. Hwang, L. Chen, X. Ji, C. Yang, H. He, C. Wang, E. Garfunkel, D. Su, O. Borodin, C. Wang, *Nat. Energy* **2020**, *5*, 386.
[149] Y. Xiao, K. Turcheniuk, A. Narla, A.-Y. Song, X. Ren, A. Magasinski, A. Jain, S. Huang, H. Lee, G. Yushin, *Nat. Mater.* **2021**, *20*, 984.
[150] C. Y. Fan, X. H. Zhang, Y. H. Shi, H. Y. Xu, J. P. Zhang, X. L. Wu, *Nanoscale* **2018**, *10*, 18942.
[151] L. Gao, S. Chen, L. L. Zhang, X. L. Yang, *ChemElectroChem* **2019**, *6*, 947.
[152] Y. Chen, M. Yousaf, Y. Wang, Z. Wang, S. Lou, R. P. S. Han, Y. Yang, A. Cao, *Nano Energy* **2020**, *78*, 105265.
[153] M. Yousaf, Y. S. Wang, Y. J. Chen, Z. P. Wang, A. Firdous, Z. Ali, N. Mahmood, R. Q. Zou, S. J. Guo, R. P. S. Han, *Adv. Energy Mater.* **2019**, *9*, 1900567.
[154] M. Yousaf, Y. J. Chen, H. Tabassum, Z. P. Wang, Y. S. Wang, A. Y. Abid, A. Mahmood, N. Mahmood, S. J. Guo, R. P. S. Han, P. Gao, *Adv. Sci.* **2019**, *11*, 02907.
[155] B. Luo, Y. X. Hu, X. B. Zhu, T. F. Qiu, L. J. Zhi, M. Xiao, H. J. Zhang, M. C. Zou, A. Y. Cao, L. Z. Wang, *J. Mater. Chem. A* **2018**, *6*, 1462.
[156] C. H. Jiang, Z. X. Ye, H. T. Ye, Z. M. Zou, *Appl. Surf. Sci.* **2020**, *504*, 144464.
[157] C. S. Zhou, S. X. Fan, M. X. Hu, J. M. Lu, J. Li, Z. H. Huang, F. Y. Kang, R. T. Lv, *J. Mater. Chem. A* **2017**, *5*, 15517.
[158] D. L. Chao, P. Liang, Z. Chen, L. Y. Bai, H. Shen, X. X. Liu, X. H. Xia, Y. L. Zhao, S. V. Savilov, J. Y. Lin, Z. X. Shen, *ACS Nano* **2016**, *10*, 10211.
[159] L. Pan, H. J. Huang, M. Zhong, M. Niederberger, *Energy Storage Mater.* **2019**, *16*, 519.
[160] Z. Yuan, L. Wang, D. Li, J. Cao, W. Han, *ACS Nano* **2021**, *15*, 7439.
[161] Y. P. Liu, X. Y. He, D. Hanlon, A. Harvey, J. N. Coleman, Y. G. Li, *ACS Nano* **2016**, *10*, 8821.
[162] H. L. Ye, L. Wang, S. Deng, X. Q. Zeng, K. Q. Nie, P. N. Duchesne, B. Wang, S. Liu, J. H. Zhou, F. P. Zhao, N. Han, P. Zhang, J. Zhong, X. H. Sun, Y. Y. Li, Y. G. Li, J. Lu, *Adv. Energy Mater.* **2017**, *7*, 1601602.
[163] S. C. Yu, Z. G. Liu, H. Tempel, H. Kungl, R. A. Eichel, *J. Mater. Chem. A* **2018**, *6*, 18304.
[164] D. L. Guo, J. W. Qin, Z. G. Yin, J. M. Bai, Y. K. Sun, M. H. Cao, *Nano Energy* **2018**, *45*, 136.
[165] J. Hwang, K. Matsumoto, R. Hagiwara, *ACS Appl. Energy Mater.* **2019**, *2*, 2818.
[166] J. Zhou, J. C. Chen, M. X. Chen, J. Wang, X. Z. Liu, B. Wei, Z. C. Wang, J. J. Li, L. Gu, Q. H. Zhang, H. Wang, L. Guo, *Adv. Mater.* **2019**, *31*, 9.
[167] Y. Liu, Y. J. Fang, Z. W. Zhao, C. Z. Yuan, X. W. Lou, *Adv. Energy Mater.* **2019**, *9*, 9.
[168] D. Luo, C. Ma, J. Hou, Z. Zhang, R. Feng, L. Yang, X. Zhang, H. Lu, J. Liu, Y. Li, Y. Zhang, X. Wang, Z. Chen, *Adv. Energy Mater.* **2022**, *12*, 2103716.
[169] H. Fu, Z. W. Xu, R. Z. Li, W. W. Guan, K. Yao, J. F. Huang, J. Yang, X. T. Shen, *ACS Sustainable Chem. Eng.* **2018**, *6*, 14751.
[170] F. Shen, W. Luo, J. Q. Dai, Y. G. Yao, M. W. Zhu, E. Hitz, Y. F. Tang, Y. F. Chen, V. L. Sprenkle, X. L. Li, L. B. Hu, *Adv. Energy Mater.* **2016**, *6*, 7.
[171] Y. H. Zheng, Y. X. Lu, X. G. Qi, Y. S. Wang, L. Q. Mu, Y. M. Li, Q. Ma, J. Li, Y. S. Hu, *Energy Storage Mater.* **2019**, *18*, 269.
[172] Y. Wang, Z. Wen, C. C. Wang, C. C. Yang, Q. Jiang, *Small* **2021**, *17*, 2102349.
[173] J. Park, M. Lee, D. W. Feng, Z. H. Huang, A. C. Hinckley, A. Yakoyenko, X. D. Zou, Y. Cui, Z. A. Bao, *J. Am. Chem. Soc.* **2018**, *140*, 10315.
[174] X. M. Xu, P. J. Wu, Q. Li, W. Yang, X. Zhang, X. P. Wang, J. S. Meng, C. J. Niu, L. Q. Mai, *Nano Energy* **2018**, *50*, 606.
[175] a) S. Zheng, D. Feng, L. Xu, J. Du, B. Li, B. Wang, *ACS Mater. Lett.* **2022**, *4*, 432; b) X. Liu, B. Xiao, A. Daali, X. Zhou, Z. Yu, X. Li, Y. Liu, L. Yin, Z. Yang, C. Zhao, L. Zhu, Y. Ren, L. Cheng, S. Ahmed, Z. Chen, X. Li, G.-L. Xu, K. Amine, *ACS Energy Lett.* **2021**, *6*, 547; c) R. Tian, A. Griffin, M. McCrystall, M. Breshears, A. Harvey, C. Gabbett, D. V. Horváth, C. Backes, Y. Jing, T. Heine, S.-H. Park, J. Coelho, V. Nicolosi, M. Nentwig, C. Benndorf, O. Oeckler, J. N. Coleman, *Adv. Energy Mater.* **2021**, *11*, 2002364.
[176] Y. Liu, X. He, D. Hanlon, A. Harvey, J. N. Coleman, Y. Li, *ACS Nano* **2016**, *10*, 8821.
[177] J. Zhou, J. Chen, M. Chen, J. Wang, X. Liu, B. Wei, Z. Wang, J. Li, L. Gu, Q. Zhang, H. Wang, L. Guo, *Adv. Mater.* **2019**, *31*, 1807874.
[178] X. Xiang, K. Zhang, J. Chen, *Adv. Mater.* **2015**, *27*, 5343.
[179] J.-Y. Hwang, S.-M. Oh, S.-T. Myung, K. Y. Chung, I. Belharouak, Y.-K. Sun, *Nat. Commun.* **2015**, *6*, 6865.
[180] Y. Zhou, X. Rui, W. Sun, Z. Xu, Y. Zhou, W. J. Ng, Q. Yan, E. Fong, *ACS Nano* **2015**, *9*, 4628.
[181] Q. Wang, B. Zhao, S. Zhang, X. Gao, C. Deng, *J. Mater. Chem. A* **2015**, *3*, 7732.
[182] C. Guo, K. Zhang, Q. Zhao, L. Pei, J. Chen, *Chem. Commun.* **2015**, *51*, 10244.

[183] a) F. Duffner, N. Kronemeyer, J. Tübke, J. Leker, M. Winter, R. Schmuch, *Nat. Energy* **2021**, *6*, 123; b) X.-G. Yang, T. Liu, C.-Y. Wang, *Nat. Energy* **2021**, *6*, 176; c) N. D. Popovich, D. Rajagopal, E. Tasar, A. Phadke, *Nat. Energy* **2021**, *6*, 1017.
[184] J. Wu, X. Zhang, Z. Ju, L. Wang, Z. Hui, K. Mayilvahanan, K. J. Takeuchi, A. C. Marschilok, A. C. West, E. S. Takeuchi, G. Yu, *Adv. Mater.* **2021**, *33*, 2101275.
[185] J. Neumann, M. Petranikova, M. Meeus, J. D. Gamarra, R. Younesi, M. Winter, S. Nowak, *Adv. Energy Mater.* **2022**, *12*, 2102917.
[186] L. Liu, J. Xu, S. Wang, F. Wu, H. Li, L. Chen, *eTransportation* **2019**, *1*, 100010.
[187] X. Yang, K. Doyle-Davis, X. Gao, X. Sun, *eTransportation* **2022**, *11*, 100152.
[188] a) A. Kwade, W. Haselrieder, R. Leithoff, A. Modlinger, F. Dietrich, K. Droeder, *Nat. Energy* **2018**, *3*, 290; b) R. Schmuch, R. Wagner, G. Hörpel, T. Placke, M. Winter, *Nat. Energy* **2018**, *3*, 267.
[189] a) A. W. Xiao, H. J. Lee, I. Capone, A. Robertson, T.-U. Wi, J. Fawdon, S. Wheeler, H.-W. Lee, N. Grobert, M. Pasta, *Nat. Mater.* **2020**, *19*, 644; b) Q. Huang, K. Turcheniuk, X. Ren, A. Magasinski, A.-Y. Song, Y. Xiao, D. Kim, G. Yushin, *Nat. Mater.* **2019**, *18*, 1343.
[190] a) Y. Qi, Y. Lu, F. Ding, Q. Zhang, H. Li, X. Huang, L. Chen, Y.-S. Hu, *Angew. Chem., Int. Ed.* **2019**, *58*, 4361; b) T. Rojo, Y.-S. Hu, M. Forsyth, X. Li, *Adv. Energy Mater.* **2018**, *8*, 1800880; c) Y.-S. Hu, Y. Li, *ACS Energy Lett.* **2021**, *6*, 4115.
[191] A. M. Boyce, D. J. Cumming, C. Huang, S. P. Zankowski, P. S. Grant, D. J. L. Brett, P. R. Shearing, *ACS Nano* **2021**, *15*, 18624.

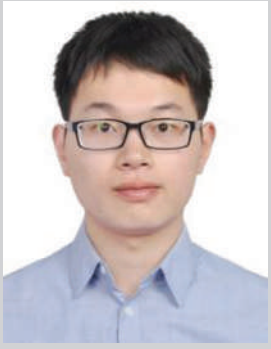

Yijun Chen is currently a senior material engineer in OPPO Research Institute. He received his Ph.D. degree in College of Engineering, Peking University, China in 2020. He worked as a visiting scholar in Columbia University from 2018 to 2020. He received his Bachelor degree in Huazhong University of Science and Technology in 2015. His research interests include advanced materials for energy storage and management systems, such as lithium/sodium ion batteries and radiative cooling.

Bo Zhao is currently a Ph.D. candidate under the supervision of Prof. Anyuan Cao in School of Materials Science and Engineering, Peking University. He received his Master and Bachelor degrees from Zhejiang University and Yanshan University in 2020 and 2017, respectively. His research interests mainly include advanced nanomaterials for energy storage, such as metal-air batteries based on the carbon nanotube sponges.

Yuan Yang received a B.S. in physics from Peking University in 2007 and a Ph.D. in materials science and engineering from Stanford University in 2012. After working as a postdoctoral associate at MIT for three years, he joined Columbia University in 2015 and is currently an associate professor in the Department of Applied Physics and Applied Mathematics. His research interests mainly include designing, characterizing, and analyzing materials and devices for electrochemical energy storage and conversion (e.g., batteries, water splitting), and thermal management (e.g., solar absorber, radiative cooling).

Anyuan Cao is currently a professor in the School of Materials Science and Engineering, Peking University. His research interests include controlled synthesis of carbon nanomaterials such as carbon nanotube fibers and sponges, self-assembly of nanostructures and optoelectronic properties, multifunctional nanocomposites for sensors, actuators, and thermal management. He developed the world's smallest nanotube brushes and 3D porous carbon nanotube sponges for environmental cleanup and energy storage electrodes. He has published about 200 papers in journals such as Science, Nature Nanotechnology, and Advanced Materials.